UNIVERSITY OF ROCHESTER
LABORATORY FOR LASER ENERGETICS

Volume 88
July–September 2001
DOE/SF/19460-404

LLE Review

Quarterly Report

About the Cover:

The cover photo shows one of the two large-area conditioning (LAC) stations operated by LLE's Optical Manufacturing Group in support of the National Ignition Facility project. Laboratory Engineer Jason Taniguchi monitors the control and data acquisition system, while Senior Technical Associate Nelson LeBarron checks the optic substrate mounted on the translation stage. During operation, intense laser pulses are delivered to the optic via the transparent beam tube at the right. The article entitled "Functional Damage Thresholds of Hafnia/Silica Coating Designs for the NIF Laser" (p. 177) describes how the LAC was used to test candidate high-reflectivity coatings on full-sized substrates like the one shown. The device visible on the left of the cover photo is a large-optic lifting tool (LOLT). Several facilities in the large-optics manufacturing community use this basic LLE design.

The translation stage of the second LAC is shown in the foreground of the photo to the left. Visible behind the test optic (at the right in photo) is the system that detects and documents damage caused by scanning the optic with an intense pulsed beam. Visual examination by trained eyes remains an important part of the process.

The work described in this volume includes current research at the Laboratory for Laser Energetics, which is supported by New York State Energy Research and Development Authority, the University of Rochester, the U.S. Department of Energy Office of Inertial Confinement Fusion under Cooperative Agreement No. DE-FC03-92SF19460, and other agencies.

Printed in the United States of America
Available from
National Technical Information Services
U.S. Department of Commerce
5285 Port Royal Road
Springfield, VA 22161

Price codes: Printed Copy A04
Microfiche A01

For questions or comments, contact Thomas H. Hinterman, *Editor*, Laboratory for Laser Energetics, 250 East River Road, Rochester, NY 14623-1299, (716) 275-0866.

Worldwide-Web Home Page: http://www.lle.rochester.edu/

UNIVERSITY OF ROCHESTER
LABORATORY FOR LASER ENERGETICS

Volume 88
July–September 2001
DOE/SF/19460-404

LLE Review

Quarterly Report

UR LLE

Contents

In Brief

This volume of the LLE Review, covering July–September 2001, features an article by C. Stoeckl, V. Yu. Glebov, J. D. Zuegel, and D. D. Meyerhofer (p. 171) that describes a simple, low-cost, wide-dynamic-range, neutron bang time (NBT) detector. This instrument complements the capabilities of the streak camera–based neutron temporal diagnostic (NTD), which is also installed on the OMEGA laser. The new NBT measures the neutron bang time of D_2- and DT-filled inertial confinement fusion (ICF) implosion capsules at neutron yields between 10^7 and 10^{11} with an absolute timing accuracy of better than 100 ps. This level of accuracy allows the modeling of the implosions to be effectively guided using hydrocode calculations.

Additional highlights of research presented in this issue include the following:

- J. Taniguchi, N. E. LeBarron, J. Howe, D. J. Smith, C. Stolz, C. Weizapfel, and J. Kimmons (p. 177) report that the current substrate cleaning and handling methods used in the application of high-reflectance optical coatings are so effective that it is necessary to test large parts in order to achieve statistically meaningful assessments. This has led LLE's Optical Manufacturing Group to use coating-conditioning equipment designed by Lawrence Livermore National Laboratory (LLNL) for large National Ignition Facility (NIF) optics to test new coating designs. The equipment facilitates testing of full-sized NIF substrates by automatically scanning the optic relative to a system that subjects a small area to representative laser pulses and simultaneously detects any resulting damage. Repeated scans at increasing fluence were used to quantify the performance of three candidate coating designs.

- S. Skupsky, R. Betti, T. J. B. Collins, V. N. Goncharov, D. R. Harding, R. L. McCrory, P. W. McKenty, D. D. Meyerhofer, and R. P. J. Town (p. 183) present direct-drive target designs for both the NIF and OMEGA. Their calculations show that the use of CH foam shells that are wetted with DT fuel improves laser absorption, leading to better implosion stability and higher neutron yield in comparison to the more-conventional all-DT designs. The techniques necessary to perform "wetted-foam" implosions are being developed.

- R. Sobolewski (p. 188) reviews various concepts for the creation of ultrafast input/output (I/O) interfaces suitable for implementation of digital superconducting electronics in ultrafast telecommunication routers. Separate sections describe the progress in the development of multi-GHz-bandwidth, optical-to-electrical (input), and electrical-to-optical (output) transducers. The article ends with a brief summary, including a personal assessment of the current state of the art in superconducting optoelectronics.

- F. Y. Tsai, D. R. Harding, S. H. Chen, and E. L. Alfonso (p. 196) are working on the development of polyimide as an ablator material for inertial confinement fusion (ICF) targets because of its superior mechanical and thermal properties. They report on a parametric study of the fabrication techniques used to produce spherical polyimide shells using a vapor-deposition polymerization (VDP) method. The production rate, yield, and reproducibility of the process were optimized so that polyimide shells can be reproducibly prepared with dimensions required for ICF targets.

- This volume concludes with reports on LLE's Summer High School Research Program (p. 206), the FY01 Laser Facility Report (p. 208), and the National Laser Users' Facility News (p. 210).

Thomas H. Hinterman
Editor

Wide-Dynamic-Range "Neutron Bang Time" Detector on OMEGA

Introduction

Measurements of the neutron emission from inertial confinement fusion[1] (ICF) implosions provide important information on the target performance, which can be compared directly with numerical models. Targets filled with deuterium (D_2) or a deuterium–tritium (DT) mixture are heated either by direct laser illumination or by soft x-ray radiation in a laser-heated hohlraum. In the resulting implosion, the target is compressed to conditions under which thermonuclear fusion occurs. Fuel atoms undergoing fusion release energetic charged particles, photons, and neutrons. The time of peak neutron emission—the "neutron bang time"—is very sensitive to the details of the energy absorption and the hydrodynamic response of the target. Several detectors that measure the neutron bang time[2–4] have been described in the literature. These include a fast (<25 ps) streak camera–based neutron temporal diagnostic[5] (NTD), which is also capable of resolving the details of the neutron burn history. The NTD is currently installed on LLE's OMEGA laser. It needs a minimum neutron yield $>10^9$ to measure the bang time and is incompatible with D_2 cryogenic target experiments due to mechanical constraints. These drawbacks, plus the complexity and cost of streak camera–based measurements, motivated the development of an alternative neutron bang time detector. This article describes a simple, low-cost, wide-dynamic-range, neutron bang time (NBT) detector that has been developed to complement the capabilities of the NTD.

Setup of the Detector System

The NBT is shown schematically in Fig. 88.1. It is composed of two detector channels to increase the dynamic range of the instrument, an optical fiducial system to cross-time the

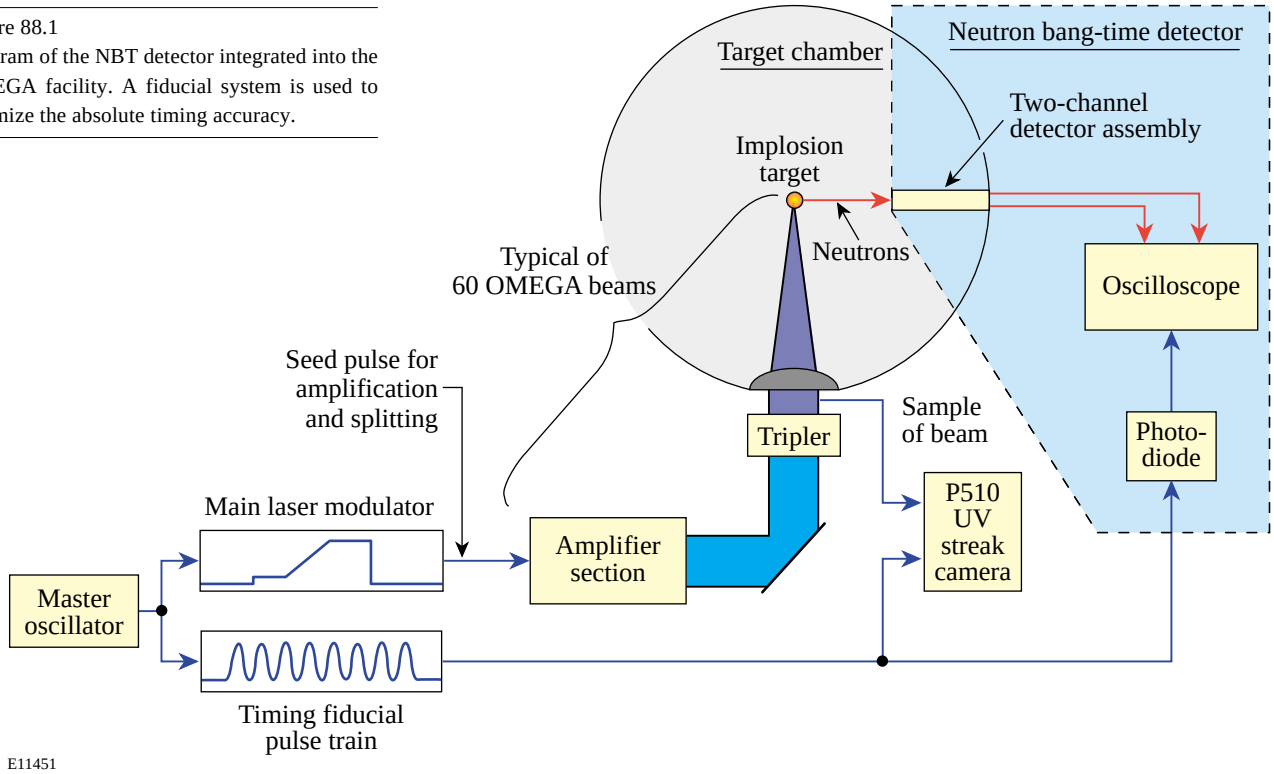

Figure 88.1
Diagram of the NBT detector integrated into the OMEGA facility. A fiducial system is used to optimize the absolute timing accuracy.

diagnostic to the laser pulse, and a fast digitizing oscilloscope. As shown in Fig. 88.2(a), each channel of the NBT system consists of a fast, quenched plastic scintillator (Bicron BC-422Q[6]) coupled to a photomultiplier tube (PMT; Hamamatsu H5783[7]). The H5783 PMT uses an integrated high-voltage power supply that requires only a 15-V dc input. This voltage is supplied through the signal cable using two high-bandwidth bias tees[8] to avoid ground loops and electromagnetic interference (EMI) noise pickup on the dc feed. The gain of the PMT is set by a voltage divider based on a reference voltage supplied by the H5783 to optimize the signal-to-noise ratio of the detection system. Both channels are packaged into a lead housing with copper foil wrapping to provide x-ray and EMI shielding. The efficient x-ray shielding and EMI shielding makes it possible to use the NBT as a secondary neutron or hard x-ray detector in an energy range above 500 keV.[9]

As is shown in Fig. 88.2(b), the NBT detector assembly is positioned approximately 55 cm from the target chamber center (TCC) in a 3.8-cm-diam reentrant tube. Due to the small diameter of the reentrant tube, the second channel is located behind the first along the flight path of the neutrons produced in the target. This does not reduce the sensitivity of the back channel because of the long mean free path of the energetic neutrons in matter. To maximize the dynamic range of the system, different-sized scintillator volumes were selected for

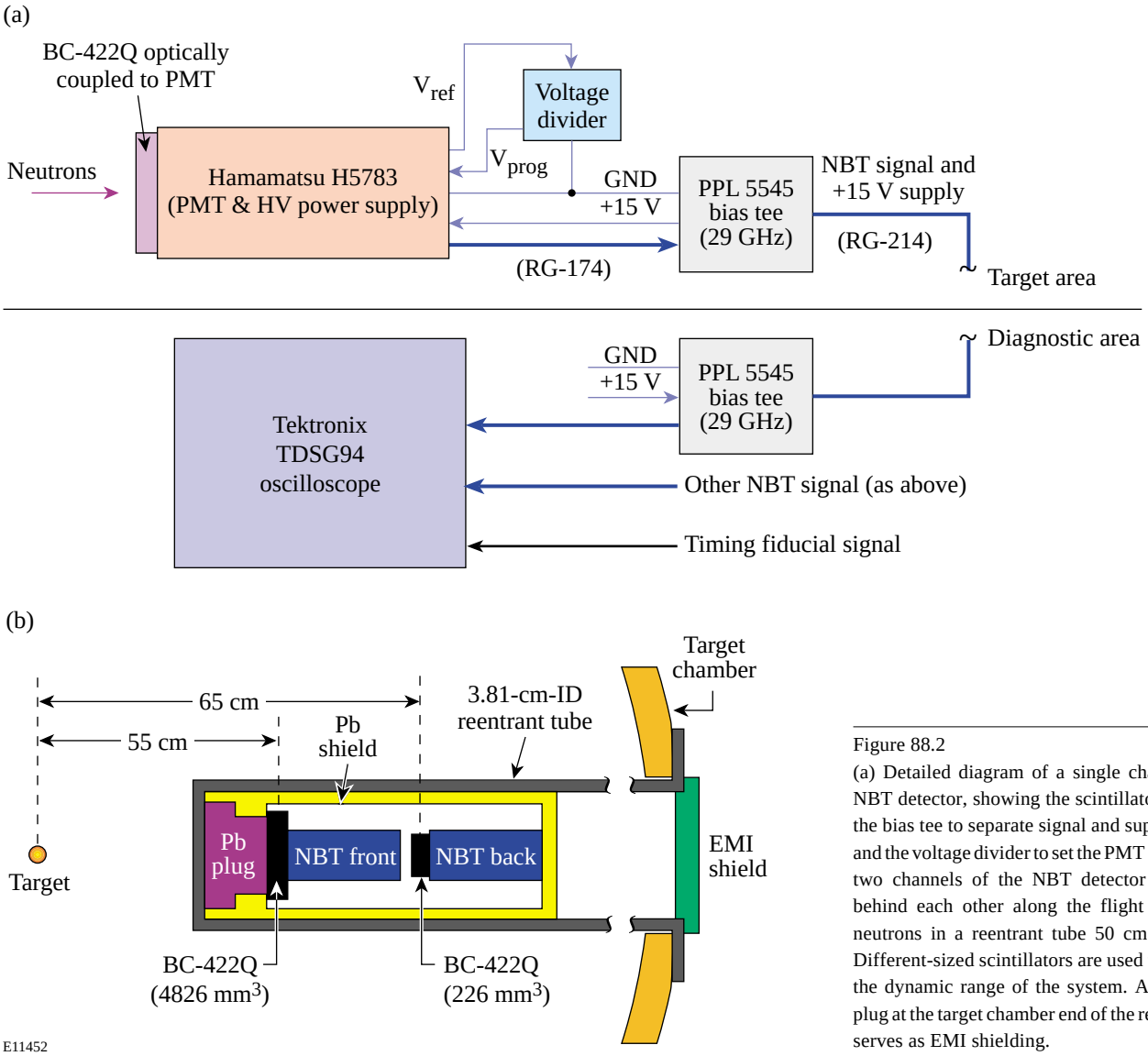

Figure 88.2
(a) Detailed diagram of a single channel of the NBT detector, showing the scintillator, the PMT, the bias tee to separate signal and supply voltage, and the voltage divider to set the PMT gain. (b) The two channels of the NBT detector are located behind each other along the flight path of the neutrons in a reentrant tube 50 cm from TCC. Different-sized scintillators are used to maximize the dynamic range of the system. An aluminum plug at the target chamber end of the reentrant tube serves as EMI shielding.

each NBT channel, 4820 mm^3 for the front channel and 230 mm^3 for the back channel. The signals from the two NBT channels are recorded on separate channels using a four-channel Tektronix TDS694,[10] 3-GHz digital oscilloscope at a sampling rate of 10 GS/s.

Absolute timing of the neutron bang time to better than 100 ps is accomplished using the OMEGA optical fiducial system. The fiducial pulse train consists of eight peaks spaced 548 ps apart and is synchronized to the shaped OMEGA laser pulse with a jitter of less than 20 ps. The optical fiducial is amplified separately from the main laser pulse and delivered to numerous system diagnostics. The fiducial pulse train is recorded on a separate channel of the NBT oscilloscope using a fast photodiode and also on the P510 ultraviolet streak camera,[11] which measures the laser pulse shape. The common optical fiducial serves as a reference for both the neutron signal and the laser pulse, enabling very accurate timing of the NBT signals.

Characterization of the NBT Components

The impulse response of the PMT was measured using a 100-fs laser pulse at 400-nm wavelength recorded on a 1-GHz sampling scope and found to be $\tau_{rise} = 940$ ps. Using the well-known relation

$$\tau_{rise}^{PMT} = \sqrt{\tau_{rise}^2 + \tau_{scope}^2}$$

with $\tau_{scope} = 350$ ps[10] describing the rise time of the scope, the rise time of the PMT is found to be $\tau_{rise}^{PMT} = 650$ ps, in excellent agreement with the value given by the manufacturer.[7]

A low-jitter timing reference signal is critical to accurate measurement of the neutron bang time because the electrical oscilloscope trigger signal has a jitter relative to the laser pulse in excess of 100 ps. The simple solution of routing an optical fiducial fiber into the NBT detector and optically adding the fiducial pulse train to the scintillator signal does not provide a high-quality fiducial signal at the oscilloscope because the rise time of the PMT is slower than the fiducial peak spacing of 548 ps. Recording the optical fiducial pulse train using a high-bandwidth photodiode on a dedicated oscilloscope channel provides a high-quality fiducial signal where every fiducial peak is clearly resolved. The use of a separate channel for the fiducial does not degrade the timing accuracy significantly because the jitter between two channels of the TDS694 is reported by the manufacturer to be less than 10 ps. Sub-pixel resolution of the fiducial timing is accomplished by fitting a pulse train of eight Gaussian pulses spaced at the well-characterized period of $d_t = 548$ ps:

$$\text{fidu}(t) = \sum_{i=0}^{7} a_i \exp\left\{-\left[t - \left(t_0 + i \times dt\right)\right]^2 / 2\sigma\right\}$$

to the recorded signal. Here a_i is the amplitude of each fiducial peak, t_0 is the time of the first fiducial pulse, and σ is the width of an individual fiducial pulse. An example of the fiducial signal together with the fitted Gaussian pulse train is presented in Fig. 88.3 showing very good agreement between signal and fit.

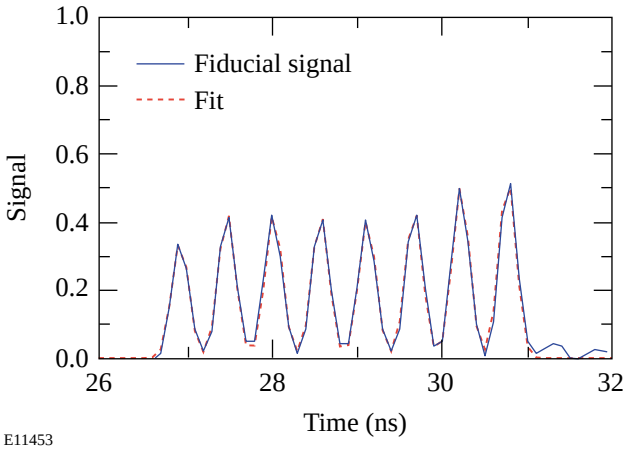

Figure 88.3
Optical fiducial and corresponding fit as recorded on the TDS694 oscilloscope. The high bandwidth of the oscilloscope makes it possible to see each individual fiducial pulse and to get a high-quality fit to obtain sub-pixel time resolution.

Because the output voltage of the PMT is limited to 5 to 10 V, EMI noise pickup effectively limits the dynamic range of each NBT detector channel. Several different shielding layers are used to limit the EMI noise to an acceptable level. The PMT is electrically isolated from the target chamber using the signal cable as its ground connection to the oscilloscope. The use of bias tees avoids ground loops in the dc power feed for the integrated PMT/high-voltage power supply. The lead housing was covered with a layer of Cu foil and grounded to the target chamber. The feedthrough holes for the signal cables were made as small as possible to limit high-frequency EMI penetration of the NBT housing. Finally, to improve the shielding, the reentrant tube was covered with an aluminum plug with only two small openings for the two signal cables. This

combined EMI shielding reduces the pickup noise from several 100 mV down to less than 10 mV for the front channel and less than 40 mV for the back channel.

The recorded neutron signal is broadened by several different mechanisms. Because the neutrons are produced at a high temperature, thermal broadening leads to a Gaussian shape of the arrival times. The plastic scintillator has a very short rise time followed by a relatively slow exponential decay.[6] Scattering processes in the housing and lead shielding also create a tail in the neutron signal that has an effect similar to the scintillator decay. The effect of the finite neutron transit time through the scintillator[12] is less important for determining the bang time than it is for measuring the neutron-averaged ion temperature and can be approximated by a Gaussian for simplicity. The electronic part of the instrument response, which can be described also by a Gaussian, results from the finite bandwidth of the photomultiplier tube, the cable, and the oscilloscope.

Overall, the measured signal $m(t)$ can be approximated by a convolution of a Gaussian $g(t)$ and an exponential decay $d(t)$, as described in detail in Ref. 12:

$$g(t) = \frac{A}{\sqrt{2\sigma}} \exp\left[-\frac{(t-t_1)}{2\sigma}\right],$$

$$d(t) = \frac{1}{\tau} \exp\left(\frac{-t}{\tau}\right),$$

$$m(t) = g(t) \otimes d(t),$$

$$m(t) = \frac{A}{2\tau} \exp\left[-\frac{(t-t_1)}{\tau}\right] \times \exp\left(\frac{\sigma^2}{2}\right) \left\{1 + \operatorname{erf}\left[\frac{(t-t_1) - \sigma^2/\tau}{\sqrt{2\sigma^2}}\right]\right\}.$$

This function is fitted to the measured signal to improve the accuracy of the bang-time determination, especially in situations of low signal-to-noise ratio (see Fig. 88.4). Because the decay time of the scintillator and the neutron scattering effects are identical for every shot, a best-fit decay time can be determined once and used to analyze all of the data. The value used for this setup is $\tau = 1.5$ ns for both the front and the back channels. The signal amplitude A, arrival time t, and signal width σ change from shot to shot and are fitted for every measurement to optimize timing accuracy.

Figure 88.5 shows the dynamic range in D_2 neutron yield for the current two-channel NBT setup. To show more clearly the limits of the linear PMT response, the NBT signal is shown in amplitude rather than collected charge (which would be more appropriate for a neutron-yield detector). In collected

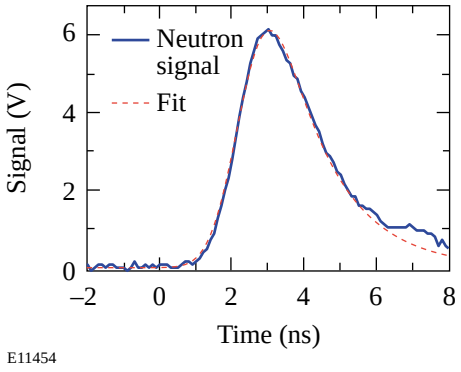

Figure 88.4
Neutron signal and corresponding fit on one channel of the NBT detector.

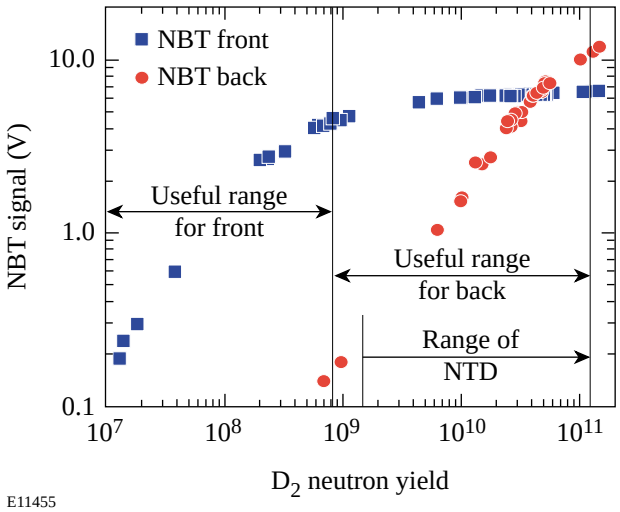

Figure 88.5
Demonstrated dynamic range of the two-channel NBT detector setup. The detection threshold for the front channel is set by the yield that results in a single neutron hit. The threshold for the back channel is determined by the EMI noise pickup.

charge, the PMT's show an even larger dynamic range that eventually distorts the temporal pulse shape. This makes it very difficult to determine the pulse arrival time and introduces large errors. The dynamic range for DT neutrons is very similar to the D_2 neutron dynamic range because, while the higher neutron energy results in a higher average signal per interacting neutron, the effect is mostly offset by the lower interaction cross section.

The front channel is relatively immune to EMI noise because even a single neutron hit results in a signal of the order of 100 mV due to the high PMT gain in the front channel. The EMI pickup noise affects mostly the back channel. A useful dynamic range from about 1×10^7 to 1×10^{11} can be realized in the present two-channel configuration.

Temporal Calibration and Bang Time Accuracy

The front NBT channel can be temporally calibrated using the hard x-ray emission from a Au target irradiated with a short (100 ps) laser pulse at best focus. To obtain a measurable signal for this calibration, the lead shield in front of the detector is replaced by a lead shield with a small hole. Previous experiments using the NTD have shown that the x-ray pulse closely follows the temporal shape of the laser irradiation.[5] Figure 88.6 shows an x-ray-induced signal recorded by the front-channel NBT, a curve fit to this signal using the expression described in the previous section, and the shape of the 100-ps laser pulse as recorded on the OMEGA UV streak camera system.[11] The effects of the limited bandwidth and the noise on the recorded signal are clearly seen, but the accuracy of determining the signal peak is improved considerably by the fitting procedure. The discrepancy that is apparent between the signal and the fit at the end of the pulse is attributed to the use of the expression that was derived for neutrons. Scattered x rays do not change speed as neutrons do, so the tail-off that is characteristic of the neutron signal is not present on the x-ray signal. This effect contributes approximately σ_{calib} = 50 ps uncertainty to the calibration.

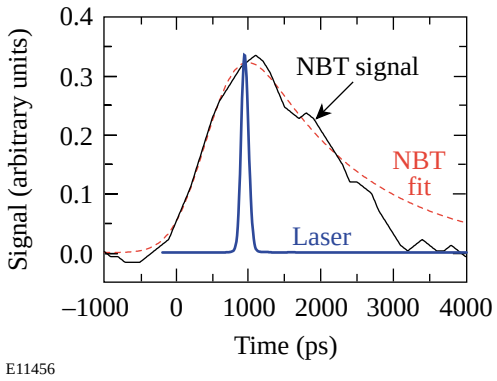

Figure 88.6
Front-channel NBT signal and corresponding fit for a hard x-ray emission produced by a 100-ps laser pulse irradiating a gold target at best focus. The 100-ps laser pulse is shown for comparison.

The x-ray calibration can be easily carried over to the neutron measurements using the propagation delay difference from the TCC to the scintillator between x rays and neutrons:

$$\Delta t_n = L_{\text{scint}}\left(\frac{1}{v_n} - \frac{1}{c}\right),$$

where $v_n^{D_2} = 2.16$ cm/ns and $v_n^{DT} = 5.12$ cm/ns are the neutron velocities and L_{scint} = 55 cm (the distance between TCC and the scintillator). A measurement uncertainty in the scintillator distance of the order of 1 mm is estimated. This corresponds to a calibration error of $\sigma_{\text{dist}}^{D_2} = 50$ ps for D_2 and $\sigma_{\text{dist}}^{D_2} = 20$ ps for DT neutrons. The scintillator distance can be measured *in situ* using the arrival-time difference between DT and D_2 neutrons for implosions of nominally identical bang time and was found to agree within the measurement error of the geometric measurement.

The back channel cannot be calibrated using this x-ray technique because the PMT and bias tee of the front channel effectively shield the back-channel detector from the hard x rays produced by the timing target. This channel can be cross calibrated to either the front channel in the common range of sensitivity or to the NTD. The very high accuracy of the NTD (<20 ps) provides a good measure of the bang time uncertainty of the NBT system. Figure 88.7 shows the cross-calibration of the back channel of NBT and NTD using many targets shots with D_2-filled plastic capsules. A very good correlation between the NTD and back-channel NBT data is observed, with a spread of σ_{back} = 50 ps. A correlation of similar quality is found between the front and back channels of the NBT detector in the common range of sensitivity. Given the 650-ps rise time of the PMT, this is a very good agreement.

Because both NBT channels are analyzed by the same method, it is safe to assume that the bang time uncertainty from fitting the front-channel NBT data is the same as the measured back-channel spread: σ_{fit} = 50 ps. Adding the contributions from the x-ray calibration, σ_{calib}, σ_{dist}, and the uncertainty of

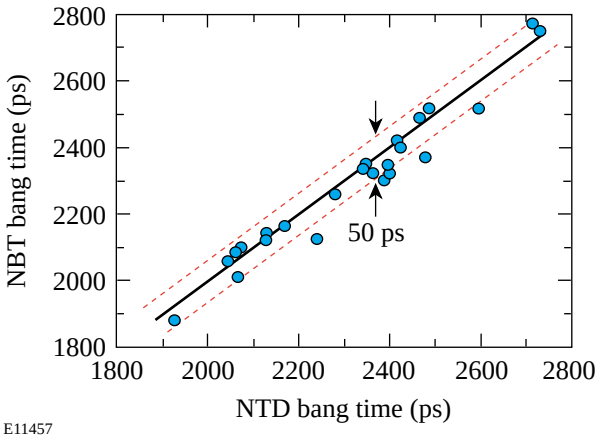

Figure 88.7
Cross-calibration between the back NBT channel and NTD. A very good correlation between NTD and NBT is observed with a rms difference of only 50 ps.

the bang time determination σ_{fit} in quadrature results in an overall absolute neutron bang time accuracy of $\sigma_{front} \leq 100$ ps for the x-ray-calibrated front NBT channel.

Summary and Conclusions

A simple, low-cost, two-channel neutron bang time detector having a wide dynamic range has been developed for OMEGA to complement the capabilities of the streak camera–based NTD. This instrument is able to measure the neutron bang time of D_2- and DT-filled capsules at a neutron yield between 10^7 and 10^{11} with an absolute timing accuracy of better than 100 ps, using hard x rays to calibrate the system. A high-stability fiducial system and a high-bandwidth, fast digitizing oscilloscope are both essential to achieve this precision. Neutron bang time uncertainty as low as 50 ps has been demonstrated using cross-calibrations to a higher-precision instrument such as the NTD. This level of accuracy allows the modeling of the implosions to be effectively guided using hydrocode calculations.

ACKNOWLEDGMENT

This work was supported by the U.S. Department of Energy Office of Inertial Confinement Fusion under Cooperative Agreement No. DE-FC03-92SF19460 and the University of Rochester. The support of DOE does not constitute an endorsement by DOE of the views expressed in this article.

REFERENCES

1. J. Nuckolls *et al.*, Nature **239**, 139 (1972).
2. N. Miyanaga *et al.*, Rev. Sci. Instrum. **61**, 3592 (1990).
3. T. J. Murphy and R. A. Lerche, *ICF Quarterly Report* **3**, 35, Lawrence Livermore National Laboratory, Livermore, CA, UCRL-LR-105821-93-1 (1992).
4. R. A. Lerche, D. W. Phillion, and G. L. Tietbohl, in *Ultrahigh- and High-Speed Photography, Videography, and Photonics '93*, edited by P. W. Roehrenbeck (SPIE, Bellingham, WA, 1993), Vol. 2002, pp. 153–161.
5. R. A. Lerche, D. W. Phillion, and G. L. Tietbohl, Rev. Sci. Instrum. **66**, 933 (1995).
6. Bicron Newbury, Newbury, OH 44065-9577.
7. Hamamatsu Photonics K.K. (http://www.hamamatsu.com).
8. Picosecond Pulse Labs, Boulder, CO 80301.
9. V. Yu. Glebov, D. D. Meyerhofer, C. Stoeckl, and J. D. Zuegel, Rev. Sci. Instrum. **72**, 824 (2001).
10. Tektronix Corporation, Beaverton, OR 97077.
11. Laboratory for Laser Energetics LLE Review **87**, 109, NTIS document No. DOE/SF/19460-397 (2001). Copies may be obtained from the National Technical Information Service, Springfield, VA 22161.
12. T. J. Murphy, R. E. Chrien, and K. A. Klare, Rev. Sci. Instrum. **68**, 610 (1997).

Functional Damage Thresholds of Hafnia/Silica Coating Designs for the NIF Laser

Introduction

LLE's Optical Manufacturing Group (OMAN) has been tasked with coating several types of optics for use on the National Ignition Facility (NIF) laser system. Until recently, the standard quality assurance technique for coating large optics has been to process a smaller "witness" optic along with the large optic.Tests and inspections performed on the witness optic were used to certify the quality of the larger optic. This approach reduces costs and avoids damage to the production part. (The NIF optics used in this effort were 412 mm square. The corresponding witness optic would be 51 mm in diameter.)

One of the process factors that affects the durability of an optic is the cleanliness of the substrate prior to deposition of the thin-film, high-reflective coating. A particle on the substrate surface that is coated over creates a nodule that is much more likely to fail than any other portion of the coating. Current substrate cleaning and handling methods are so effective, however, that the number of particles per unit area present prior to coating is very small. As a result, the small-surface-area witness substrates have become statistically less likely to represent the damage properties of full-sized parts. For this reason, OMAN has been conducting a damage-testing experiment on its mirror coatings using full-sized NIF substrates. A large-area conditioning (LAC) station designed by LLNL was used for this testing.

The LAC station facilitates testing of full-sized samples by automatically scanning the test optic relative to an optical system that simultaneously irradiates a small area and detects any resulting damage. Repeated scans at increasing fluence were used to quantify the performance of candidate coating designs.

Three candidate high-reflector, thin-film coating designs using hafnia and silica were developed for the LM7E mirrors on the NIF laser. Mirrors were prepared with each candidate and damage tested to provide data that NIF planners could use, along with spectrophotometric results, to determine which coating design would work best for the NIF laser.

Objectives and Scope

Coating durability is the main issue investigated in this experiment. The coatings must be durable enough to survive the maximum fluence of the NIF's main beam (fluence being beam pulse energy per square centimeter). The reflectance/transmittance properties at other wavelengths are a secondary issue because the NIF plans to use alignment lasers that will operate on a different wavelength than that of the main beam. The selection of that wavelength can be based on the coating designs of the various optics in the system. Because variations in the coating designs may have positive or negative impact on damage thresholds, the optic's spectral performance and damage threshold are linked. The objective of this experiment is to find the best combination of coating durability and overall spectral performance for the NIF laser.

LLNL's definition of damage is "Functional Damage Threshold (FDT) is the minimum fluence at which a damaged optic degrades the performance of the NIF laser."† This represents a departure from traditional damage testing. Using this criterion meant that our first objective was to create some form of damage, and our second objective was to find the practical limit at which the optic could continue to function with that damage present. When the FDT is found, the resulting damage is termed "failure damage." Once failure damage has occurred, that damage site is likely to grow at fluences lower than the FDT. Figure 88.8(a) shows a damage site that has not reached its FDT; Fig. 88.8(b) shows a damage site that has reached its FDT.

If testing is continued on a failure damage site at the FDT fluence, that site will grow very rapidly. However, if the fluence is decreased from the FDT, the rate at which the site grows will decrease correspondingly. The growth threshold fluence (GTF) is the lowest fluence at which a site will continue to grow after it has sustained failure damage. Below the GTF, the size of the failure damage site will remain stable.

†This definition came from a presentation by C. Stolz at LLE regarding NIF definitions of damage.

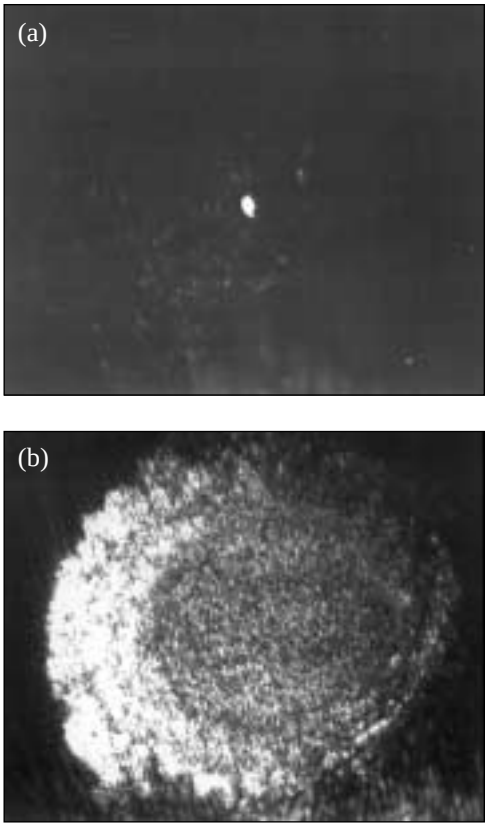

G5403

Figure 88.8
(a) A stable damage site ~0.13 mm in diameter. (b) The same site, after reaching it's FDT. During a single miniscan it grew to ~2.3 mm in diameter.

At the GTF, growth occurs at the lowest rate that can be positively detected. The GTF is always lower than the FDT.

During the course of the experiment, it was observed that the rate at which a damaged site grows after reaching the FDT is a function of the fluence used. At the GTF, the damage site is growing slowly enough that its size can be accurately measured. At fluences above the GTF, this becomes more difficult since the damage size quickly grows larger than available equipment can accurately measure. In order to obtain data for large numbers of shots, growth-rate testing was done at the GTF.

In summary, if the FDT, GTF, and the growth rate at the GTF are known, the fluence range over which the optic can perform without being damaged is also known. In addition, should that optic experience failure damage, the resulting operating limits can be estimated. These data can be used along with spectrophotometric results as criteria to select a coating design that is most suitable for the NIF optics.

Coatings

Three coating design options were tested on BK-7 substrates against a requirement of $Rs_{1054\ nm} > 99.5\%$ at 42.2° incidence. The NIF will be aligned with a UV laser, with a wavelength between 351 nm and 405 nm. (In this section, $Rs_{wavelength}$ stands for the reflectance in *s*-polarization at the wavelength in the subscript.) The different LLE coating designs try to maximize reflection about 351, 374, or 405 nm while maintaining the 1054-nm specification. They were named the Type-I, -II and -III coatings, respectively.

Types I and II used 22 alternating layers of HfO_2 and SiO_2 to form a first-order stopband reflector at 1054 nm. The refractive indices at 1054 nm are 1.993 for hafnia and 1.456 for silica. This resulted in physical thicknesses of 140.4 nm and 203.9 nm for the Type-I, high- and low-index quarter waves, respectively.

The Type-I and Type-II designs differed in that the stopband of Type II was shifted to 1078 nm, enabling the third-order reflectance $Rs_{374\ nm}$ to be >94%. In this design, the reflectance at 1054 nm is still above the specification but a slightly higher E-field is allowed to stand at the substrate/coating interface. Optimally a coating has E-field peaks occurring within a given layer of coating material instead of at an interface since the interface is structurally the weaker of the two. The spectral characteristics of the two types of coatings are shown in Fig. 88.9.

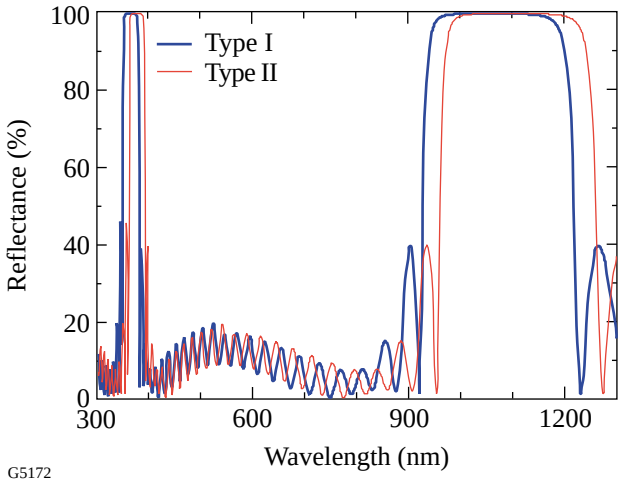

G5172

Figure 88.9
Reflectance versus wavelength for Type-I and -II coatings. The Type-II design at 42° incidence has a third-order stopband at 374 nm versus 351 nm for Type I.

The Type-III design is a computer-optimized, 32-layer design, with all layers of non-quarter-wave thickness. This was necessary to obtain $Rs_{351\ nm} < 7\%$ and $Rs_{405\ nm} > 94\%$ while maintaining $Rs_{1054\ nm} > 99.5\%$. Figure 88.10 shows the spectral characteristics of the Type-III design.

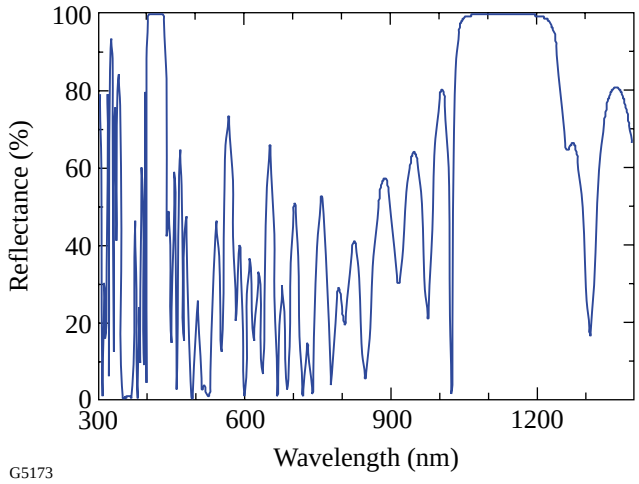

Figure 88.10
Reflectance versus wavelength for Type-III coating. The Type-III design is a non-quarter-wave design achieving high reflectance at 1054 nm and 405 nm while transmitting 351 nm at 42° incidence.

The coatings were deposited using electron-beam sources placed 120 cm below the planetary substrate plane. Hafnia layers were deposited at 0.16 nm/s by the evaporation of pure hafnium metal using a 7.5-kV electron-beam gun. This provided a consistent spit-free vapor in a 1×10^{-4}-Torr oxygen environment. Silica layers were deposited at 0.44 nm/s in 5×10^{-5} Torr of oxygen using an electron-beam gun at 6.0 kV. Achieving the correct oxygen pressure during silica deposition is important in balancing stresses for the two materials in their operating environment, which is air controlled to 40% relative humidity.

Experiment

The experiment was conducted using the LLNL-designed LAC station. The LAC station is capable of automating the entire damage testing and damage site detection process with a minimum of operator input. It consists of a precision *x*–*y* translation stage (shown in Fig. 88.11) that supports and positions the optic being processed, a fixed optical system for optic monitoring, a laser table that delivers the damage-testing beam and monitors beam characteristics, and a computer controller that operates the system and logs data sets.

Figure 88.11
The LAC station monitors an optic's surface quality at the same time it is being damage tested. The translation stage shown here can handle a variety of NIF optics, such as a NIF polarizer, which is 810 × 420 mm. Pictured on the stage is an LM2 substrate, approximately 420 × 420 mm.

The optical system that monitors the test optic is mounted in a fixed position in front of the translation stage (see Fig. 88.12). It is aligned so that the point at which its optical path intersects the front surface of the optic is the same point at which the damage-testing beam strikes the optic and is reflected away into a beam dump. This system uses a 633-nm diode laser to monitor scatter. A small reflector, mounted to the front of the telescope, reflects the diode's beam toward the

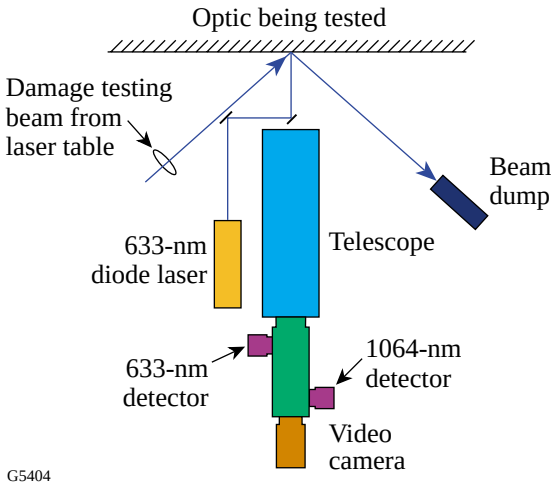

Figure 88.12
Optic monitoring system.

optic. If there is no scatter, i.e., the optic surface is undamaged, the diode beam will reflect back into this small reflector. If there is scatter, light will miss the reflector and be collected by the telescope. A 633-nm detector mounted to the back of the telescope collects the scatter data and relays it to the computer, which produces a scatter map of the optic.

In addition to the 633-nm detector, there is also a 1064-nm detector. Should the damage-testing beam strike the optic's surface and cause damage, 1064-nm light will scatter instead of reflecting into the beam dump. This scattered light is collected by the telescope and seen by the 1064-nm detector, which relays that data to the computer, which, in turn, produces what is called a "plasma map." A video camera completes the system; its output is sent to a video monitor and to the computer controller. The computer uses this input to capture digital still images when requested by the operator.

The laser table (shown in Fig. 88.13) includes the damage-testing laser (characteristics discussed below), a camera, and a power meter. The camera monitors the beam's cross section, while energy levels are measured via the power meter head. Both sets of data are relayed to the LAC computer program, which calculates the geometric characteristics of the beam based on the camera data and then combines it with the measured energy levels to determine the instantaneous and average fluence of the beam. All of these results are logged by the program.

An OMAN addition to the LAC system was a digital video recorder. The signal was taken from the line connecting the video monitor to the computer. The recorder was used to document the actual damage as it occurred when a miniscan was performed (miniscans are defined below).

The experiment was conducted using the LAC in a class-1000 clean-room environment at LLE as follows: Damage tests were performed by raster-scanning a *Q*-switched Spectra Physics Quanta-Ray Pro Nd:YAG laser emitting 1064-nm light with a 30-Hz repetition rate and a 10-ns pulse length. Beam characteristics (energy/shot and beam cross section) were sent directly from the data acquisition hardware to the LAC program. The program automated all pertinent calculations and controlled the substrate position with respect to the laser beam. The program scales the fluences it reports to a 3-ns pulse length, using the following experimentally derived scaling equation:

$$F_x = F_y(x/y)^{0.35}, \tag{1}$$

where x and y are the two pulse lengths of interest and $F_{x \text{ or } y}$ is the fluence at that pulse length.

During the procedure described below, the clear aperture of the optic was divided into two halves: one half was reserved for *s*-polarization testing, the other for *p*-polarization. Damage testing was performed on one half of the optic at a time.

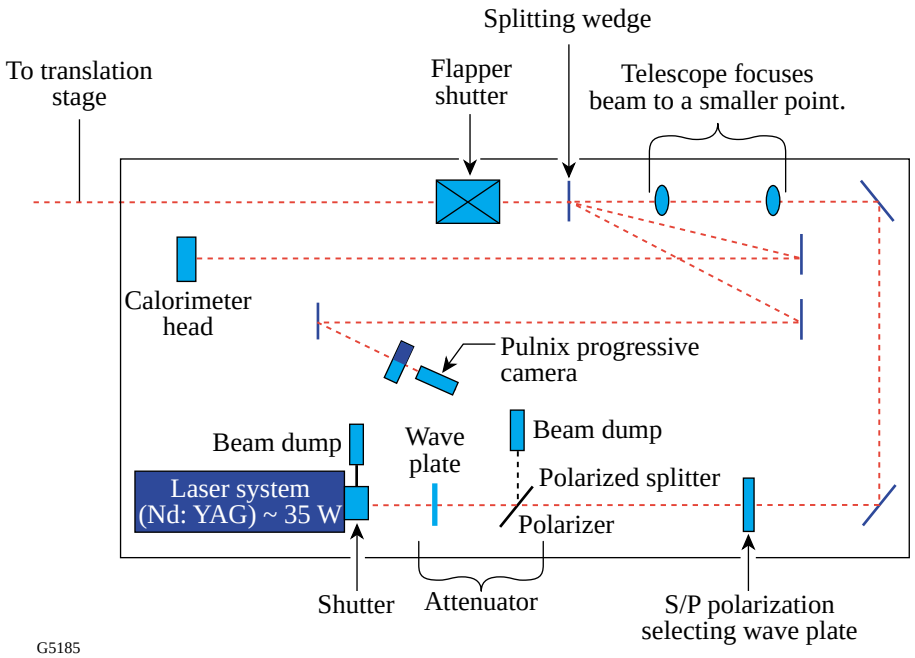

Figure 88.13
Schematic of the LAC laser table layout. The length of the beam path between the splitting wedge and camera is equal to that between the splitting wedge and testing plane.

A full scan was performed first on the half of the aperture being tested. The fluences (scaled to a 3-ns pulse) used for these scans were 15, 18, 22, 25, 30, and 35 J/cm^2. After each full scan was completed (approximately 6 h), the scatter map of the optic's surface was examined for possible defect sites. The optic was also examined by eye for possible defect sites.

Once a defect site (or potential defect site) was found, it was made the center of a "miniscan." A miniscan is a 10-mm-wide by 5-mm-tall raster scan, with the candidate defect site at the center. A scatter site was said to be "stable" at a given fluence if no growth occurred after three sets of five miniscans (15 miniscans total) were done on the site. If the site was determined to be stable, another full scan was done at the next-highest fluence. The miniscan process was then repeated at that fluence. This fullscan/miniscan process was repeated until the damage site became unstable.

Once a scatter site was found to be unstable (damage growth occurred prior to the 15th miniscan), the fluence causing the damage growth was recorded as the FDT and determination of the GTF was started.

The procedure used to determine the GTF is the same as that used to determine the FDT, with two exceptions: (1) no full scan is performed, and (2) the first miniscan fluence is 12 J/cm^2 instead of 15 J/cm^2 (the scaled-to-3-ns-fluence steps are 12, 15, 18, 22, and 25 J/cm^2). The same criteria that determined the FDT also apply to the GTF (three sets of five miniscans). If the damage site was found to be stable at 12 J/cm^2, the fluence was increased and the procedure repeated.

Data Gathering

Multiple damage sites were examined on each of the Type-I, -II, and -III optics. A photothermal printer was used to produce images of identified damage sites prior to and after each full scan and group of miniscans. These images were then measured with a circle template and scaled to the appropriate dimensions. It should be noted that one constraint of this method is that only the lateral size of defects, not changes in depth, can be measured; therefore, throughout this experiment, damage growth refers only to a change in dimension tangent to the surface of the optic.

The fluence at which a scan, or group of scans, was performed was also recorded, as well as how many of those scans were performed. These three parameters—lateral defect size, scan fluence, number of scans—were then used for analysis.

Data Analysis

The average growth rate can be determined if an extended number of shots are taken at the GTF. Two sites were tested in excess of 50 raster scans at the GTF. A definite trend in the growth of the damage size could be seen when it was plotted as a function of the number of raster scans. A trend line was fit to the data points, the slope of which is the change in size as a function of raster scans, or the average growth rate.

Figure 88.14 is a plot of the data collected at the GTF at two sites. As is evident, the growth rates of these two sites are nearly identical (roughly 14.0 and 14.4 μm/miniscan) through the course of approximately 120 miniscans.

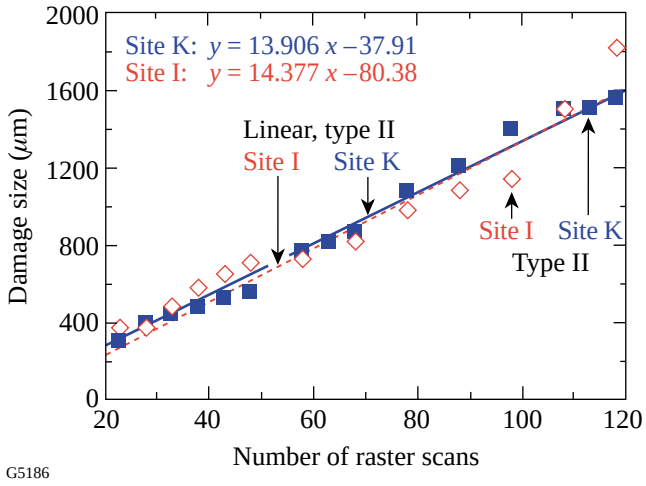

Figure 88.14
Plot of damage size versus number of raster scans at a fluence of 22.5 J/cm^2 for 10-ns pulses.

Results and Conclusion

The results for the Type-I, -II, and -III coated LM7E's are listed in Table 88.I. Each fluence listed is the lowest for its particular category and is scaled from the 3-ns-pulse-length number reported by the LAC program to its 10-ns counterpart. The FDT numbers represent the lowest damage thresholds found on a particular coating design/polarization. For each coating design/polarization combination, a minimum of ten damage sites were investigated.

The following conclusions can be drawn:

1. The damage thresholds of the Type-I coatings were greater than those of the Type-II or -III coatings.
2. The GTF was the same for all three coating designs.

Due in part to the results of this experiment, the NIF project has decided to go with a slightly modified version of the Type-II coating. This "Type-IV" coating differs from the Type II in that the top and bottom three layers of the coating stack are modified. This was done for two reasons. The first is to improve performance over the Type-II design. The second has to do with an additional requirement (not addressed by this experiment) regarding backscattered stimulated Brillion scattering (SBS) and 400- to 700-nm stimulated Raman scattering (SRS) light from the target chamber. Spectral measurements performed by LLNL show the Type-IV design more effectively suppresses SBS and SRS than the Type-II design.

ACKNOWLEDGMENT

This work was supported by the U.S. Department of Energy Office of Inertial Confinement Fusion under Cooperative Agreement No. DE-FC03-92SF19460, the University of Rochester, and Lawrence Livermore National Laboratories under subcontract B399901. The support of DOE does not constitute an endorsement by DOE of the views expressed in this article.

Table 88.I: FDT's and GTF's for the three LM7E mirror designs.

(All 10 ns in J/cm^2)	*p*-pol FDT	*s*-pol FDT	*p*-pol GTF	*s*-pol GTF
Type I	37	42	22	22
Type II	37	33	22	22
Type III	33	33	22	22
The precision of the listed fluences is ±3 J/cm^2.				

High-Gain Direct-Drive Target Designs for the National Ignition Facility

Introduction

Direct drive[1] offers the potential of higher target gain for the National Ignition Facility (NIF)[2] than indirect drive.[3] Direct-drive targets have been designed that reach a gain of 45 in one-dimensional (1-D) simulations using primarily a pure cryogenic DT shell driven on an isentrope where the pressure is three times the Fermi-degenerate pressure ($\alpha = 3$). The sensitivity of this design to laser and target-surface nonuniformities has been studied with two-dimensional (2-D) simulations.[4] At the levels of nonuniformity expected for the NIF, the neutron yield was calculated to be about 70% of the 1-D value, producing a target gain of 30. A second class of targets has the potential of achieving even higher gain. In these designs, the outer portion of the cryogenic DT shell is replaced with a region of low-density CH foam. Liquid DT is "wicked" into the voids of the foam.[5] The advantage of these "wetted-foam" designs over the "all-DT" target is that the presence of higher-Z material (C) in the laser deposition region results in increased laser absorption. For the NIF designs, the laser absorption increases by ~40% (going from 60% absorption in DT to 85% in the wetted foam). For a scaled-down version of the wetted-foam target, which can be examined on LLE's OMEGA laser, the laser absorption is increased by almost a factor of 2, effectively doubling the amount of energy available to drive the target. With the increased laser energy, the capsules can contain an increased amount of fuel. The wetted-foam targets are thicker, providing increased stability, and the additional fuel provides higher neutron yield.

Results–NIF

A comparison between one possible wetted-foam design for the NIF and the base-line "all-DT" design is shown in Fig. 88.15, with the targets drawn approximately to scale. (In Fig. 88.15 and the other figures, distances are labeled in microns and IFAR is the in-flight aspect ratio.) The main result is that the wetted-foam design achieves a 1-D target gain that

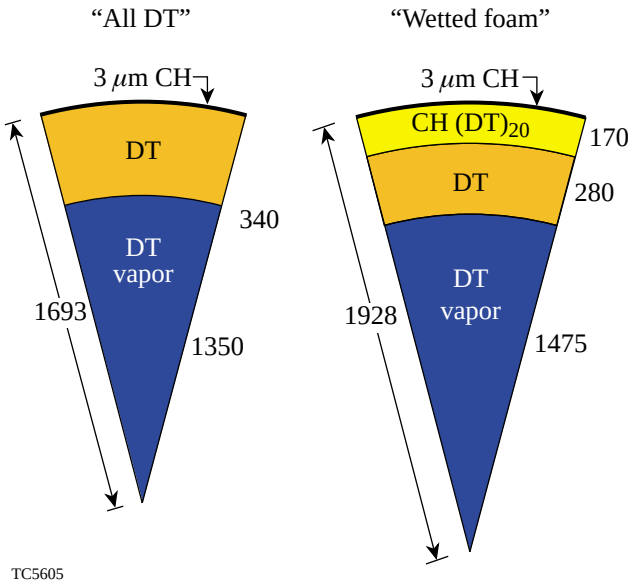

1.5-MJ Designs		
	All DT	Wetted foam
Gain	45	120
Absorption (%)	60	85
ρR (g/cm^2)	1.3	1.7
Adiabat (α)	3	2
Peak IFAR	60	50
Margin	44	32

Figure 88.15
Comparison between the wetted-foam and all-DT direct-drive target designs for the NIF. The wetted-foam design has ~40% higher laser absorption and more than twice the target gain.

is almost three times higher than the gain for the all-DT target. Most of this large increase in target gain is directly related to the increase in target size. The foam target is about 30% thicker, its outer diameter is about 20% larger, and it contains about 80% more fuel. Since the foam target is thicker, it can be driven on a lower adiabat ($\alpha = 2$) than the all-DT target ($\alpha = 3$), without compromising shell integrity during the acceleration phase of the implosion. This, combined with the larger fuel mass, results in a 30% increase in the peak areal density ρR (where ρ is the density and R is the radius) achieved by the fuel (1.85 versus 1.3 g/cm^2). The fraction of fuel burned (or *fractional burnup*) by thermonuclear reactions is roughly proportional to the peak ρR (in this range). The 80% increase in fuel mass combined with a 30% increase in fractional burnup of the fuel increases the target gain by a factor of 2.5 and accounts for most of the increased gain shown in Fig. 88.15.

A preliminary stability analysis of the wetted-foam design shows that this target is more stable than the all-DT target during the acceleration phase of the implosion. Figure 88.16 shows the result of applying a stability postprocessor[6] to the 1-D simulations for these targets. The shell thickness and the size of the mixed region resulting from hydrodynamic instabilities are plotted as functions of time. Both simulations use the same "seeds" for the Rayleigh–Taylor instability caused by laser-beam nonuniformity and target-surface roughness. In these simulations the foam is treated as a homogeneous material. The shell size is four times larger than the mix region for the foam target and three times larger for the all-DT target. This improved margin for stability of the foam design is mainly the result of the increased thickness of the target shell.

A similar stability analysis for the deceleration phase of the implosion showed that the fractional distortion of the hot spot was significantly larger for the foam target than for the all-DT target. This was the result of a lower implosion velocity for the foam target than for the all-DT target: 3×10^7 cm/s versus 4×10^7 cm/s. Because of the lower implosion velocity, the target decelerates for a longer time before the ignition temperature is reached. Lower temperatures during deceleration also reduce the ablative stabilization of the Rayleigh–Taylor growth.[7] These two factors—increased deceleration time before ignition and increased growth rates—result in increased distortion of the hot spot even though the initial seed for deceleration growth is somewhat smaller for the foam design. These stability estimates will be verified with multidimensional simulations.

To achieve greater stability during the deceleration phase, a second foam design with a higher implosion velocity has been developed. This design (target #1 in Fig. 88.17) is smaller, has a thinner shell, and is less massive than the higher-gain wetted-foam design (target #2 in Fig. 88.17) in order to achieve the higher velocity. The foam density was increased from 30 mg/cm^3 to 140 mg/cm^3 to maintain high laser absorption for the smaller target. Because the target is thinner, the adiabat had to be increased from α = 2.0 to α = 2.5 to maintain sufficient stability during the acceleration phase of the implosion. The penalty paid for the increased stability was a reduction in target gain due to the higher adiabat and smaller amount of fuel. Nonetheless, the 1-D target gain for this foam design is still almost a factor of 2 higher than for the all-DT gain: 80 versus 45. A stability analysis for both the acceleration and deceleration portions of the implosion shows distortion comparable to that of the all-DT design, which was calculated to achieve 70% of the 1-D yield.

Results–OMEGA

The high-velocity, wetted-foam design was scaled down to 35 kJ to examine what experiments could be performed using

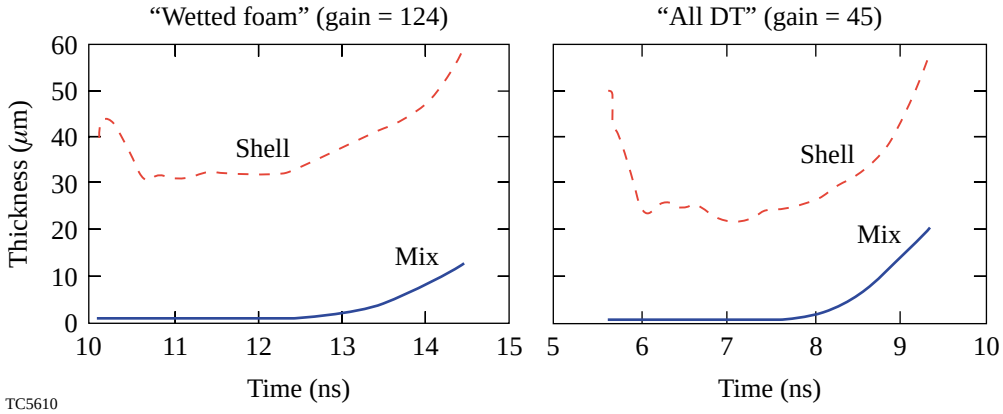

Figure 88.16
Shell thickness and mix thickness as a function of time during the acceleration phase of the implosion for the wetted-foam and all-DT designs shown in Fig. 88.15.

the OMEGA laser. The design was tuned to achieve a target gain of 0.3 with the highest-possible adiabat (for maximum stability during acceleration) and the highest-possible implosion velocity (for the maximum stability during deceleration). The target and pulse shape are shown in Fig. 88.18. A target gain in the range of 0.2 to 0.3 would demonstrate the onset of bootstrap heating. Bootstrap heating is the self-heating process whereby alpha particles from the DT reaction deposit their energy back into the fuel and raise the temperature, resulting in a significant increase in the thermonuclear reaction rate. To be effective, the region of neutron production (hot spot) should be comparable in size to the distance over which alpha particles lose their energy. This corresponds to a ρR of ~300 mg/cm^2. This 35-kJ, wetted-foam design shows a measurable amount of bootstrap heating. The effect of bootstrap heating is seen in Fig. 88.19, which shows the computed neutron yield plotted as a function of variations in the length of the foot of the laser pulse. For the optimal foot length, the neutron yield is highest due to optimal timing of the shocks in the target. To see the effect of bootstrap heating, a second curve in Fig. 88.19 shows

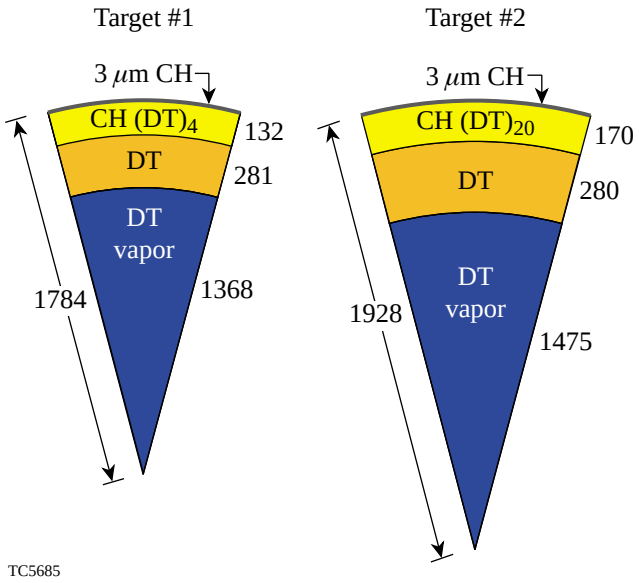

	1.5-MJ Wetted-Foam Designs	
	Target #1	Target #2
Foam (mg/cm^3)	140	30
Gain	81	120
Absorption (%)	90	85
ρR (g/cm^2)	1.4	1.7
Adiabat	2.5	2.0
Margin	48	32
Velocity (cm/s)	4.0×10^7	3.2×10^7

Figure 88.17
Comparison between two wetted-foam designs for the NIF. The smaller target has a higher implosion velocity, resulting in greater stability during the deceleration phase of the implosion.

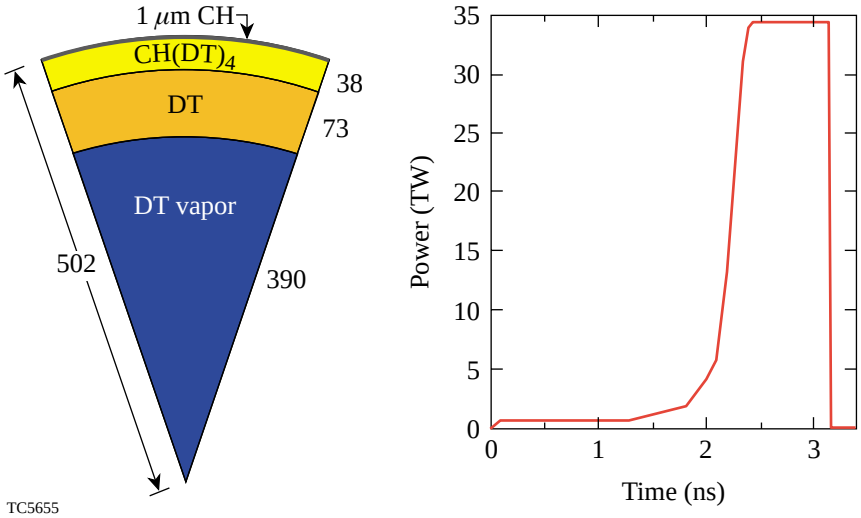

Figure 88.18
A 35-kJ wetted-foam design for experiments on the OMEGA laser. This target is a scaled-down version of the smaller target illustrated in Fig. 88.17.

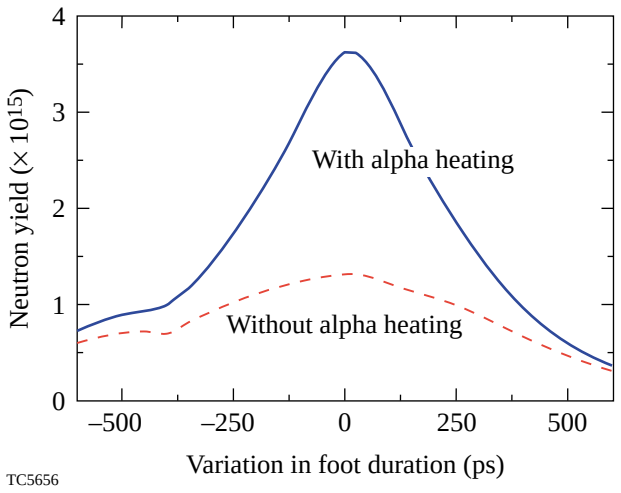

Figure 88.19
The effect of bootstrap heating on neutron yield. Neutron yield is plotted as a function of the length of the foot of the pulse shown in Fig. 88.18. For the optimal pulse length, there is an optimal coalescence of shocks within the fuel, resulting in maximum neutron production. At maximum neutron production there is enough alpha-particle heating of the fuel that the neutron yield is a factor of 3 higher than it would be without this heating.

the neutron yield with alpha-particle heating turned off in the simulation. Under these conditions alpha heating increases the neutron yield by a factor of ~3 at optimal shock timing when the neutron production is largest. Moving away from peak neutron production, the amount of alpha heating becomes too small to significantly increase the temperature. The density and temperature profiles in the fuel at one instant in time during neutron production are shown in Fig. 88.20. The hot region extends close to a ρR of 300 mg/cm^2, which is the expected condition for bootstrap heating.

To observe these effects on OMEGA, improvements in laser uniformity and target quality are required. The levels of nonuniformity from target-surface roughness and laser nonuniformity would have to be typically a factor of 2 to 4 smaller than required for the NIF because the OMEGA targets are about 3.5 times smaller. An initial stability analysis of this target was performed using a stability postprocessor.[6] We used a 0.5-μm inner-surface roughness for the DT ice and the laser imprint corresponding to SSD with 1-THz bandwidth and two color cycles and twice the spectral dispersion that is currently used on OMEGA to seed the Rayleigh–Taylor instability from target-surface roughness and laser nonuniformity. These specifications for the laser and target uniformities are beyond current capabilities on OMEGA, but they should be achievable with extensions of current technology. A plot of shell thickness and mix thickness is shown in Fig. 88.21. At the time of closest approach, the shell is twice as large as the mixed region. This might be adequate but will have to be examined with two-dimensional simulations.

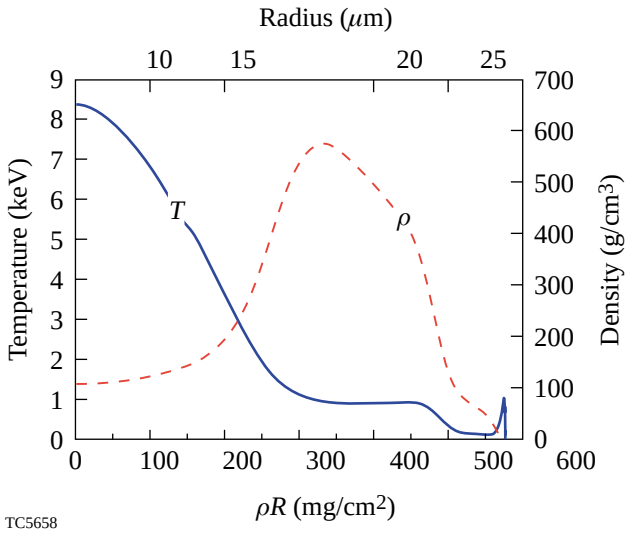

Figure 88.20
Density and temperature profiles at one instant in time during neutron production. The temperature and density profiles of the hot region are characteristic of hot-spot conditions in an igniting target.

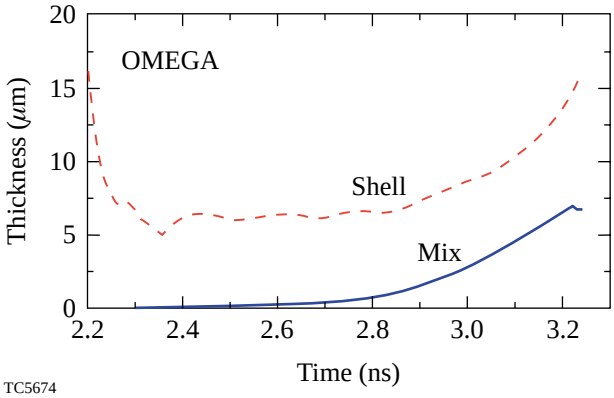

Figure 88.21
Shell thickness and mix thickness as a function of time for the OMEGA wetted-foam design (from Fig. 88.18) during the acceleration phase of the implosion. The laser nonuniformity was a factor of 2 lower than currently achieved on OMEGA, and an inner-surface roughness of 0.5 μm was used.

The design presented here will be scaled down to the lower energies (25 to 30 kJ) that can be expected on OMEGA for pulse shapes similar to that shown in Fig. 88.18. While the signal of bootstrap heating will be less dramatic than that shown in Fig. 88.19, the demonstration that this new type of target can be successfully imploded with a greatly increased laser absorption would be an exciting result with significant implications for direct-drive NIF designs. A program for developing the key areas necessary for wetted-foam implosions is being developed. This includes an investigation of the feasibility of fabricating foam shells of the required quality.

ACKNOWLEDGMENT

This work was supported by the U.S. Department of Energy Office of Inertial Confinement Fusion under Cooperative Agreement No. DE-FC03-92SF19460 and the University of Rochester. The support of DOE does not constitute an endorsement by DOE of the views expressed in this article.

REFERENCES

1. J. Nuckolls *et al.*, Nature **239**, 139 (1972).
2. M. D. Campbell and W. J. Hogan, Plasma Phys. Control. Fusion **41**, B39 (1999).
3. S. E. Bodner, D. G. Colombant, J. H. Gardner, R. H. Lehmberg, S. P. Obenschain, L. Phillips, A. J. Schmitt, J. D. Sethian, R. L. McCrory, W. Seka, C. P. Verdon, J. P. Knauer, B. B. Afeyan, and H. T. Powell, Phys. Plasmas **5**, 1901 (1998).
4. P. W. McKenty, V. N. Goncharov, R. P. J. Town, S. Skupsky, R. Betti, and R. L. McCrory, Phys. Plasmas **8**, 2315 (2001).
5. R. A. Sacks and D. H. Darling, Nucl. Fusion **27**, 447 (1987).
6. V. N. Goncharov, P. McKenty, S. Skupsky, R. Betti, R. L. McCrory, and C. Cherfils-Clérouin, Phys. Plasmas **7**, 5118 (2000).
7. V. Lobatchev and R. Betti, Phys. Rev. Lett. **85**, 4522 (2000).

Ultrafast Optoelectronic Interface for Digital Superconducting Electronics

Introduction

Ultrafast optoelectronics is an acknowledged field of technological importance for the 21st century, and a very large amount of research has been performed on this topic in recent years.[1] It is estimated that by the year 2006 nearly 13% of developed-world households will be connected to Global Internet via interactive broadband fiber services. This requires very high capacity networks with complex switchboards and routers. Current single-wavelength bit rates for optical fibers are between 2 and 6 Gbit/s, with laboratory demonstrations reaching speeds of up to 40 Gbit/s. Implementation of the optical wave division multiplexing (WDM) technique increases the fiber throughput to well above 1 Tbit/s. Time division multiplexing (TDM) is also an obvious, and in many aspects preferable, multiplexing choice for digital signals to increase the fiber throughput capacity. Implementation of TDM will require ultrahigh-speed transmitters in the electrical domain. Superconducting digital electronics is expected to become the processing medium of choice for these optical telecommunication applications.

The highest-speed digital data processing and manipulation can be achieved using superconducting electronics circuitry based on single-flux-quantum (SFQ) logical devices consisting of a combination of resistively shunted tunnel Josephson junctions (JJ's).[2] Low-temperature superconducting (LTS) SFQ digital circuits, fabricated in the standard, Nb tri-layer process with 1.5-μm feature size, have demonstrated clock speeds from 20 to 40 GHz. Further reduction of the linewidth to below 0.8 μm would allow JJ circuits to reach speeds of well above 100 GHz, even in complex designs.[3,4] The road map for the development of SFQ electronics estimates that high-temperature superconducting (HTS) digital circuits should reach 1-THz-range clock rates within the next ten years,[4] and, indeed, 0.7-ps SFQ pulses generated by intrinsically shunted Y-Ba-Cu-O (YBCO) JJ's have been demonstrated recently.[5]

Integrating SFQ-logic-based processors into ultrafast (e.g., above 30-GHz clock rate), high-performance applications requires, however, a new paradigm for digital input/output (I/O) communication between the SFQ processor and the outside world. Only optical fiber links can assure multi-GHz bit rates; they are also immune from crosstalk and electromagnetic interference and feature excellent thermal insulation. Together, a SFQ processor and an optical I/O will constitute the new ultrafast optoelectronics, namely superconducting optoelectronics.

This article begins with a general description of a superconducting optoelectronic router followed by, in separate sections, descriptions of progress in the development of optical-to-electrical transducers (OET's) and electrical-to-optical transducers (EOT's), suitable as I/O circuitry for superconducting digital electronics. Finally, a brief summary includes a personal assessment of the current state of the art in the superconducting optoelectronic (I/O) interface.

Superconducting Optoelectronic Router

One of the application areas where superconducting electronics can significantly outperform semiconductor technologies is telecommunication hardware, namely, ultrafast routers and crossbar-type switching structures.[4] The router is being used in telecommunication systems as the network node that directs the flow of information between different sub-networks. Figure 88.22 shows a schematic of an optoelectronic router.[6] Information arrives as multiwavelength trains of optical pulses at the router input ports, where, using suitable OET's, it is translated into the electrical domain. Next, information packages are routed to the appropriate output addresses using an ultrafast electronic processing network that provides such packet-switch functions as routing and drop/add, without the need to demultiplex down to lower data rates. Finally, signals are translated again, but this time into the optical domain, using EOT's.

In the superconducting router, the switching circuitry of the electronic information processor is based on the SFQ gates because of their very high switching speed and design simplicity. Present-day SFQ crossbar designs are limited to switching speeds below 10 GHz and utilize copper I/O microwave

transmission lines.[7] These lines are known to be too dispersive and lossy at frequencies exceeding 30 GHz. They also consume too much cooling power because they constitute a cryogenic-to-room-temperature interface that accounts for up to 75% of the total load. In future-generation, 100-GHz-bandwidth routers, only optical fibers can provide the needed signal transmission bandwidth, as well as excellent thermal insulation. We note that in switching-type systems, contrary to most of the other digital data processing schemes, both the OET's and EOT's have to provide a bandwidth that is at least equal to the operating frequency of the information-processing unit. Thus, the clock rate of the entire router circuit is limited by the digital processor and *not* the I/O circuitry.

In the example in Fig. 88.22, optically coded information has the form of return-to-zero (RZ) pulses. Logical "1's" in subsequent clock cycles are coded as separate pulses, while the absence of a pulse in a given clock cycle is interpreted as logical "0." The RZ coding is optimal for laser pulses and fits naturally to the SFQ logic, which is also coded based on either presence or absence of a pulse in a clock cycle.[2] Thus, no additional matching circuitry is needed at the I/O ends. Finally, the OET's and EOT's should be optimized for a 1.55-μm-radiation range since this wavelength is the optical communication standard for data transmission.

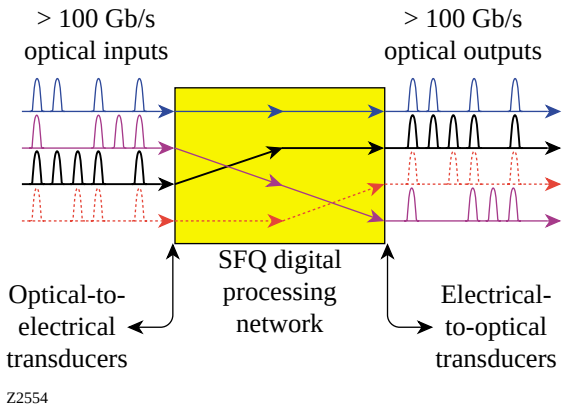

Figure 88.22
Schematic of the superconducting optoelectronics input and output interfaces for an ultrafast SFQ digital information processing network. Each train of optical pulses represents a different optical wavelength due to assumed implementation of the WDM technique.

Superconducting Optical-to-Electrical Transducers

The first superconducting optoelectronic circuit was demonstrated by Dykaar *et al.*[8,9] As shown in Fig. 88.23(a), a photoconductive metal-semiconductor-metal (MSM) diode (a 50-μm-wide gap in the coplanar line, on the left-hand side of the junction) was used as the OET, and the generated photoresponse signal was directly applied to switch a tunnel JJ. The structure was fabricated using the Pb-alloy technology[10] on a semi-insulating GaAs substrate, which acted as the active medium for the MSM switch. Since the JJ was not shunted, the circuit operated only with the unbiased junction and when the MSM-generated excitation current pulses (typically ~8 ps wide) exceeded the critical charge (time integral of the pulse) needed to switch a hysteretic JJ into the resistive state.[9] The circuit was tested using the early version of the cryogenic electro-optic (EO) sampling system,[11] with the 50-Ω probe transmission line fabricated on $LiTaO_3$ and wire-bonded directly to the superconducting coplanar line [Fig. 88.23(a)]. The JJ switching waveform was sampled about 300 μm from the junction [see "sampling point" in Fig. 88.23(a)]. The recorded transient is shown in Fig. 88.23(b).

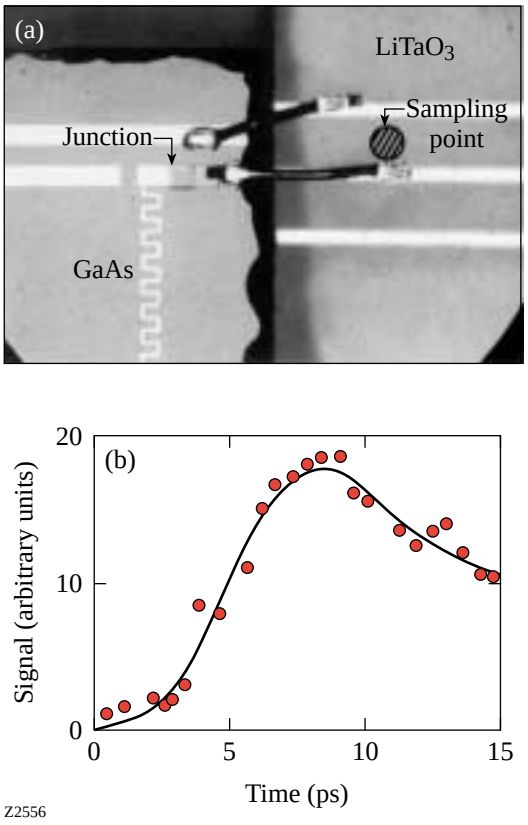

Figure 88.23
(a) Micrograph of an optoelectronic superconducting Pb-alloy circuit consisting of a GaAs photoconductive switch and separately biased Josephson junction (JJ). The circuit is wire-bonded to a transmission line on a $LaTiO_3$ crystal for EO sampling measurements. (b) Time-resolved switching process of the unbiased JJ shown in (a), driven by an 8-ps-wide electrical transient. The input amplitude was approximately five times the junction critical current. Temperature was 2.1 K.

It exhibits a ~3-ps turn-on delay time, followed by a ~5-ps rise time. The signal fall time is significantly longer, demonstrating that after switching, the junction remained in the transient voltage state, as expected from JSPICE-program numerical simulations.[9]

The usefulness of the structure shown in Fig. 88.23(a) for practical router structures was limited by the use of an unshunted JJ. The hysteretic nature of the junction current–voltage (*I–V*) characteristics precluded the use of the junction dc bias as an adjustable switching threshold. In addition, the junction exhibited a large resistive-capacitive (RC) time constant, limiting the transducer's speed of response. Later, Van Zeghbroeck[12] published systematic studies of *I–V* characteristics of various cryogenic MSM diodes and demonstrated that Nb-Si-Nb devices were compatible with Nb-based JJ circuits.

The next-generation superconducting OET system proposed and implemented by Wang *et al.*[13] was free of the limitations suffered by its predecessors. The test structures were fabricated at the HYPRES Foundry, using their standard Nb process,[14] and were fully compatible with the current SFQ digital circuit technology. This OET is shown in Fig. 88.24(a) and consists of a Nb-Si-Nb MSM photodiode, integrated with a two-JJ pulse shaper. This arrangement allowed trains of 100-fs-wide optical pulses from an external laser source, incident on the Nb-Si-Nb diode (switching beam), to be transformed into electrical signals and shaped into SFQ pulses by the two-junction Josephson pulse shaper (both JJ's were externally resistively shunted). The SFQ waveforms were recorded right after the second JJ (sampling beam), using the EO sampling system, and, as shown in Fig. 88.24(b), represented sub-mV, 3.2-ps-wide voltage transients. The integral of the experimental signal was equal to Φ_0, a quantum of magnetic flux, confirming that indeed the OET output consisted of single SFQ pulses. The measured pulse characteristics were in very good agreement with JSPICE simulations.[13] The simulations also showed that the width and amplitude of measured SFQ signals were limited by the parameters of the JJ's used in the pulse shaper and not the Nb-Si-Nb photodiode.

Wide possibilities for superconducting optoelectronic circuits[15] were opened as a result of the successful demonstration that the integrated OET system is indeed able to transform a train of optical pulses into the SFQ-coded input for a superconducting digital electronic circuit at rates of up to 30 Gbit/s for 1.5-μm-feature-size JJ technology (HYPRES standard process[14]). Currie, Sobolewski, and Hsiang[16] used Nb-Si-Nb photodiodes to inject approximately 20-ps-wide electrical pulses into Nb-based superconducting transmission lines to study their propagation properties. They also determined the amount of crosstalk between two Nb microstrips, fabricated at different metallization levels and separated by a dielectric SiO_2 layer (see Fig. 88.25). The time-resolved crosstalk signal was measured using the EO sampler and was >20 dB below the signal propagated in the main transmission line (see "sampling points" in Fig. 88.25). The results were in very good agreement with the simple capacitive model of the signal coupling between the two crossing microstrips. Bulzacchelli *et al.*[17] implemented MSM diodes for an optoelectronic clocking system in which optical pulses were delivered via fiber to a superconducting chip, on which the Nb-Si-Nb OET triggered the SFQ

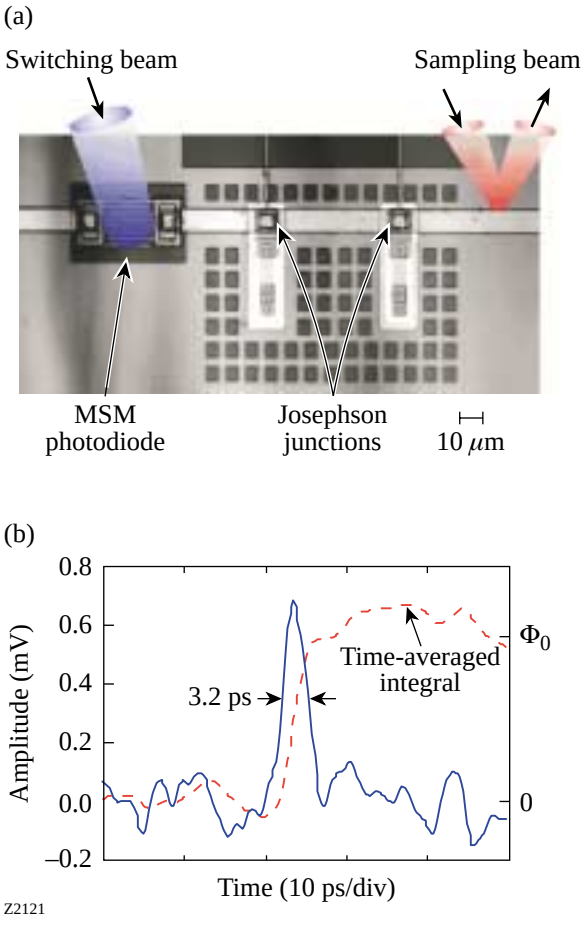

Figure 88.24
(a) Micrograph of an optoelectronic superconducting Nb circuit consisting of a Nb-Si-Nb MSM photodiode coupled to a microstrip line and followed by a two-junction pulse shaper. The entire circuit was overlayed with a $LaTiO_3$ crystal for EO sampling measurements (not shown). (b) Time-resolved single SFQ pulse and its time integral. Temperature was 2.1 K.

circuit at frequencies reaching 20.6 GHz. As in the work by Wang *et al.*,[13] all of these electronic structures were fabricated in the standard, Nb-trilayer HYPRES process.[14]

The discovery of HTS materials offered the promise that HTS digital electronics can reach terahertz clock speeds.[3,4] The characteristic response times of HTS are of the order of single picoseconds[18] and intrinsically shunted YBCO JJ's exhibit a characteristic voltage close to 8 mV,[19] predicting that the corresponding SFQ pulse width, generated during the junction switching event, should be well below 100 fs. To achieve comparable, subpicosecond electrical excitations, Osbahr *et al.*[20] used amorphous GaAs, deposited directly on a coplanar YBCO transmission line. The structure acted as a MSM diode, and the authors successfully generated the shortest 0.4-ps-wide electrical input pulses reported to date (~2-THz digital bandwidth). The pulses were used to study propagation properties of YBCO transmission structures. It is interesting that GaAs did not "poison" the YBCO; however, an overlay of Au on the YBCO strips was needed to sustain the highest, THz-frequency components in the propagating pulses. This latter result confirmed the earlier studies[21] that at above 300 GHz, microwave loss of superconducting YBCO actually exceeds that of normal metals, such as Au or Cu, kept at 77 K.

Independently of semiconducting MSM-type devices, both LTS[22,23] and HTS[18] microbridges, operated as hot-electron photodetectors, have been proposed as OET's. For LTS photodetectors, NbN was the material of choice since it is characterized by a ~30-ps photoresponse time,[24] the fastest among conventional superconductors. In the case of HTS structures, the YBCO microbridge was successfully implemented as an optoelectronic interface for switching a grain-boundary YBCO junction.[5] Figure 88.26(a) presents an integrated YBCO microbridge plus a YBCO–JJ structure. The bridge was independently biased (not shown) and, upon illumination with a femtosecond optical pulse (excitation beam), generated ~2-ps-wide electrical transients, which were then applied to switch the dc-biased JJ. Time-resolved dynamics of the junction were studied with the help of the EO sampling system (sampling beam). The actual test geometry, shown in Fig. 88.26(a), was characterized by a large inductance parallel to the JJ, due to the extended, right-angle-type junction leads. Nevertheless, the authors were able to extract the actual junction switching process and demonstrate [see Fig. 88.26(b)] that the response consisted of a train of 0.65-ps-wide SFQ pulses. The measured signal was in very good agreement with JSPICE simulations performed for a shunted JJ with the characteristic voltage of 2.1 mV. The JJ's estimated power consumption associated with the SFQ pulse generation was ~0.1 μW, leading to a "switching time" × "dissipation power" product equal to 0.08 aJ, the lowest reported value for any digital device. Further JSPICE simulations[25] predicted that YBCO JJ's with the characteristic voltage above 3.5 mV (well within the reach of the current HTS JJ technology[19]) should generate SFQ pulses with a width of <300 fs, which corresponds to a 3-dB bandwidth of >1 THz, breaking yet another "barrier" in the development of digital technologies.

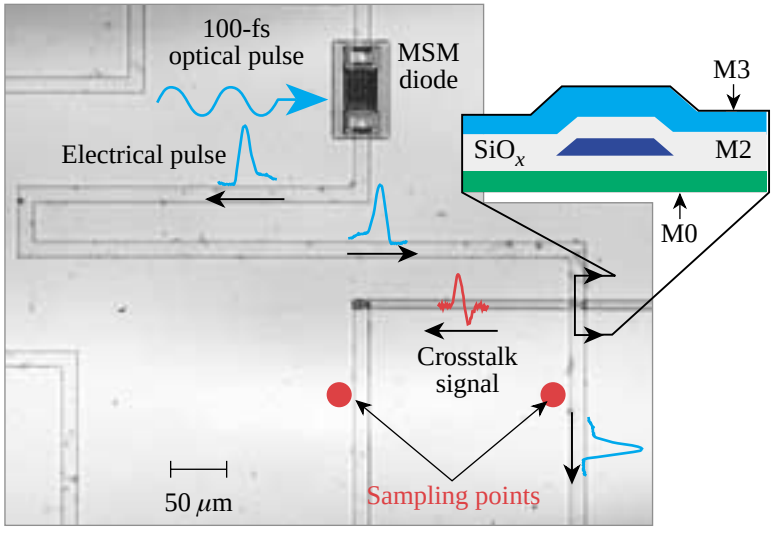

Z2312

Figure 88.25
Micrograph of an experimental setup for measuring crosstalk. The circuit uses an MSM diode to generate a picosecond electrical transient, which propagates along the main microstrip line (MSL) and then crosses above the other. At the intersection each line is on a different metallization layer. The signals on the two MSL's are detected at sampling points by the EO system.

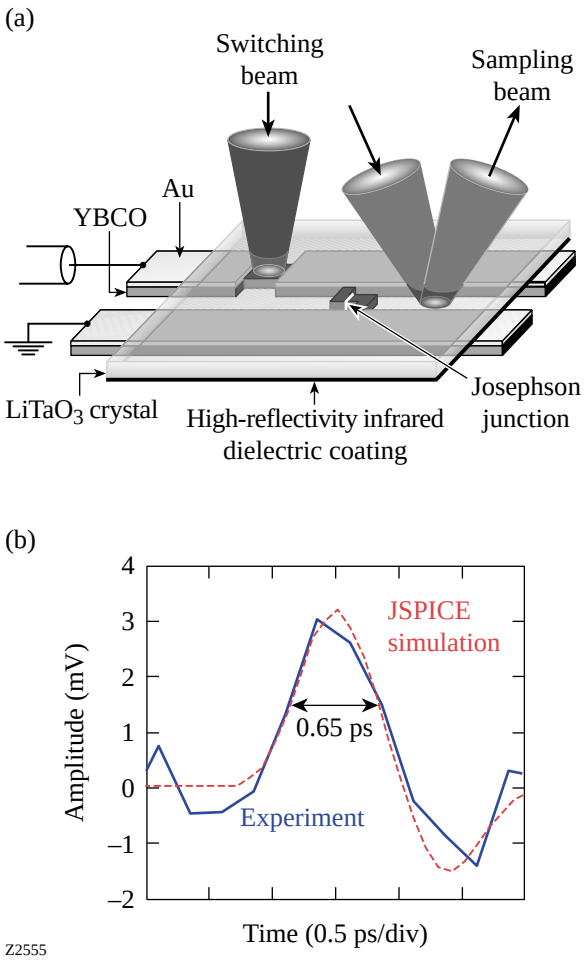

Figure 88.26
(a) Schematic of a coplanar strip transmission line containing a YBCO microbridge and a bicrystal JJ. The entire circuit is overlayed with a $LaTiO_3$ crystal for EO sampling measurements. (b) Time-resolved, single SFQ pulse and the corresponding numerical JSPICE simulation. Temperature was 20 K.

Superconducting Electrical-to-Optical Transducers

Both the OET and EOT ends of the telecommunication router must, of course, operate at the same speed. In the case of the superconducting crossbar, in the best scenario, the EOT should be able to transform a sequence of "0" and "1" SFQ pulses directly into optically coded information. The design of the SFQ-to-optical output interface is a very challenging problem, mainly due to the extremely low energy being carried by SFQ pulses, and, so far, there are no satisfactory practical solutions. Several new concepts, however, designed specifically for digital superconducting electronics, have recently been proposed.

The first optical output interface for JJ electronics was proposed by Van Zeghbroeck[12] in the form of an actively modulated GaAs/AlGaAs semiconductor laser diode with a sub-mA threshold current. The GaAs/AlGaAs laser diodes were selected because of their low power dissipation and large modulation bandwidth. The first actual implementation of the laser-diode EOT system in a JJ latching integrated circuit was achieved by Nakahara *et al.*[23] The authors used the special high-voltage Josephson circuit to increase the signal level to about 10 mV and then amplified it using a liquid-helium HEMT (high-electron-mobility transistor) semiconducting amplifier. Subsequently, the output was fed into a liquid-He InGaAsP laser. Although only low-frequency tests were performed, the expected maximum speed of the output circuitry was estimated to be approximately 1 GHz.

A laser diode operating at 4.2 K was also used by the HYPRES team[26,27] to provide a serial output data stream via an optical fiber from a superconducting analog-to-digital converter (ADC) to room-temperature conventional electronics. The output from the ADC was linearized with a parallel-to-serial converter, amplified with an on-chip driver (Josephson amplifier), and used to modulate a laser diode biased at the lasing threshold. The authors also investigated in detail the performance of various laser diodes fabricated for operation at 4.2 K.[27] They found that, at low temperatures, the current threshold for lasing reduces significantly, resulting in much lower input power being needed to operate the laser. Unfortunately, the dynamic resistance (dV/dI) also increases significantly near the lasing threshold and the power efficiency (dP_{out}/dI) decreases. To successfully operate a laser as a superconducting EOT, its dynamic resistance should be as small as possible, so that an appreciable current modulation is produced when a small voltage signal is applied. At the same time, dP_{out}/dI should be as large as possible, to get a large modulation of the optical power output. The analysis presented in Ref. 27 indicated that $dV/dI < 10\ \Omega$ and $dP_{out}/dI \geq 0.5$ mW/mA are required for robust operation of a laser-based optical output interface for superconducting electronics. More research on cryogenic laser diodes is needed to achieve these parameters.

Recently, Sobolewski and Park[28] proposed a magneto-optic (MO) modulator as an ultrafast EOT. The main advantage of a passive modulation scheme is that it requires only a sensitive medium and optimized coupling between electrical and optical signals to obtain the desired modulation efficiency and speed of response. For cryogenic systems, it is very important that

fiber-coupled modulators represent only a minor thermal load. While the MO effect has been applied to optical modulators[29] in current, conventional optoelectronic systems, ultrafast EO modulators are used exclusively as EOT's. Unfortunately, the EO modulators are not practical for superconducting electronics since they require high-voltage driving signals and, thus, are incompatible with SFQ gates.

MO modulators based on the Faraday effect offer a number of advantages for superconducting optoelectronics. Many MO materials, including the most-sensitive europium monochalcogenides, exhibit MO properties only at temperatures below 20 K,[30] while the Verdet constant for diluted-magnetic semiconductors, or garnets, increases drastically at low temperatures. In addition, some MO crystals (e.g., EuS and EuSe) are characterized by <2-ps response times, assuring above-150-GHz, 3-dB analog bandwidth.[31] In garnets, the response is limited by the ferromagnetic resonance frequency (e.g., 82.3 GHz for Bi-YIG[32]) with potential for reaching >1 THz.

Figure 88.27 shows the concept of a superconducting MO modulator based on a microwave microstrip line (MSL) with a polarization-sensitive MO active medium and fiber-optic cw light delivery [Fig. 88.27(a)]. The MSL configuration, with the superconducting ground plane, allows for a long interaction distance, and the low characteristic impedance of the line assures that the *H*-field component of the electromagnetic signal is uniform along the modulator length [Fig. 88.27(b)]. Light modulation direction occurs in parallel to the *H* field and perpendicular to the signal propagation. Unlike most common EO modulators, this eliminates the need to match the velocities of the electromagnetic signal and light, unless a multipass design is considered. Numerical simulations showed that for the 100-μm-wide, 5-μm-high MSL, filled with the EuSe MO material and assuming that the input current pulse is 1 mA (10-kA/cm^2 critical current density for a nominal 10-μm^2 Josephson tunnel junction), the *H* uniformity along the optical pass is >98% and the angle of Faraday rotation for green light reaches ~0.13°. In a crossed-polarizers modulator geometry, such a polarization rotation angle should give a signal-to-noise ratio of above 10 in the 160-GHz bandwidth of Ref. 33.

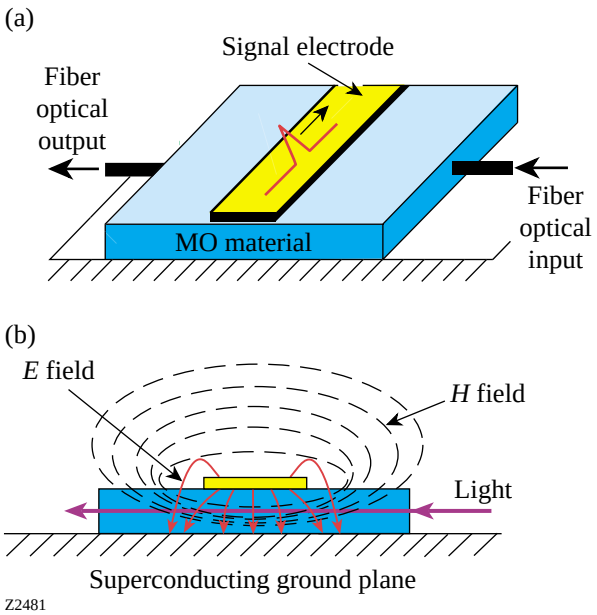

Figure 88.27
Structure of a superconducting MO modulator proposed in Ref. 28. (a) Modulator geometry. (b) Cross section schematically showing spatial distribution of the *E* and *H* fields.

Conclusion

Various concepts for ultrafast I/O interfaces for digital superconducting electronics suitable for telecommunication routers have been reviewed. For the input OET, it has been demonstrated experimentally that both the amorphous GaAs photoconductive switch and the YBCO hot-electron photodetector are able to transform the >100-Gbit/s optically coded input information to the electrical domain with sufficient signal-to-noise ratio, speed, and power loading. The Nb-Si-Nb diode is also a desired solution, primarily because of the ease of integration with the standard Nb JJ fabrication process. The Nb MSM's, however, should be patterned with deeply submicron dimensions to reach the single-picosecond response times needed for the ultrafast router applications. From the bias point of view, MSM-type structures have a significant advantage over hot-electron photodetectors since they are highly resistive in the OFF state and do not load the circuit. On the other hand, the responsivity of superconducting photodetectors is significantly higher. Most recently, NbN photodetectors have been demonstrated to respond to single visible and infrared photons,[34] making them the leading candidate for future quantum communication and quantum cryptography systems.

Optoelectronic output from the superconducting electronics and, especially, the direct SFQ-to-optical transition is very difficult since SFQ pulses carry very little energy. There is no proven concept that achieves both the needed >100-Gbit/s speed and the required sensitivity. The active laser-diode modulation scheme allows for direct modulation of the optical

output at the processor clock frequency; however, for SFQ electronics, it requires substantial, broadband amplification of SFQ pulses or high-voltage latching Josephson output drivers to drive the laser. In addition, the laser itself, placed inside the dewar, is a significant source of thermal loading. Laser modulation can be a viable option in systems where the output signal has relatively low clock frequency (e.g., in digital decimation filters) since the current EOT designs are limited to speeds of approximately 1 GHz. Extensive research is needed to develop a semiconductor laser diode optimized for ultrafast performance at cryogenic temperatures.

Passive modulation schemes seem to be the approach of choice since, in the modulator case, one needs to achieve only an "imprint" of the SFQ-coded information onto the optical beam to carry it into room temperature and, subsequently, process it using conventional optoelectronics. Passive modulation, based on EO modulators, is the current optoelectronic industry standard. Among optical modulators for superconducting SFQ electronics, MO devices are favored by the author since, at least based on the literature and ultrafast sampling measurements conducted by Freedman,[31,32] they seem to be fast and sensitive enough, and their performance is actually improved at cryogenic temperatures. The first comprehensive demonstration, however, is yet to be performed.

ACKNOWLEDGMENT

This work was supported by the US Office of Naval Research Grant N00014-00-1-0237.

REFERENCES

1. P. Lagasse *et al.*, *Photonic Technologies in Europe* (Telenor AS, R&D, Norway, 1998), http://www.infowin.org/ACTS/ANALYSYS/PRODUCTS/THEMATIC/PHOTONIC/.
2. K. K. Likharev and V. K. Semenov, IEEE Trans. Appl. Supercond. **1**, 3 (1991).
3. K. Likharev, Phys. World **10**, 39 (1997).
4. P. Bunyk, K. Likharev, and D. Zinoviev, Int. J. High Speed Electron. Syst. **11**, 257 (2001).
5. R. Adam, M. Currie, C. Williams, R. Sobolewski, O. Harnack, and M. Darula, Appl. Phys. Lett. **76**, 469 (2000).
6. J. X. Przybysz, Northrup Grumman, private communication (1995).
7. Q. Ke *et al.*, IEEE Trans. Appl. Supercond. **7**, 2968 (1997).
8. D. R. Dykaar, R. Sobolewski, T. Y. Hsiang, and G. A. Mourou, IEEE Trans. Magn. **MAG-23**, 767 (1987).
9. D. R. Dykaar, R. Sobolewski, and T. Y. Hsiang, IEEE Trans. Magn. **25**, 1392 (1989).
10. See, e.g., W. Anacker, IBM J. Res. Dev. **24**, 107 (1980).
11. D. R. Dykaar, R. Sobolewski, J. M. Chwalek, T. Y. Hsiang, and G. A. Mourou, in *Advances in Cryogenic Engineering*, edited by R. W. Fast (Plenum Press, New York, 1988), Vol. 33, pp. 1097–1104; see also M. Lindgren, M. Currie, C. A. Williams, T. Y. Hsiang, P. M. Fauchet, R. Sobolewski, S. H. Moffat, R. A. Hughes, J. S. Preston, and F. A. Hegmann, IEEE J. Sel. Top. Quantum Electron. **2**, 668 (1996).
12. B. Van Zeghbroeck, IEEE Trans. Appl. Supercond. **3**, 2881 (1993).
13. C.-C. Wang, M. Currie, D. Jacobs-Perkins, M. J. Feldman, R. Sobolewski, and T. Y. Hsiang, Appl. Phys. Lett. **66**, 3325 (1995).
14. *HYPRES Process Design Rules Manual*, HYPRES, Inc., Elmsford, NY 10523.
15. C.-C. Wang, M. Currie, D. Jacobs-Perkins, R. Sobolewski, T. Y. Hsiang, and M. J. Feldman, in *Applied Superconductivity 1995*, edited by D. Dew-Hughes, Proceedings of EUCAS 1995 (Institute of Physics, Bristol, UK, 1995), Vol. 2, pp. 787–791.
16. M. Currie, R. Sobolewski, and T. Y. Hsiang, Appl. Phys. Lett. **73**, 1910 (1998).
17. J. F. Bulzacchelli *et al.*, IEEE Trans. Appl. Supercond. **7**, 3301 (1997).
18. M. Lindgren, M. Currie, C. Williams, T. Y. Hsiang, P. M. Fauchet, R. Sobolewski, S. H. Moffat, R. A. Hughes, J. S. Preston, and F. A. Hegmann, Appl. Phys. Lett. **74**, 853 (1999).
19. M. A. J. Verhoeven *et al.*, Appl. Phys. Lett. **69**, 848 (1996).
20. C. J. Osbahr *et al.*, Appl. Phys. Lett. **74**, 1892 (1999).
21. M. C. Nuss *et al.*, IEEE Electron Device Lett. **11**, 200 (1990).
22. M. Zorin *et al.*, IEEE Trans. Appl. Supercond. **7**, 3734 (1997).
23. K. Nakahara *et al.*, IEEE Trans. Appl. Supercond. **4**, 223 (1994).
24. K. S. Il'in, I. I. Milostnaya, A. A. Verevkin, G. N. Gol'tsman, E. M. Gershenzon, and R. Sobolewski, Appl. Phys. Lett. **73**, 3938 (1998).
25. R. Adam, R. Sobolewski, and M. Darula, in *Superconducting and Related Oxides: Physics and Nanoengineering IV*, edited by D. Pavuna and I. Bozovic (SPIE, Bellingham, WA, 2000), Vol. 4058, pp. 230–244.

26. L. A. Bunz, R. Robertazzi, and S. Rylov, IEEE Trans. Appl. Supercond. **7**, 2972 (1997).

27. D. Gupta, D. V. Gaiarenko, and S. V. Rylov, IEEE Trans. Appl. Supercond. **9**, 3030 (1999).

28. R. Sobolewski and J.-R. Park, IEEE Trans. Appl. Supercond. **11**, 727 (2001).

29. P. K. Tien and R. J. Martin, Appl. Phys. Lett. **21**, 394 (1972).

30. M. P. Mulloy, W. J. Blau, and J. G. Lunney, J. Appl. Phys. **73**, 4104 (1993).

31. M. R. Freeman, J. Appl. Phys. **75**, 6194 (1994).

32. A. Y. Elezzabi and M. R. Freeman, Appl. Phys. Lett. **68**, 3546 (1996).

33. R. Rey-de-Castro and W. Glomb, LLE, private communication (2001).

34. G. N. Gol'tsman, O. Okunev, G. Chulkova, A. Lipatov, A. Semenov, K. Smirnov, B. Voronov, A. Dzardanov, C. Williams, and R. Sobolewski, Appl. Phys. Lett. **79**, 705 (2001).

Optimizing the Fabrication of Polyimide Shells

Introduction

Polyimide is being developed as an ablator material for inertial confinement fusion (ICF) targets because of its superior mechanical and thermal properties.[1] A typical target design for the OMEGA laser system consists of a spherical shell, 1 mm in diameter and 1 μm in wall thickness, with a 100-μm-thick layer of solid deuterium and tritium (DT) uniformly deposited on the inner surface. To achieve this, the shells must be both strong and permeable so that they can be filled quickly with DT gas and survive the pressure gradient created in subsequent treatments, including cooling to below 18.9 K and layering by differential heating. Material properties that determine the performance of shells as targets include gas permeability, Young's modulus, tensile strength, and elongation at break.[2]

Fabrication of spherical polyimide shells has been demonstrated using a vapor deposition polymerization (VDP) method, and preliminary characterization of the shell properties has been conducted.[2–4] In this work, a parametric study was performed on the fabrication process of polyimide shells. The production rate, yield, and reproducibility of the process were optimized. The shells were thoroughly characterized to determine the material properties, microstructures, and surface finish, which were then correlated with the processing parameters. The permeability was also determined at cryogenic temperatures between 130 K and 295 K.

Experimental

1. Fabrication

a. Materials. 1,2,4,5-benzenetetracarboxylic dianhydride (PMDA) (97% purity) and 4,4′-oxydianiline (ODA) (99+% purity; zone refined) were purchased from Aldrich Chemical and used as received. Spherical shells, ~910 μm in diameter with a 7- to 17-μm wall thickness and >99.8% sphericity, made of thermally depolymerizable poly-α-methylstyrene (PAMS) with a molecular weight (MW) of 400,000 were received from General Atomics and used as mandrels without further treatment.

b. Deposition. The fabrication process involved two steps. PMDA and ODA were vapor deposited to form poly(amic acid) (PAA) on either PAMS mandrels or flat substrates. The PAA layer was then converted into polyimide by thermal imidization. In this process, the PAMS mandrels depolymerized and permeated out of the nascent polyimide layer, resulting in freestanding shells. The chemical reaction scheme is shown in Fig. 88.28.

A schematic of the deposition system is shown in Fig. 88.29. The two monomers were separately sublimed from two evaporators directed toward a rotating coating stage.[3] The vacuum chamber was maintained at 4.8 to 5.2 $\times 10^{-6}$ Torr throughout deposition. The individual deposition rates of PMDA and ODA

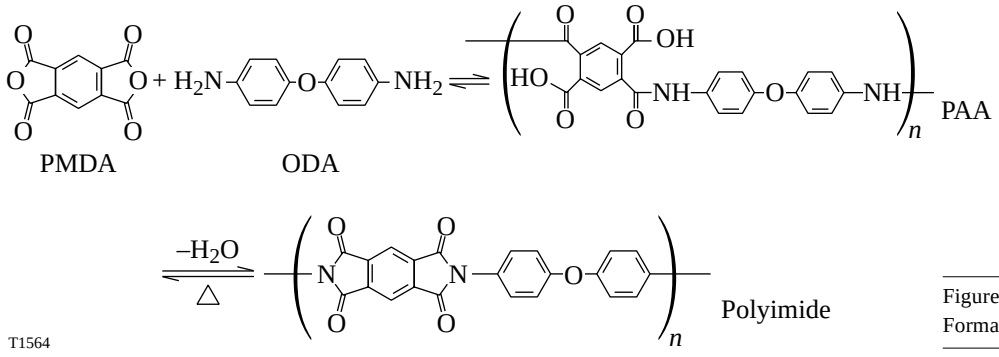

T1564

Figure 88.28
Formation of polyimide from PMDA and ODA.

were measured by depositing each of them separately onto 0.3-cm^2 PAMS films, which were weighed, before and after deposition, to an accuracy of ±0.05 μg using a microbalance (Cahn model 4700). The monomer deposition rates were measured for discrete evaporator temperatures and substrate positions to determine the conditions that yielded equimolar deposition of the monomers. A 3×5-cm^2 shutter plate was used to shield the substrate for approximately 30 min until the steady-state deposition rates were reached.

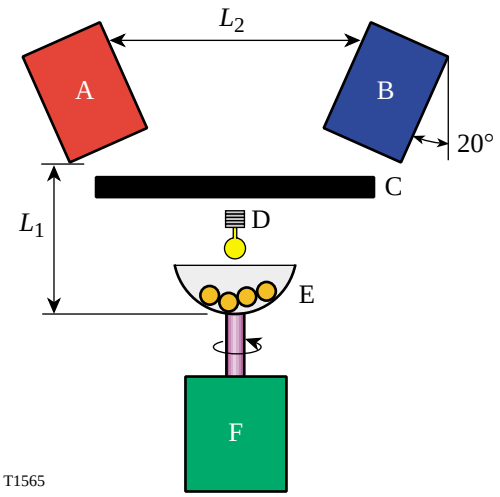

Figure 88.29
Schematic of the deposition system inside the vacuum chamber. A: evaporator for ODA; B: evaporator for PMDA; C: shutter; D: tungsten lamp filament; E: rotating pan with shells; F: motor. Dimensions: L_1 = 3 cm; L_2 = 5 cm.

Batches of 20 to 60 PAMS mandrels were over-coated in a 1-cm-diam hemispherical aluminum holder rotating at 60 to 120 rpm.[5] The static charge created by the motion of the mandrels was neutralized by flooding the entire holder with electrons from a biased tungsten filament (12 V; 20 mA) 0.5 cm above the holder. To examine the effect of a heated substrate, the temperature of the PAMS mandrels was raised from room temperature to 140°C. This was achieved by clamping the shaft of the rotating pan between two copper fingers that were connected to a cartridge heater. The temperature was controlled with an OMEGA CN9001 temperature controller. The pan was preheated at 140°C for 2 to 3 h before deposition began.

Flat films were deposited on either silicon wafers (1 × 1 cm^2) or sodium chloride disks (1.3-cm diameter and 0.1-cm thickness; purchased from International Crystal Laboratory), which were also rotated at 60 to 120 rpm. The deposition rate was ~7 μm/h for flat films and ~3 μm/h for shells at room temperature.

c. Imidization. The as-deposited PAA shells were imidized in a NEY Centurion VPM vacuum furnace with programmable temperature (accuracy = ±0.1°C). The furnace was purged by a constant 7.5-cm^3/min flow of nitrogen or air throughout the imidization process. The temperature cycle consisted of a ramp-up (0.1, 0.5, or 1°C/min) from 25 to 300°C, a soak at 300°C for a predetermined duration (1, 3, or 6 h), and cooldown to 25°C at 5°C/min. Images of the shells during imidization were recorded and analyzed to monitor the changes in shell diameter with temperature. Imidized flat films were detached from the substrates by soaking in de-ionized water at 90°C for 24 to 48 h. The films were then dried at 80°C under vacuum for 24 h.

2. Characterization

a. Chemical analysis. Fourier transform infrared (FTIR) spectra were obtained using films approximately 1 μm thick deposited on sodium chloride disks. The elemental composition was determined by combustion analysis performed by Oneida Research Services using freestanding films with mass of approximately 10 mg. Solubility was examined by soaking films and shells in concentrated sulfuric acid (97%) at room temperature. The size of the samples was monitored using an optical microscope throughout soaking.

b. X-ray diffraction (XRD). The tested samples included (1) freestanding films (1 cm × 1 cm × 25 μm), (2) shells, and (3) flat films made of 10 to 20 flattened shells. A Rigaku D2000 Bragg-Brentano diffractometer[6] equipped with a copper rotating anode, diffracted beam graphite monochromator, and scintillation detector was used to obtain reflection-mode diffraction patterns from film samples. Data were collected as continuous scans, at a scan rate of 2° 2θ/min. A Bruker AXS microdiffractometer[7] equipped with a copper rotating anode, Goebel mirrors, a 0.5-mm collimator, and a two-dimensional general area detector diffraction system (GADDS) was used to obtain transmission-mode diffraction patterns for shell and film samples and reflection-mode diffraction patterns for shell samples. Each data set was collected until 10^7-count total integrated intensity was achieved.

c. Dimensions and surface finish. Shell diameter was measured to an accuracy of ±1 μm using a Nikon Optiphot microscope, and the wall thickness was calculated from mass and density. The shell mass was measured to an accuracy of

±0.05 μg using a microbalance, and the density was measured to an accuracy of ±0.001 g/cm^3 using a density column (performed by General Atomics). The wall thickness obtained by this method was confirmed by SEM (scanning electron microscope) micrographs of the wall cross sections obtained on a LEO 982 Field Emission SEM. The thickness of flat films was measured using a Rank Taylor Hobson Talysurf profilometer to an accuracy of 0.1 μm.

The shell's surface finish was characterized by sphere-mapping (performed by General Atomics) and by using a SEM. Sphere maps were measured for thin-walled (1.5- to 1.8-μm) shells that were slightly inflated (~1%) by 4- to 6.5-atm internal pressure of nitrogen. The permeability of nitrogen through the shell wall was sufficiently low to maintain the inflation for ~24 h. The same shells were measured again when deflated to compare the surface finish with or without inflation.

d. Property measurements. One hundred to two hundred shells prepared under each imidization condition were measured for gas permeability and mechanical properties. The permeability was determined by measuring the time constant. Young's modulus, tensile strength, and elongation at break were determined by a burst/buckle test. Detailed descriptions of the test procedures can be found elsewhere.[3,8] Helium permeability at cryogenic temperatures (156 K to 298 K) was determined for Kapton HN and vapor-deposited flat films (dimension = 1 cm × 1 cm × 25 μm) using a setup reported elsewhere,[3] with the addition of a helium leak detector (Edwards Spectron 600D) to measure the helium permeation rates through the films.[9]

Results and Discussion

1. Yield and Reproducibility of the Fabrication Process

a. Deposition. Maintaining the stoichiometric ratio (1:1) of monomers when depositing PAA is critical since non-stoichiometric deposition results in greatly deteriorated properties and surface finish.[10–13] The monomers must also be uniformly deposited over the entire substrate surface. The spatial variation of the monomer deposition rates on the substrate plane is shown in Fig. 88.30 (note that the X-Z plane is the plane of symmetry for the two evaporators). The dependency of the monomer deposition rates on the evaporator temperature is shown in Fig. 88.31. The evaporator temperatures that yielded equimolar monomer deposition were PMDA = 153°C and ODA = 126°C. The substrate located at the center of the chamber floor [(0,0,0) in Fig. 88.30] was minimized in size (1×1 cm^2 for flat films; ~0.5×0.5 cm^2 for shells) and rotated at 120 rpm to reduce the spatial variability. Figure 88.32 illustrates the smooth surface of a typical shell deposited under the above conditions.

b. Imidization. The key factor that determines the yield of polyimide shells is the stress generated during imidization, which can rupture the shells if not carefully controlled. The main source of stress is the depolymerization of the PAMS mandrels into gaseous products at elevated temperatures. Depending on the depolymerization rate, the products may be unable to permeate out of the polyimide layer at the rate they are produced, creating a pressure differential that inflates the shells.

The changes in shell diameter during imidization under various heating rates and atmospheres are shown in Fig. 88.33. The shells imidized in air inflated more abruptly and at a lower

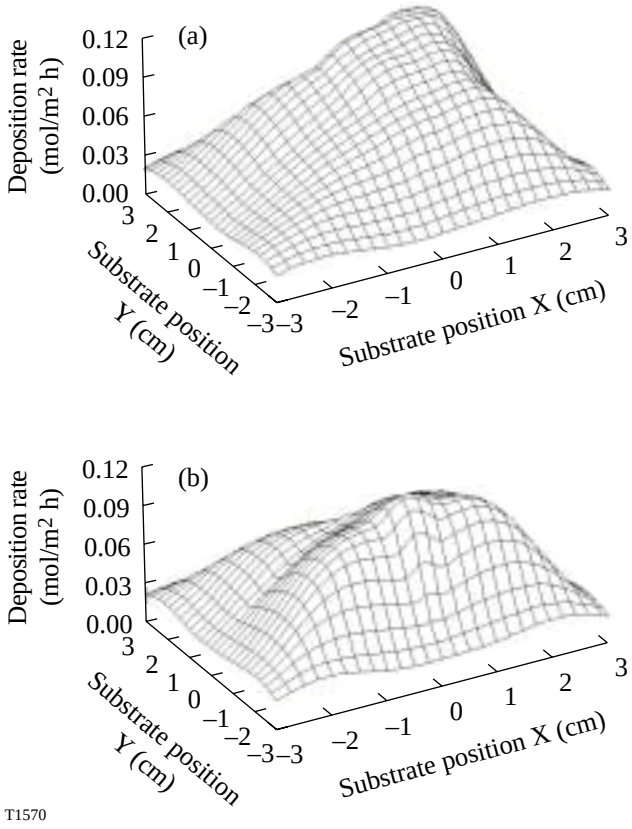

Figure 88.30
Spatial variation of the monomer deposition rates on the substrate plane: (a) PMDA (153°C), (b) ODA (126°C). Note that the X-Z plane is the plane of symmetry for the two evaporators. The separation between the evaporators is 5 cm, and the vertical distance between the substrate and evaporator planes is 3 cm, as shown in Fig. 88.29.

temperature than those imidized in nitrogen. This was attributed to the lower initiation temperature and higher reaction rate of the depolymerization of PAMS in the presence of oxygen. The yield of air-imidized shells was reduced as a result of this drastic inflation, as summarized in Table 88.II. In a nitrogen atmosphere, shells inflated more at higher heating rates due to the more rapid depolymerization of PAMS (Fig. 88.33), and the yield was lowered (Table 88.II). Imidizing at 0.1°C/min in a nitrogen atmosphere minimized the inflation and thus provided the highest yield.

The chemical composition of the polyimide shells and films produced by the optimized process agreed with that of the commercial PMDA-ODA films (Kapton®), as shown in the FTIR spectra (Fig. 88.34) and the combustion analysis data (Table 88.III).

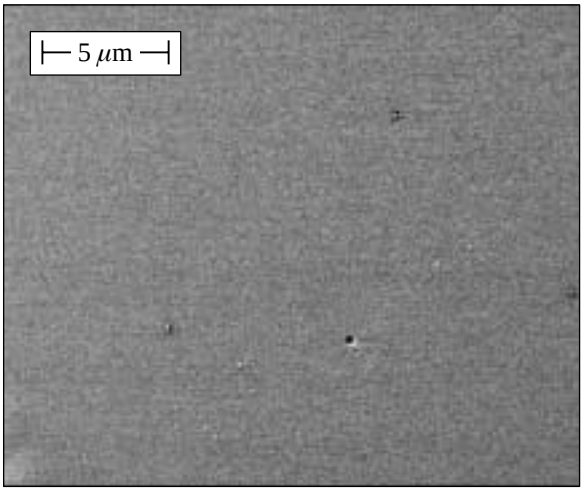

Figure 88.32
SEM micrograph of the outer surface of a 4-μm-thick polyimide shell.

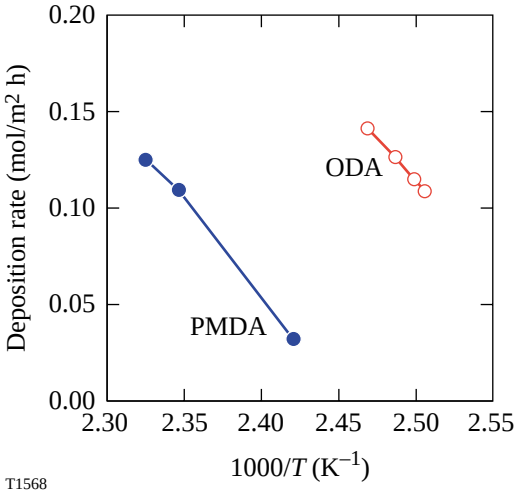

Figure 88.31
Dependency of the monomer deposition rates on the evaporator temperature. The deposition rates were measured with 0.3×0.3-cm^2 PAMS films located at (0,0,0) of Fig. 88.30.

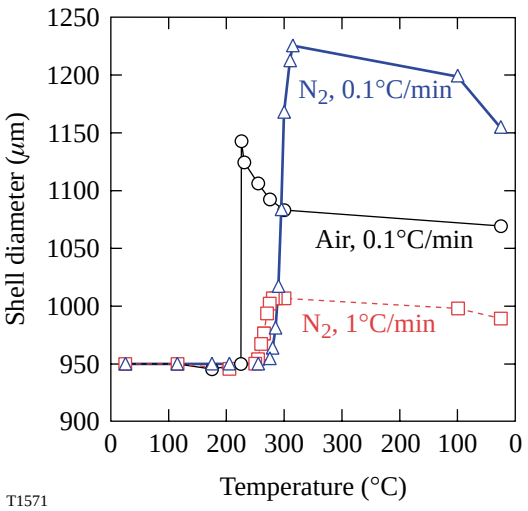

Figure 88.33
Changing shell diameter with imidization temperature for three imidization conditions: (a) N_2, 0.1°C/min, (b) air, 0.1°C/min, and (c) N_2, 1°C/min. The shells remained spherical throughout imidization.

Table 88.II: Yield of polyimide shells under different imidization conditions.

	Air 0.1°C/min	N_2 0.1°C/min	N_2 0.5°C/min	N_2 1.0°C/min
Yield (%)	60	100	90	60

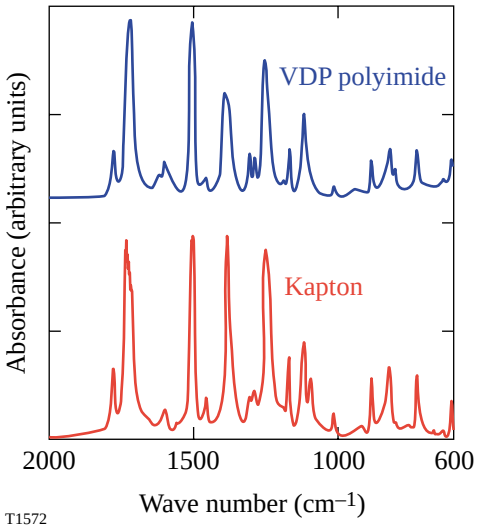

Figure 88.34
FTIR spectra of vapor-deposited polyimide (VDP) and Kapton®. The VDP sample was imidized at 0.1°C/min in N_2 for 6 h. The Kapton spectrum was obtained using a 8-μm-thick Kapton® HN film (DuPont).

Table 88.III: Atomic composition of VDP polyimide (imidized at 0.1°C/min in N_2; 6 h at 300°C) by combustion analysis. The formula of polyimide is $C_{22}H_{10}N_2O_5$.

	Atomic percent (%)			
	C	H	N	O
VDP (±0.2)	55.3	26.8	5.3	12.7
By formula	56.4	25.7	5.1	12.8

2. Properties of Polyimide Shells

The measured properties of polyimide shells agree with the literature values of commercial Kapton® films,[14] as shown in Table 88.IV. The experimental test matrix employed to obtain these properties used five to ten shells per batch; ten to twenty batches were tested to obtain batch-to-batch reproducibility. The narrow uncertainty intervals listed in Table 88.IV confirm the reproducibility of the process.

3. Effects of Imidization Conditions

Different imidization conditions resulted in different permeability, tensile strength, and flexibility (ultimate strain) but had little effect on the Young's modulus of the shells. The results can be summarized as follows:

a. Imidizing atmosphere (N_2 versus air). The properties of N_2- and air-imidized polyimides are compared in Table 88.V. Imidizing in air instead of nitrogen increased the permeability by ~100% while reducing the strength by ~25%. The elongation at break was also decreased by ~50%. The air-imidized shells possessed lower crystallinity than N_2-imidized shells, as indicated by the x-ray diffraction patterns in Fig. 88.35, where the peak associated with the 002 lattice planes is substantially weaker in the air-imidized samples.

The FTIR spectra in Fig. 88.36 show that the air-imidized samples retained a weak anhydride peak at 1850 cm^{-1}, indicating that a small fraction of the imide groups had been hydrolyzed into anhydride. This may result in a shortened polymer chain length that generally reduces the tensile strength and elongation at break of polymeric materials.[15] Both air- and N_2-imidized shells were cross-linked, as indicated by the fact that they were insoluble in concentrated sulfuric acid.[16] The distinct properties of the air-imidized samples may be attributed to their lower crystallinity and MW.

Table 88.IV: Properties of polyimide shells (imidized at 0.1°C/min in N_2; 6 h at 300°C) and the literature values for Kapton®. E = Young's modulus, σ = tensile strength, and ε = elongation at break.

	Mechanical Properties			Gas Permeability (mol·m/m^2·Pa·s)			
	E (GPa)	σ (MPa)	ε	He × 10^{16}	H_2 × 10^{16}	D_2 × 10^{16}	N_2 × 10^{18}
VDP shells	3.2±0.1	280±19	0.27±0.02	4.9±0.1	3.6±0.1	3.5±0.1	3.9±0.2
Kapton®[13]	2.5	231		8.2	4.9	4.4±0.1*	12

*Measured experimentally with 25-μm-thick Kapton® HN films (DuPont).
(Literature value of D_2 permeability through Kapton is unavailable.)

b. Imidizing rate. The properties of polyimide imidized at different heating rates are shown in Table 88.VI. Helium permeability increased with the heating rate, while the tensile strength and flexibility showed an opposite trend. The samples imidized at 1°C/min became soluble, suggesting that the fast heating rate had eliminated cross-linking. The higher permeability and lower tensile properties of the shells imidized at 1°C/min may be attributed to the absence of cross-linking.[17–19]

The XRD patterns of shells imidized at 1°C/min and 0.1°C/min are compared in Fig. 88.37. The relative intensity of the 002 peak showed that the crytallinity was lower in the 1°C/min sample than in the 0.1°C/min sample. This provides another explanation for the differences in the properties. The greater strain/stress experienced by the shells imidized at 1°C/min, as shown in Fig. 88.33, is believed to hinder the polyimide molecules from crystallizing.

c. Imidization time at 300°C. As shown in Table 88.VII, the helium permeability, tensile strength, and flexibility increased with the duration for which the samples were cured at 300°C. The samples imidized for 1 h dissolved completely in sulfuric acid, while the samples imidized for more than 3 h were insoluble. As displayed in the FTIR spectra (Fig. 88.38), the intensity of the imide peaks (~1780 and 1380 cm^{-1}) increased with the cure time (no further effect was observed after 6 h at 300°C). The FTIR spectra and solubility results indicate that imidization was incomplete and that cross-linking reactions had not taken place until after 3 h of curing. The low tensile properties and high solubility of the 1-h-cured shells were attributed to the absence of cross-linking and/or lower MW due to incomplete imidization.

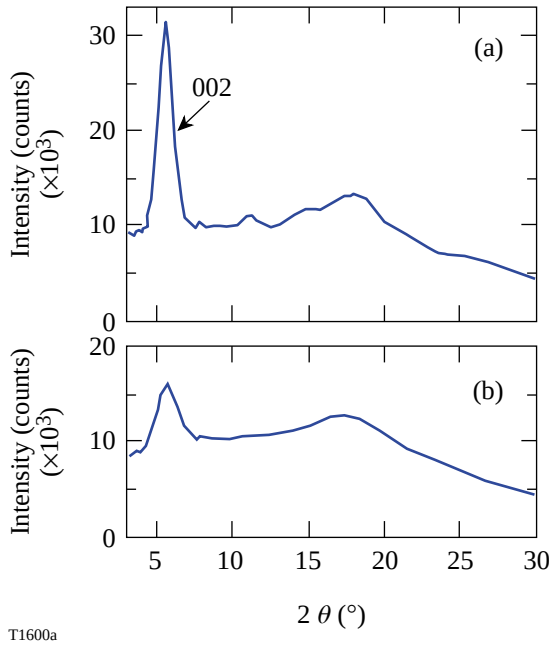

Figure 88.35
1-D x-ray microdiffractometer patterns integrated from 2-D transmission patterns of (a) N_2-imidized and (b) air-imidized samples.

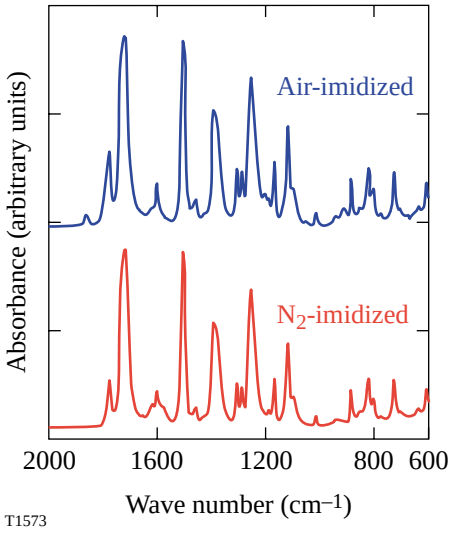

Figure 88.36
FTIR spectra of air- and N_2-imidized VDP polyimide.

Table 88.V: Properties of N_2- and air-imidized VDP polyimide. The permeability and solubility were measured with both film and shell samples, and the other properties were measured with shells only. The imidization conditions (0.1°C/min; 6 h) were the same except for the atmosphere.

Imidizing conditions	Mechanical Properties			Gas Permeability (mol·m/m²·Pa·s)			Solubility in H_2SO_4
	E (GPa)	σ (MPa)	ε	He × 10^{16}	D_2 × 10^{16}	N_2 × 10^{18}	
N_2	3.2±0.1	280±19	0.27±0.02	4.9±0.1	3.5±0.1	3.9±0.2	insoluble
Air	3.0±0.2	191±11	0.13±0.03	11.7±0.6	7.6±0.5	8.5±0.2	insoluble

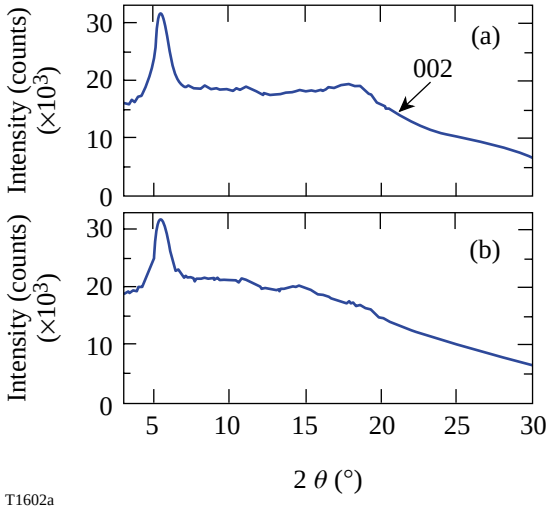

Figure 88.37
1-D x-ray microdiffractometer patterns integrated from 2-D transmission patterns of shells imidized at (a) 0.1°C/min and (b) 1°C/min.

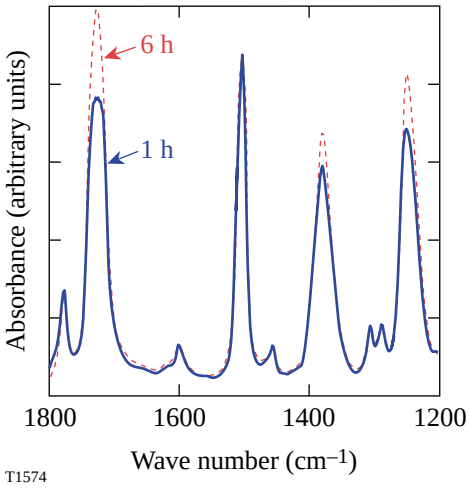

Figure 88.38
FTIR spectra of VDP polyimide imidized for 1 h and 6 h at 300°C.

Table 88.VI: Properties of VDP polyimide imidized at different heating rates. The solubility was tested with both film and shell samples, and the other properties were measured with shells only. The imidization conditions (nitrogen; 6 h) were the same except for the heating rate.

Imidizing conditions	Mechanical Properties			He Permeability × 10^{16} (mol·m/m^2·Pa·s)	Solubility in H_2SO_4
	E (GPa)	σ (MPa)	ε		
0.1°C/min	3.2±0.1	280±19	0.27±0.02	4.9±0.1	insoluble
0.5°C/min	3.3±0.3	230±26	0.08±0.02	5.3±0.1	insoluble
1.0°C/min	3.3±0.3	136±6	0.03±0.01	5.6±0.2	soluble

Table 88.VII: Properties of VDP polyimide shells imidized for different durations at 300°C. The solubility was tested with both film and shell samples, and the other properties were measured with shells only. The imidization conditions (nitrogen; 0.1°C/min) were the same except for the duration.

Imidizing conditions	Mechanical Properties			He Permeability × 10^{16} (mol·m/m^2·Pa·s)	Solubility in H_2SO_4
	E (GPa)	σ (MPa)	ε		
1 h	3.4±0.2	100±10	0.15±0.03	4.1±0.1	soluble
3 h	3.2±0.1			4.6±0.1	insoluble
6 h	3.2±0.1	280±19	0.27±0.02	4.9±0.1	insoluble

4. Biaxial Straining and Permeability

Approximately 150 imidized shells that had been inflated with a biaxial strain of ~0.25 were tested for permeability. The results are summarized in Table 88.VIII. The permeability of the shells increased; however, the magnitude of the increase fell into two categories: ~1/3 of the tested shells became ~1000-fold more permeable, while ~2/3 showed a moderate increase of ~25%. Upon heating to 350°C (within the reported T_g range for polyimide)[14] in nitrogen for 1 h, these shells were recovered to their original dimensions and permeability.

The XRD patterns of the shells before and after straining are shown in Fig. 88.39. Straining the shells decreased their crystallinity as indicated by the reduced intensity of the 002 peak. The lowered crystallinity may account for the moderate permeability increase of the strained shells. It is speculated that the ~1000-fold increase in permeability resulted from crazing/shear-banding, which can create microvoids in the shells and thus greatly expedite permeation.[20] Importantly, the structural integrity of the inflated shells was not affected since they could be repeatedly flattened and recovered by pressure differential and could contain liquid D_2 at cryogenic temperatures.

5. Cryogenic Permeability

The temperature dependency of the helium permeability through Kapton and VDP films is plotted in Fig. 88.40. The data measured with Kapton agree with those reported by S. A. Letts *et al.*[9] Both materials followed the Arrhenius relationship over the measured temperature range. The activation energy for permeation calculated from the data was 19.5 and 16.0 KJ/mol for VDP and Kapton, respectively. The good temperature–permeability correlation will allow the permeability to be estimated in an extended temperature range. The higher activation energy of VDP polyimide may be due to its

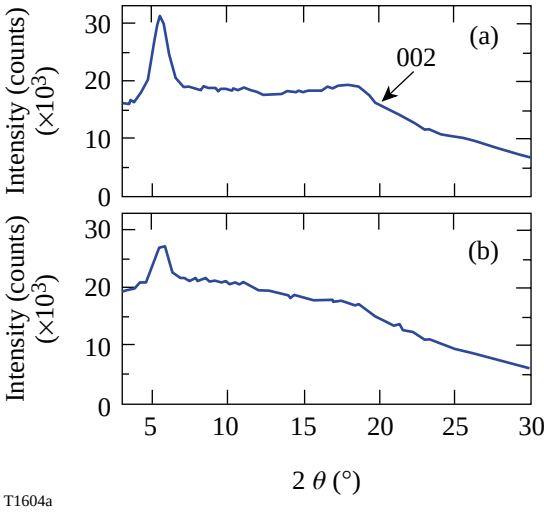

Figure 88.39
1-D x-ray microdiffractometer patterns integrated from 2-D transmission patterns of (a) pristine and (b) inflated shells.

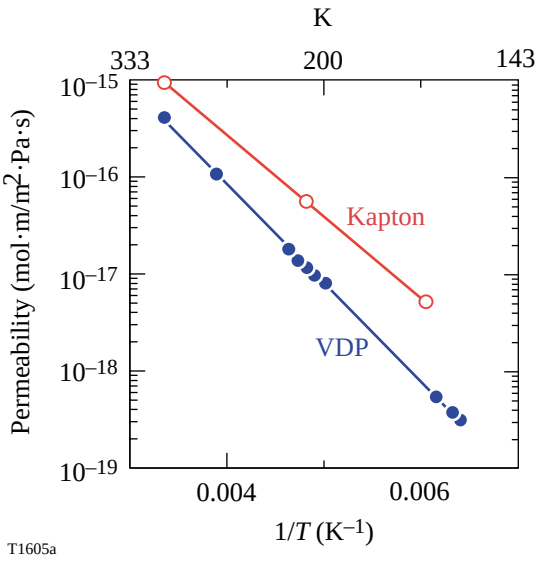

Figure 88.40
Temperature dependency of the helium permeability of VDP and solution-cast polyimide (Kapton) at cryogenic temperatures.

Table 88.VIII: Permeability of polyimide shells before and after straining.

	Permeability (mol·m/m²·Pa·s)		
	Before straining (120 shells)	Biaxially strained (~0.25)	
		80 shells	40 shells
He × 10^{16}	4.9±0.1	6.2±0.2	NA*
N_2 × 10^{18}	3.9±0.2	Not measured	500 → 4000

*Permeability too high to measure using current apparatus.

being cross-linked. For polymeric materials, the activation energy is determined by the segmental mobility of the molecules; the segmental mobility is limited when the molecules are cross-linked, resulting in high activation energy.[21]

6. Surface Finish

Figure 88.41 displays the power spectra calculated from the sphere maps of a 1.7-μm-wall shell, inflated and deflated, as described in the **Experimental Section** above. The mode-2 to -20 roughness was reduced when the shell was inflated, suggesting that the low-mode roughness may instead be a "waviness" in the shell wall, which can be eliminated by inflation. Based on this observation, the low-mode roughness of thin-wall cryogenic targets may be significantly reduced since they are kept inflated during application.[22]

The SEM micrographs of the surface of as-deposited shells prepared with unheated and heated substrates are shown in Fig. 88.42. Contrary to our expectation that a heated substrate would re-evaporate unreacted monomers and thus eliminate high-mode roughness (coating-induced bumps),[4] the number density of coating-induced bumps increased with the coating temperature. This may be due to two mechanisms: (1) At higher temperatures the coating rate was slower (50% slower at 140°C than at 25°C), thus the shells experienced more abrasion and collisions, reported to increase surface roughness,[4] over the longer period required to achieve equivalent thickness. (2) The stoichtometry was offset by disproportional re-evaporation of PMDA and ODA, which have different vapor pressures at 120°C to 140°C.

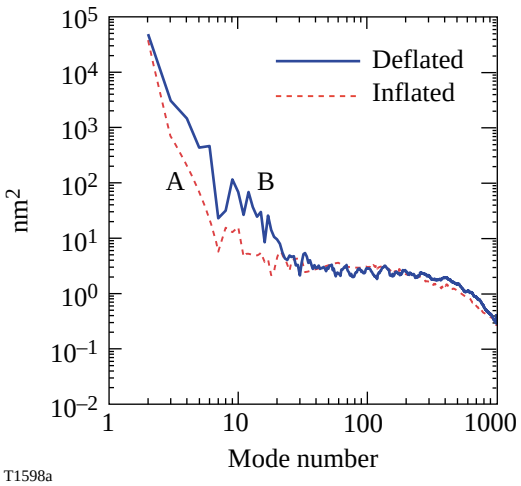

Figure 88.41
Power spectra of a thin-walled (1.8-μm) polyimide shell: A–inflated (~1%) by 6.5 atm N_2; B–deflated after the fill gas permeated out.

7. Summary

Vapor-deposited polyimide shells had properties equivalent to commercial polyimide films. The fabrication process was studied parametrically to optimize the shell properties, qualities, and yield, and the results can be summarized in the following:

- Strength and surface smoothness of PAA coating were achieved by maintaining an equimolar deposition of the precursor monomers over the substrate surface. Factors that affected the monomer deposition rates included the evaporating temperature and the geometrical arrangement of the substrate.

- The stress generated during imidization due to depolymerization of PAMS mandrels determined the yield of polyimide shells, which could be controlled by varying the imidization conditions. Imidizing at 0.1°C/min in nitrogen atmosphere minimized the stress and provided the highest yield.

- Shells imidized in air were twice as permeable, ~75% as strong, and ~50% as flexible as their counterparts imidized in nitrogen; the Young's modulus was unaffected; and the crystallinity and MW were lower.

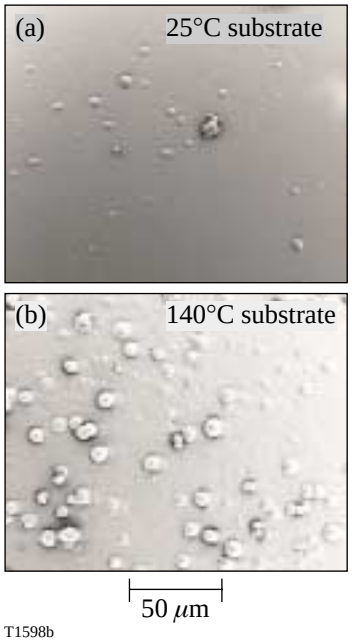

Figure 88.42
SEM micrographs of the surface of as-deposited shells (6-μm coating) prepared at (a) 25°C and (b) 140°C substrate temperatures.

- Increasing the imidization rate increased the permeability (~25%) and solubility and decreased the strength (~50%) and flexibility (~200%), while maintaining the Young's modulus. The samples imidized at the fastest heating rate became soluble with lower crystallinity.

- Imidizing for less than 3 h at 300°C resulted in lower strength, flexibility, and permeability and produced polyimide that was soluble. The imidization was incomplete at 1 h, which may have led to lower MW and the absence of cross-linking.

- Biaxial straining increased the permeability by up to three orders of magnitude but reduced the crystallinity.

- Inflating thin-wall shells reduced the low-mode surface roughness; heating the substrate during coating increased the high-mode roughness.

Conclusion

Polyimide shells can be reproducibly prepared with dimensions required for ICF targets. The properties and quality of shells can be modified and improved via processing parameters. The modifications in the shell properties are attributed to changes in crystallinity, degree of cross-linking, or molecular weight.

ACKNOWLEDGMENT

This work was supported by the U.S. Department of Energy Office of Inertial Confinement Fusion under Cooperative Agreement No. DE-FC03-92SF19460, the University of Rochester, and the New York State Energy Research and Development Authority. The support of DOE does not constitute an endorsement by DOE of the views expressed in this article.

REFERENCES

1. J. J. Sanchez and S. A. Letts, Fusion Technol. **31**, 491 (1997).
2. F. Y. Tsai, E. L. Alfonso, S.-H. Chen, and D. R. Harding, Fusion Technol. **38**, 83 (2000).
3. E. L. Alfonso, S. H. Chen, R. Q. Gram, and D. R. Harding, J. Mater. Res. **13**, 2988 (1998).
4. C. C. Roberts *et al.*, Fusion Technol. **35**, 138 (1999).
5. A. Nikroo and D. Woodhouse, Fusion Technol. **35**, 202 (1999).
6. R. Jenkins and R. L. Snyder, *Introduction to X-Ray Powder Diffractometry* (Wiley, New York, 1996), Chap. 7, pp. 173–203.
7. B. A. Squires and K. L. Smith, in *Advances in X-Ray Analysis*, edited by P. K. Predecki *et al.* (Plenum Press, New York, 1995), Vol. 38, pp. 511–516.
8. F. Y. Tsai, E. L. Alfonso, S. H. Chen, and D. R. Harding, "Processing Vapor-Deposited Polyimide," to be published in the Journal of Physics D.
9. S. Letts *et al.*, presented at the Twelfth Target Fabrication Specialists' Meeting, Jackson Hole, WY, 19–23 April 1998.
10. T. Strunskus and M. Grunze, in *Polyimides: Fundamentals and Applications*, edited by M. K. Ghosh and K. L. Mittal, Plastics Engineering, Vol. 36 (Marcel Dekker, New York, 1996), pp. 187–205.
11. E. L. Alfonso, F.-Y. Tsai, S.-H. Chen, R. Q. Gram, and D. R. Harding, Fusion Technol. **35**, 131 (1999).
12. R. G. Pethe *et al.*, J. Mater. Res. **8**, 3218 (1993).
13. C. C. Roberts *et al.*, Fusion Technol. **38**, 94 (2000).
14. Kapton® product literature, DuPont™ High Performance Polymers, Circleville, OH 43113.
15. W. Volksen, P. Cotts, and D. Y. Yoon, J. Polym. Sci. B, Polym. Phys. **25**, 2487 (1987).
16. P. M. Cotts and W. Volksen, ACS Symp. Ser. **242**, 227 (1984).
17. C. E. Rogers, in *Polymer Permeability*, edited by J. Comyn (Elsevier, London, 1985), Chap. 2, pp. 11–73.
18. G. A. Patfoort, *Polymers: An Introduction to Their Physical, Mechanical and Rheological Behaviour* (Story-Scientia, Gent, Belgium, 1974), pp. 321–323.
19. F. W. Billmeyer, Jr., *Textbook of Polymer Science*, 3rd ed. (Wiley, New York, 1984), Chap. 12, pp. 330–357.
20. E. H. Andrews, in *The Physics of Glassy Polymers*, edited by R. N. Haward (Wiley, New York, 1973), pp. 394–453.
21. A. Singh-Ghosal and W. J. Koros, Ind. Eng. Chem. Res. **38**, 3647 (1999).
22. I. Anteby, Ben-Gurion University of the Negev, private communication (1996).

LLE's Summer High School Research Program

During the summer of 2001, 13 students from Rochester-area high schools participated in the Laboratory for Laser Energetics' Summer High School Research Program. The goal of this program is to excite a group of high school students about careers in the areas of science and technology by exposing them to research in a state-of-the-art environment. Too often, students are exposed to "research" only through classroom laboratories, which have prescribed procedures and predictable results. In LLE's summer program, the students experience many of the trials, tribulations, and rewards of scientific research. By participating in research in a real environment, the students often become more excited about careers in science and technology. In addition, LLE gains from the contributions of the many highly talented students who are attracted to the program.

The students spent most of their time working on their individual research projects with members of LLE's technical staff. The projects were related to current research activities at LLE and covered a broad range of areas of interest including optics modeling, laser characterization, cryogenic materials properties, liquid crystal chemistry, laser damage, electro-optic sampling, and the development, modeling, and control of laser fusion diagnostics (see Table 88.IX).

The students attended weekly seminars on technical topics associated with LLE's research. Topics this year included lasers, fusion, holography, the OMEGA Cryogenic Target System, laboratory astrophysics, experimental error analysis, and scientific ethics. The students also received safety training, learned how to give scientific presentations, and were introduced to LLE's resources, especially the computational facilities.

The program culminated on 29 August with the "High School Student Summer Research Symposium," at which the students presented the results of their research to an audience including parents, teachers, and LLE staff. The students' written reports will be bound into a permanent record of their work that can be cited in scientific publications. These reports are available by contacting LLE.

One hundred and thirty high school students have now participated in the program since it began in 1989. The students this year were selected from approximately 50 applicants.

In 1997, LLE added a new component to its high school outreach activities: an annual award to an Inspirational Science Teacher. This award honors teachers who have inspired High School Program participants in the areas of science, mathematics, and technology and includes a $1000 cash prize. Teachers are nominated by alumni of the High School Program. Mr. David Dussault, a mathematics and computer science teacher at Livonia High School, was the recipient of LLE's 2001 William D. Ryan Inspirational Teacher Award. Mr. Michael Harvey, a participant in the 1999 Summer Program who nominated Mr. Dussault, writes of his former teacher, "His approach to teaching is unique. He challenges students to work at their own pace and learn on their own. Even more impressive to me than his wisdom in preparing me for college is his love for pure education. Mr. Dussault finds the way to get his message across to every type of student." Mr. Scott Bischoping, principal of Livonia High School, also had many words of praise for Mr. Dussault. He said he has been continually impressed with Mr. Dussault's contributions to both the Math and Computer Science Departments. Two accomplishments that stood out in his mind were the success of a curriculum Mr. Dussault developed, which allows students to earn college math credits, and his dedicated leadership to the school's math team in state and local competitions.

Table 88.IX: High School Students and Projects—Summer 2001.

Name	High School	Supervisor	Brief Project Title
David Bowen	Greece Arcadia	C. Stoeckl	Controlling Scientific Instruments with JAVA
Matthew Fiedler	Brighton	W. Donaldson	Modeling Streak Camera Sweep Speeds
Melisa Gao	Brighton	J. Marozas	Two-Dimensional Phase Unwrapping for the Design of Distributed Phase Plates
Brian Ha	Gates Chili	R. Sobolewski	Optical Characterization of GaAs with MSM Structures
Gabrielle Inglis	Honeoye Falls-Lima	R. Boni	Building and Characterizing 14-GHz InGaAs Fiber-Coupled Photodiodes
Jennifer Jung	Victor	K. Marshall	Guest-Host Dye Systems for Liquid Crystal Electro-Optical Device Application
Joshua Keegan	Aquinas Institute	M. Guardalben	Numerical Modeling of Optical Parametric Chirped Pulse Amplification
Kevin Monajati	Pittsford-Sutherland	K. Marshall	Computational Modeling of Physical Properties in Liquid Crystalline Polymer Systems
Christopher Piro	Honeoye Falls-Lima	R. S. Craxton	Modeling the LCPDI with Refraction and Diffraction
Abagail Rhode	Brockport	J. Taniguchi	Experimental Simulation of Damage in Spatial Filter Lenses
Uyen Tran	Wilson Magnet	S. Regan	Experimental Investigation of the Far Field on OMEGA with an Apertured Near Field
James Wang	McQuaid Jesuit	D. Harding	Cyrogenic Permeability of Polyimide Shells
Jeffrey Wilbur	Victor	J. Lambropoulos	Inclusion Models of Laser Damage

FY01 Laser Facility Report

Improving operational reliability for precision spherical implosions including direct-drive cryogenic targets was the primary priority for FY01 on OMEGA. Laser diagnostics and techniques to characterize and improve power balance performance were extended beyond prior achievements to allow experimentalists to probe fine details of spherical target performance. In particular, plastic-shell implosions with THz SSD (smoothing by spectral dispersion) and polarization smoothing show good reproducibility and performance. All users, including experimentalists fielding indirect-drive (ID) experiments, have benefited from the improved repeatability and reliability that has come from the power balance program. (See Table 88.X for a summary of this year's targets shots.) System improvements were also geared toward specifically improving flexibility for ID experiments. Highlights of these changes and other achievements of FY01 include the following:

- The P510 UV streak camera system was completed to provide streak camera–based pulse shape, pulse timing, and power balance for all beams on every shot. The cameras combine 1000:1 signal to noise at the peak and a bandwidth of 11 GHz. Each cluster of ten beams is captured on a single camera, thus the full complement consists of six ten-beam instruments.

- Power balance of <5% was routinely achieved for 1-ns square pulses by increased execution of periodic laser-tuning shots combined with continuous monitoring and optimization of frequency-conversion-crystal (FCC) tuning.

- Power balance on target was investigated and optimized through careful characterization of x-ray yield from the focal spot of each of the 60 beams. For some implosion shots, the results were used to adjust the power settings of the beams to investigate elimination of residual power balance errors. This technique demonstrated that peak x-ray intensity measurements of 6% rms can be improved to 2% rms.

- Cryogenic target capability was extended through deployment of additional Moving Cryostat Transfer Carts (MCTC's), increased diagnostics, and refined control. Three fully functional MCTC's have been deployed as of the end of FY01, providing flexibility between the filling station, characterization and layering station, and target delivery to OMEGA. While the maximum capacity to shoot up to eight direct-drive cryogenic targets in a week was not realized in FY01, five good cryogenic implosions were accomplished during a two-week ISE (integrated spherical experiments campaign.

- The Wide-Field Target Viewing System (WFTVS) was modified in FY01 to handle images from a mega-pixel-class camera. A 2-k × 2-k array was deployed to provide a four-fold improvement positioning capability over the entire field of view of the viewing system. Indirect-drive targets with point-imaging backlighter targets can now be more precisely positioned in the chamber.

- New elliptical-focal-spot distributed phase plates (DPP's) have been deployed. These optics can be used to create uniform, circular, drive spots on EOS targets and other planar foils when the targets are not normal to the beam. Several designs are available to compensate for the incidence angles of beams from three cones.

- A completely reengineered Path Length Adjustment System (PLAS) was developed and integrated into the system largely to accommodate the flexibility demanded by users from LLNL and LANL. The new hardware and software allow for rapid reconfiguration of beam timing on target. Staggering beam arrival times for backlighting and long drive pulses is frequently requested by the user community.

Table 88.X: The OMEGA target shot summary for FY01.

LLE-ISE	376
LLE-RTI	106
LLE LPI	50
LLE (other)	44
LLE-SSP	113
LLNL	312
LANL	124
NLUF	125
CEA	29
SNL	10
Total	1289

National Laser Users' Facility News

During FY01, 600 OMEGA target shots were taken for external users. This is a 5.1% increase over FY00 and the highest number of target shots ever taken by OMEGA external users in a single year, accounting for ~47% of the total 1289 target shots taken on the system. The external users included eight collaborative teams carrying out work under the National Laser Users' Facility (NLUF) Program as well as collaborations led by scientists from Lawrence Livermore National Laboratory (LLNL), Los Alamos National Laboratory (LANL), Sandia National Laboratory (SNL), the Nuclear Weapons Effects Testing (NWET) Program, and Commissariat à l'Énergie Atomique (CEA) of France.

FY01–FY02 NLUF Experiments

FY01 was the first year that NLUF programs were approved for a two-year period of performance (FY01 and FY02). The eight NLUF experimental campaigns received a total of 125 OMEGA target shots in FY01.

The independent DOE Technical Evaluation Panel for this period, consisting of Dr. David Bradley (LLNL), Dr. David Montgomery (LANL), Dr. Richard Olson (SNL), and Dr. Ned Sauthoff (Princeton Plasma Physics Laboratory), reviewed progress reports submitted in September 2001 by all of the current participants, confirmed that all eight participants made satisfactory progress during FY01, and recommended continued funding and shot allocations for all of the programs through FY02.

In 2Q02 DOE is expected to issue a new solicitation for NLUF programs to be carried out during FY03–FY04. The NLUF shot allocation for FY03 is 12 OMEGA shot days (~120 target shots). The NLUF DOE funding allocation for FY01 and FY02 was $700,000 to cover the participants' costs for carrying out experiments on OMEGA. It is expected that this funding level may increase in FY03/FY04 to a level more consistent with the high level of interest shown in the use of OMEGA to carry out high-energy-density physics experiments of relevance to the National Nuclear Security Agency (NNSA) Stockpile Stewardship Program (SSP).

The eight NLUF experimental campaigns carried out in FY01 included the following:

Atomic Physics of Hot, Ultradense Plasmas.
Principal Investigators: C. F. Hooper Jr. (University of Florida), D. A. Haynes (Fusion Technology Institute, University of Wisconsin), and collaborators from Los Alamos National Laboratory, the University of Wisconsin, and LLE.

The plasma environment perturbs atomic processes of radiators immersed in hot, dense plasmas. This perturbation is a challenging application of the statistical mechanics of dense plasmas and leads to observable and diagnostically useful variations in the spectrum emitted by the radiators. The focus of this work is to produce hot [electron temperature (T_e) > 1.5 keV], ultradense [electron density (n_e) ~ 5×10^{24} cm^{-3}] plasmas using the OMEGA laser in direct-drive mode. In FY01 eleven shots were performed toward this objective. Ar-doped (1% to 2% by atom) CH shells (940-μm diameter, 20 μm thick) filled with 15 atm of deuterium were used in these experiments. With 23-kJ-energy, 1-ns square laser pulses, a core $n_e > 2 \times 10^{24}$ cm^{-3} and T_e ~ 1.15 keV were observed. Because simulations indicated that ramped pulse shapes can achieve electron densities in the range of 5×10^{24} cm^{-3} to 8×10^{24} cm^{-3}, a series of ramped pulse shots were taken later in the year. These data are currently being analyzed.

Determination of Temperature and Density Gradients in Implosion Cores of OMEGA Targets.
Principal Investigators: R. C. Mancini (University of Nevada, Reno), J. A. Koch (LLNL), and collaborators from the University of Wisconsin, LLE, LLNL, and Howard University.

The goal of this project is to determine time-resolved temperature and density gradients in implosion cores on OMEGA indirect-drive implosion experiments using x-ray spectroscopy. The method is based on a novel self-consistent analysis of data from simultaneous, time-resolved x-ray line spectra and x-ray monochromatic images. Argon-doped, deuterium-filled plastic shells placed in gold hohlraums and driven

by 30 UV laser beams of OMEGA were used in these experiments. The aim was to achieve stable, spherically symmetric, and reproducible implosion cores where the proposed spectroscopic gradient determination technique can be tested and established. During FY01, a target design was successfully tested, and argon *K*-shell x-ray line spectra and monochromatic images were recorded on several shots (see Fig. 88.43).

Studies of Fundamental Properties of High-Energy-Density Plasmas.
Principal Investigator: R. Petrasso (MIT Plasma Science and Fusion Center) and collaborators from LLE, LLNL, and SUNY Geneseo.

In FY01, four different types of experiments were carried out under this program. In the first experiment, slowing-down measurements of nascent 14.7-MeV protons generated by D^3He fusion reactions were made in up to eight different directions on the same target shot to characterize the capsule's total ρR variations (see Fig. 88.44). These measurements were carried out using compact wedged range filters (WRF's). In the second class of experiments, DTH-filled CD capsules were imploded with the aim of using knock-on protons to determine the fuel ρR. In the third series of experiments, fuel–shell mix was studied by determining how much shell material is combined with the fuel at burn time. In the final set of experiments, the total ρR's at the times of shock coalescence and stagnation

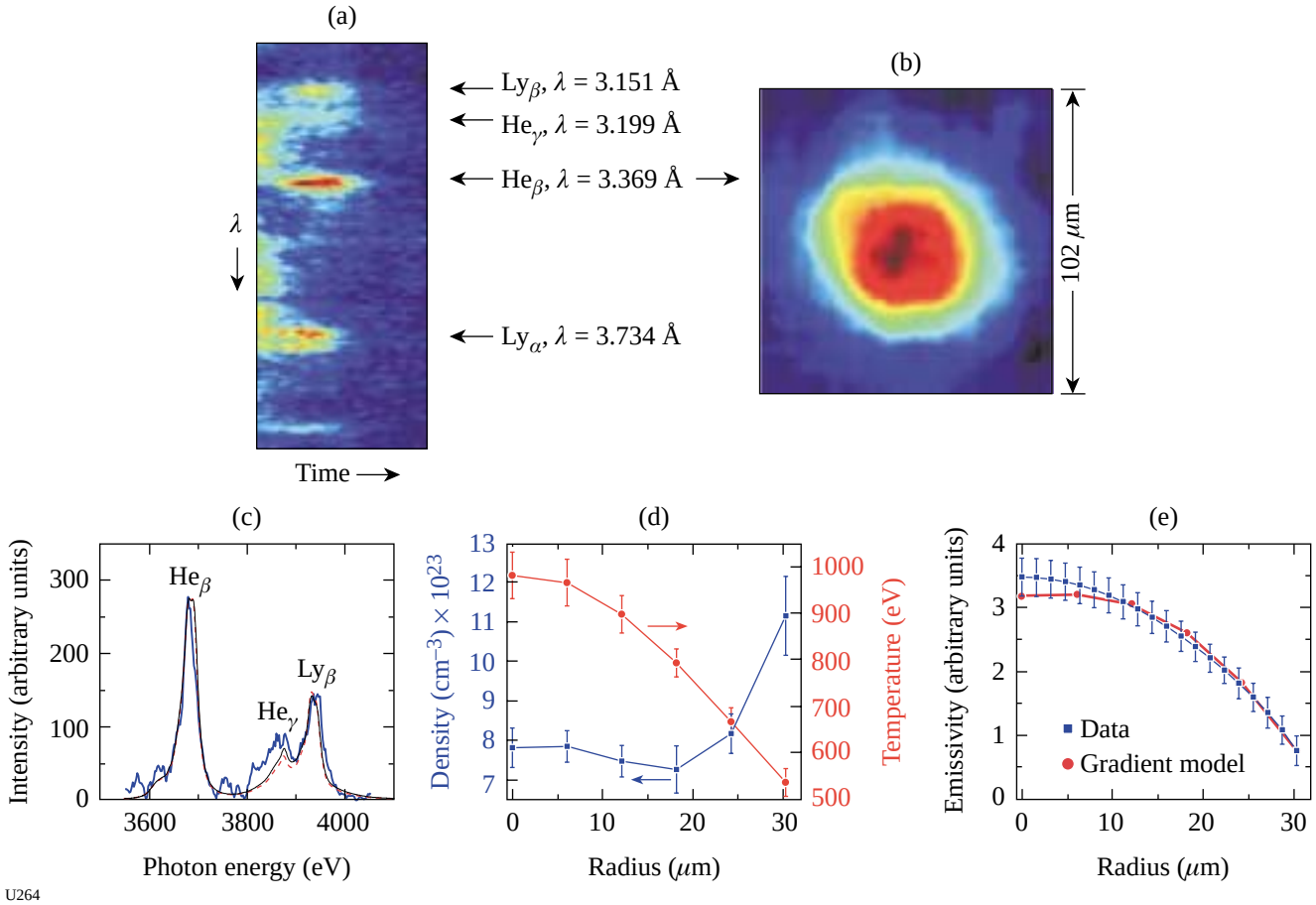

Figure 88.43
(a) Time-resolved argon *K*-shell x-ray spectrum and (b) time-integrated Heβ line monochromatic image from the implosion core of OMEGA shot 23686. (c) Synthetic spectra fits to the x-ray spectrum time-integrated over the emission interval of the Heβ line; the red dashed line is the gradient model, the thin blue line is the uniform model, and the thick blue line is the experimentally measured spectrum. (d) Electron temperature and number density core gradients. (e) Synthetic emissivity fit to the Heβ emissivity profile extracted from the monochromatic image. The emissivity-weighted averages of the gradients, $\langle N_e \rangle_\varepsilon = 7.8 \times 10^{23}$ cm^{-3} and $\langle T_e \rangle_\varepsilon = 860$ eV, show good consistency with the results of the uniform model analysis.

were differentiated. This measurement is based on a comparison of the measured energy spectra of the D^3He primary protons in implosions of D^3He-filled CH shells to those of CD/CH shells filled with only ^3He (see Fig. 88.45).

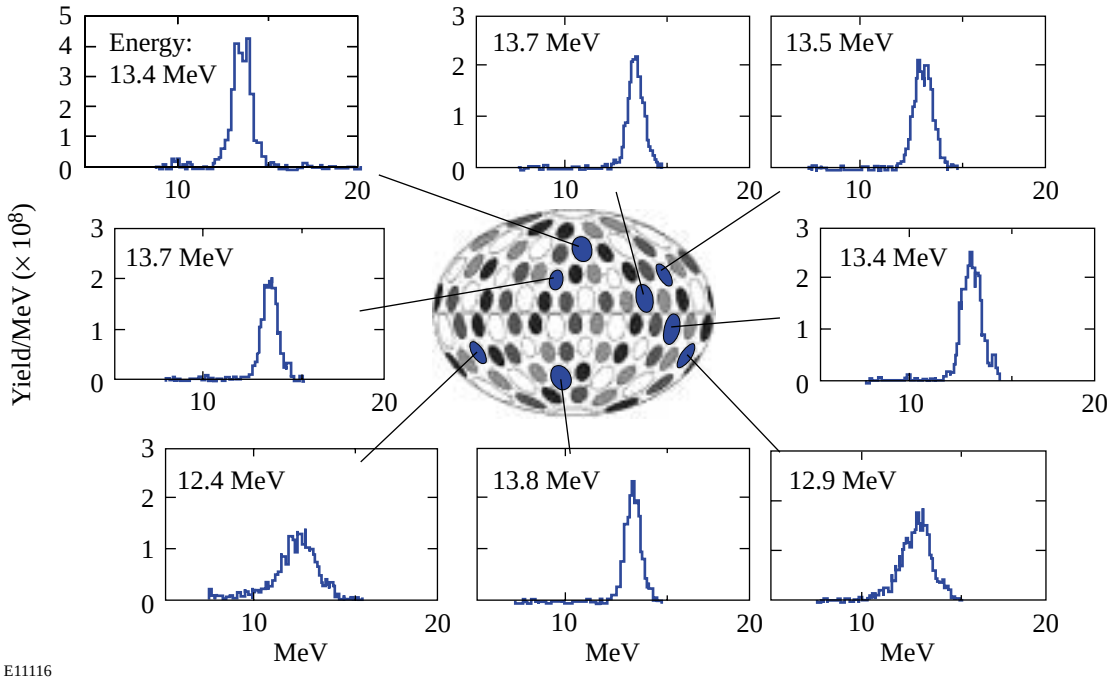

Figure 88.44
Data showing 14.7-MeV primary proton slowing down from the implosion of a D^3He-filled capsule. These data are obtained by a combination of seven wedged-range filters (WRF's) and two charged-particle spectrometers (CPS's). Note the variation in mean energy of the protons as a function of angular position. These data imply that there are significant low-ℓ-mode variations in the total areal density of the imploded capsule.

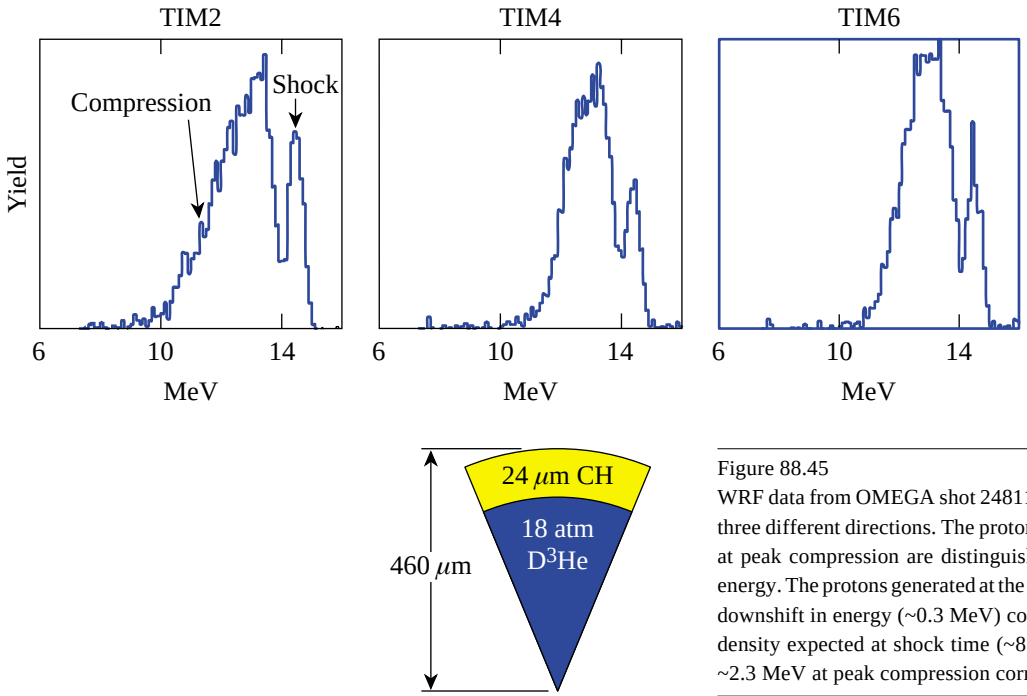

Figure 88.45
WRF data from OMEGA shot 24811 showing primary proton spectra from three different directions. The proton yield at shock time and that produced at peak compression are distinguished by the difference in mean proton energy. The protons generated at the time of the first shock have only a small downshift in energy (~0.3 MeV) corresponding to the lower capsule areal density expected at shock time (~8 mg/cm^2) compared to a downshift of ~2.3 MeV at peak compression corresponding to a ρR ~ 70 mg/cm^2.

Studies of the Dynamic Properties of Shock-Compressed FCC Crystals by In-Situ *Dynamic X-Ray Diffraction.*
Principal Investigators: H. Baldis (University of California at Davis), D. H. Kalantar (LLNL), and collaborators from LLNL, LLE, University of California at San Diego, University of Oxford, and LANL.

This experiment uses time-resolved dynamic x-ray diffraction to study the response of a lattice under shock compression as the shock passes through the sample. Recovery of target samples for laboratory examination allowed the residual deformation effects to be examined directly. The shots this year were aimed at developing the capability to record diffraction from multiple lattice planes during passage of a shock through a thin foil of single-crystal copper. Simultaneous recovery of separate shock samples experiments were conducted.

During FY01, the diffraction from the (200) and (020) lattice planes of Cu were recorded using a V x-ray source (2.38 Å). In addition, a modified target was tested using a Cu x-ray source (1.4 Å) to record the (400) lattice planes of Cu. Fielding a large-solid-angle film holder on diffraction experiments taken in August 2001 extended the technique further (see Fig. 88.46).

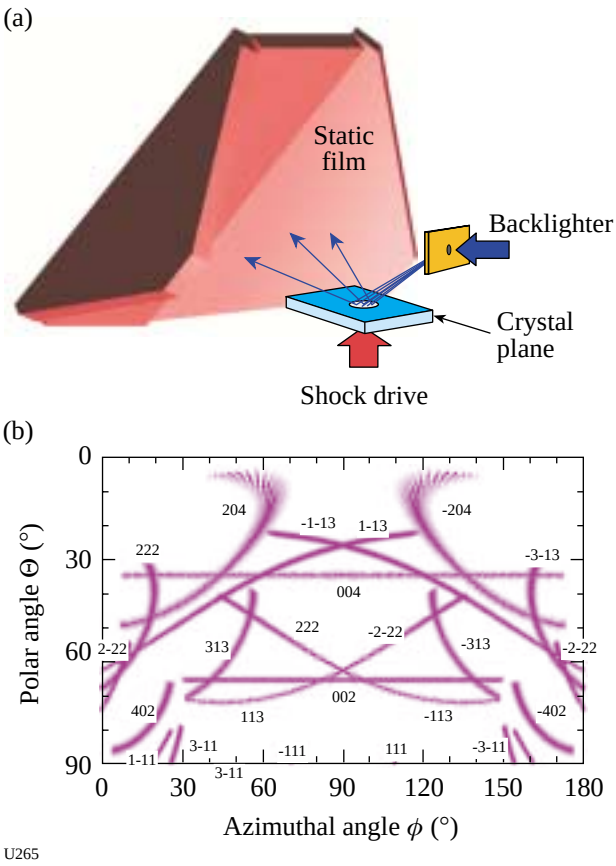

Figure 88.46
(a) Schematic of a static film-based detector that records x rays diffracted from many different lattice planes covering nearly a π-steradian solid angle. (b) Simulated diffraction pattern from multiple lattice planes of Si.

High-Spatial-Resolution Neutron Imaging of Inertial Fusion Target Plasmas Using Bubble Neutron Detectors.
Principal Investigator: Raymond K. Fisher (General Atomics) and collaborators from LLE, CEA, and LLNL.

Bubble detectors capable of detecting neutrons with a spatial resolution of 5 to 30 μm are one of the most-promising approaches to imaging NIF target plasmas with the desired 5-μm spatial resolution in the target plane. Gel bubble detectors are being tested to record neutron images of ICF implosions in OMEGA experiments. By improving the noise reduction techniques used to analyze the data taken in June 2000, it was possible to image the neutron emission from 6×10^{13}-yield DT target plasmas with a target plane spatial resolution of ~140 μm, as shown in Fig. 88.47. As expected, the spatial resolution was limited by counting statistics as a result of the low neutron detection efficiency of the easy-to-use gel bubble detectors. The results, which have been submitted for publication, were presented as an invited talk at the October 2001 Meeting of the Division of Plasma Physics of the American Physical Society.

To improve the counting statistics, data taken in May 2001 using a stack of four gel detectors were integrated over a series of up to seven high-yield DT shots. Analysis of the 2001 data is still in its early stages. Gel detectors were chosen for these initial tests since the bubbles can be photographed several hours after the neutron exposure. They consist of ~5000 drops (~100 μm in diameter) of bubble detector liquid/cm^3 suspended in an inactive support gel that occupies ~99% of the detector volume. Using a liquid bubble chamber detector, along with a light-scattering system to record the bubble locations a few microseconds after the neutron exposure when the bubbles are ~10 μm in diameter, should result in ~1000 times higher neutron detection efficiency and a target plane resolution on OMEGA of ~10 to 50 μm.

Examination of the "Cone-in-Shell" Target Compression Concept for Asymmetric Fast Ignition.
Principal Investigators: Richard B. Stephens (General Atomics) and collaborators from LLNL and the Institute of Laser Engineering (ILE), Osaka University, Osaka, Japan.

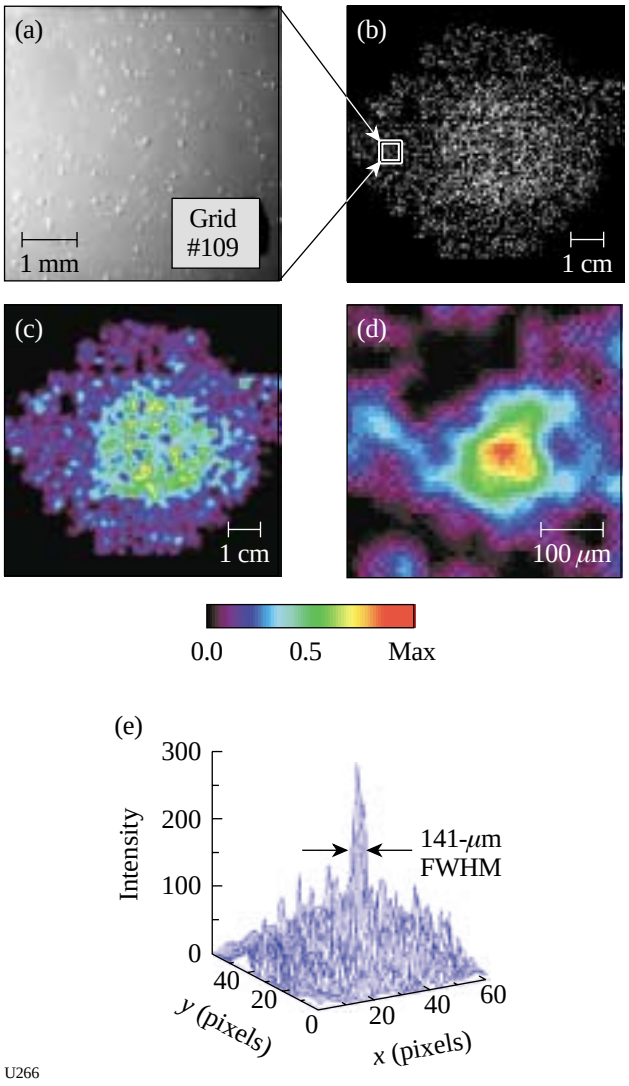

Figure 88.47
Bubble detector images from a 6×10^{13}-yield OMEGA shot, including (a) a microscope photograph of 60-μm-diam bubbles in a single grid location, (b) an x–y plot of bubble locations, (c) a coded false color image in the detector plane, and (d) and (e) an unfolded neutron image in the target plane.

Studies of the compression hydrodynamics of targets suitable for the fast-ignition inertial fusion concept have been initiated. The objective is to assemble a dense core of material while maintaining clear access for the ignition pulse through the low-density blowoff. A hollow, high-density cone inserted in the side of the shell and placed inside a cylindrical hohlraum can be used to maintain the ignition pulse access. The cone causes anisotropies in the shell implosion: radiation intensity changes and shear near the cone surface modify the local implosion velocity, and the dense core is assembled from only a partial shell. Modeling (Steve Hatchett, LLNL) suggested that the consequences of these asymmetries would be relatively minor; it should be feasible to assemble a dense, nearly spherical core with a piece missing. A model system using a hohlraum-driven target was set up to test prediction, and backlit framing camera pictures of the model system were compared to the simulation. The predicted and experimental images look similar (see Fig. 88.48) but there were subtle differences. The collapse time might have changed since the experimental shell density was about half that expected in the interval of the framed images. In addition, the shell seems less separated from the cone, and the cone shape is less defined in the experimental images compared to the simulation. Further analysis will continue in order to understand these changes and to optimize our experimental setup for the next round of experiments.

Supernova Hydrodynamics on the OMEGA Laser.
Principal Investigators: R. Paul Drake (University of Michigan), B. Remington (Center for Laser Astrophysics-ILSA, LLNL), and collaborators from LLNL, CEA Saclay (France), LLE, LANL, University of Arizona, University of Colorado, University of Chicago, SUNY Stony Brook, Naval Research Laboratory, and Eastern Michigan University.

The fundamental motivation of this program is that supernovae are not well understood. Experiments are performed in compressible hydrodynamics and radiation hydrodynamics, relevant to supernovae and supernovae remnants. These experiments produce phenomena in the laboratory that are thought, based on simulations, to be important to astrophysics but that have not been directly observed either in the laboratory or in an astrophysical system. During FY01, this work has focused on the production of an astrophysically relevant, radiative shock and on the three-dimensional, deeply nonlinear evolution of the Rayleigh–Taylor (RT) instability at a decelerating, embedded interface. These experiments required strong compression and decompression, strong shocks (Mach ~ 10 or greater), flexible geometries, and very smooth laser beams, which means that the 60-beam OMEGA laser is the only facility capable of carrying out this program.

Highlights of these Supernova Hydrodynamics experiments include the following:

a. Radiative Precursor Shocks: These experiments involved the initial acceleration of a block of material to high velocity with up to ten OMEGA beams. This block of material then drove a shock wave through low-density foam at a velocity of ~100 km/s, which was fast enough to produce a radiative

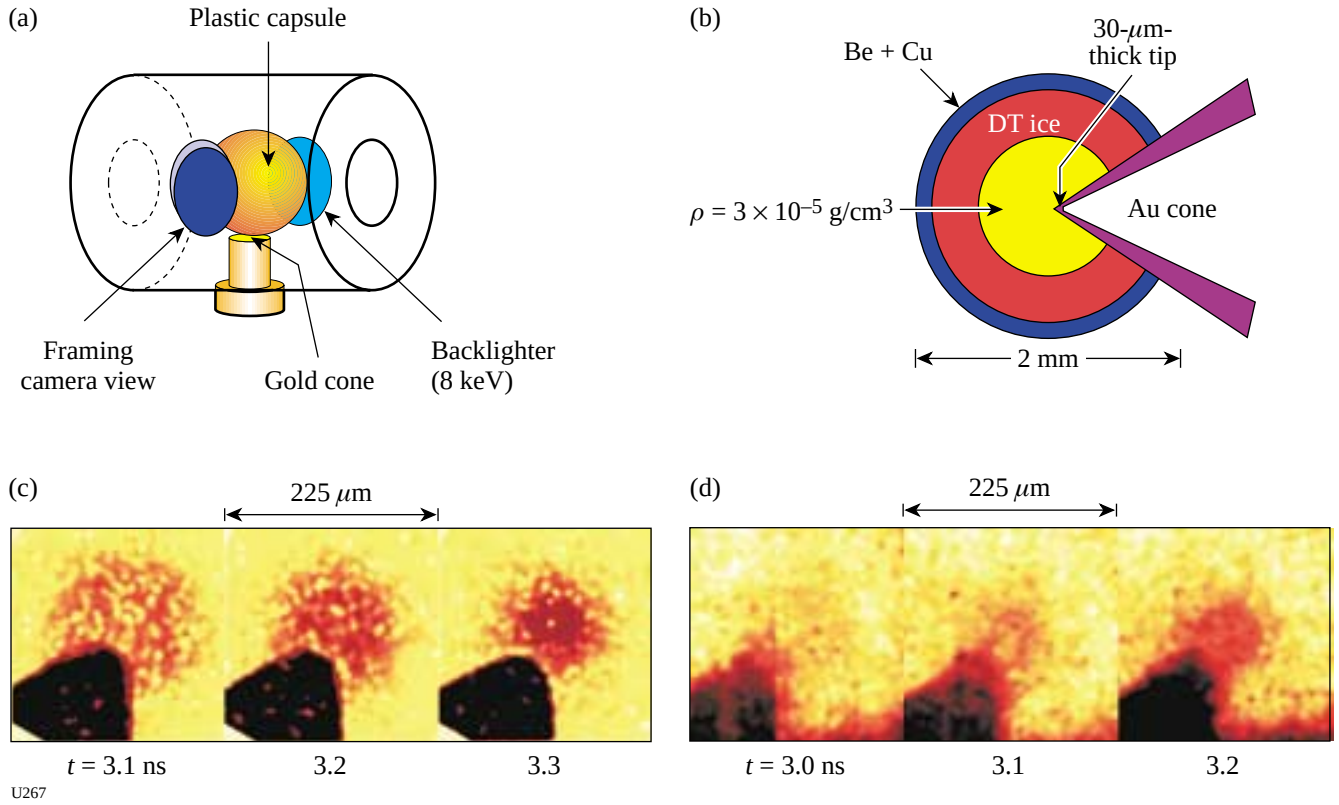

Figure 88.48
(a) Schematic of NIF-scale fast-ignition target; (b) schematic of OMEGA-scale experiment to test the concept; (c) computer simulation of x-ray backlit images of an OMEGA target; and (d) observed backlit images of an OMEGA target experiment just before stagnation.

precursor. The structure of the precursor was diagnosed with absorption spectroscopy using a thulium target. Absorption lines were detected from up to six different ionization states (see Fig. 88.49). The lines from higher ionization states appear at higher temperatures. This allows one, with the help of the OPAL atomic code,[1] to determine the temperature profile in the precursor. It is expected that such experiments will provide quality benchmark cases for astrophysical modeling.

b. 2-D versus 3-D Rayleigh–Taylor: A major issue in the evolution of supernovae is whether three-dimensional effects can resolve the differences between reality and simulations, nearly all of which are carried out in two dimensions. A few 3-D simulations, not yet benchmarked, suggest that 3-D effects are not sufficient to resolve these differences. During FY01, experiments were continued to compare the deep nonlinear evolution of the RT instability at an embedded interface in both two dimensions and three dimensions (examples from two FY00 shots are shown in Fig. 88.50).

c. Multimode Perturbations and the Onset of Turbulence: During the past year, the study of RT at an embedded interface was extended to begin to examine the growth of multimode perturbations. In addition, the experimental system was analyzed in the context of recent theories regarding the onset of turbulence at shear layers like those between the bubbles and the spikes.

d. Spherically Diverging Experiments: During the past year, a small amount of improved data was obtained on spherically diverging unstable systems. Papers now in progress describe the results obtained on these experiments.

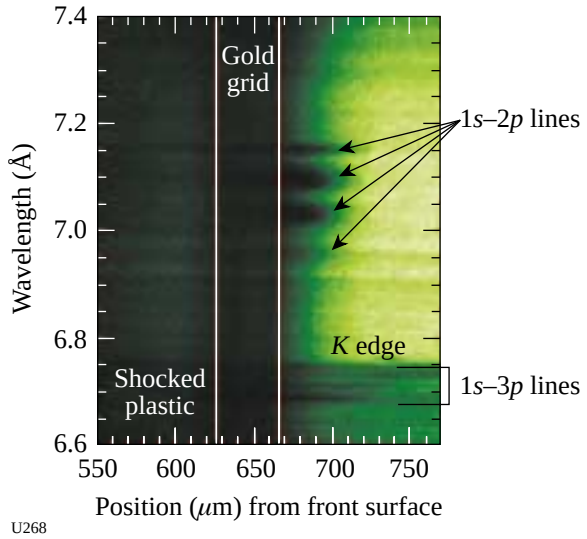

Figure 88.49
An absorption spectrum from the radiative precursor shock experiments at 5.5 ns after the onset of a 1-ns laser pulse The absorption lines extending to the right of the grid in the image can be analyzed to determine the temperature profile. Initial results show a much shorter precursor than simulations predict.

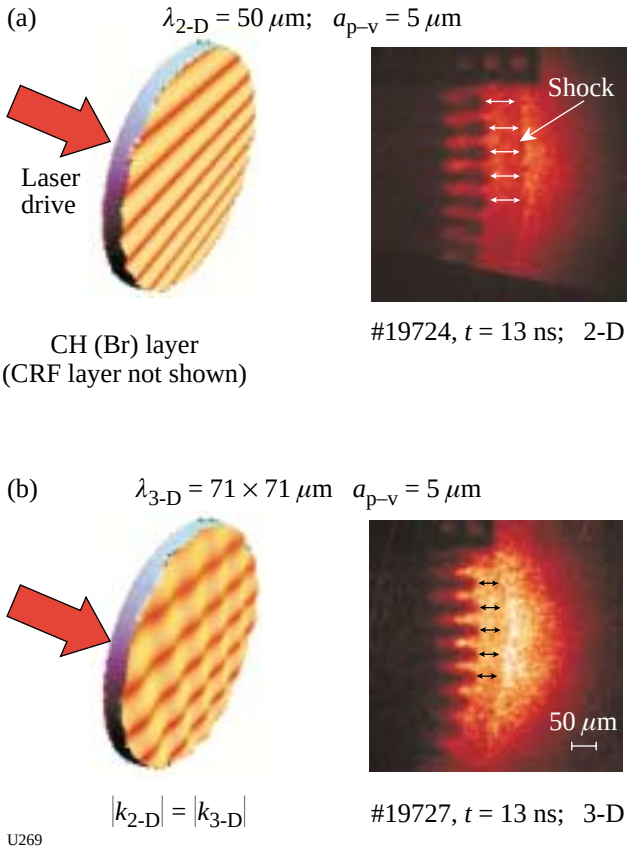

Figure 88.50
Spikes produced by the Rayleigh–Taylor instability during the deceleration of a structured interface. The spikes produced by a 3-D "egg crate" pattern (b) are longer and extend closer to the shock than those produced by a rippled (2-D) interface (a).

Optical-Mixing-Controlled Stimulated Scattering Instability Experiments on OMEGA (III) and (IV): Suppressing Backscattering Instabilities by the Externally Controlled Generation of Ion-Acoustic Turbulence.
Principal Investigator: Bedros Afeyan (Polymath Research Inc.) and collaborators from LANL, University of Nevada at Reno, LLNL, and LLE.

The prime objective of this program is to suppress backscattering instabilities by the externally controlled generation of ion-acoustic-wave (IAW) and electron-plasma-wave (EPW) turbulence in different IAW damping regimes. During FY01, the work was directed toward two goals: (1) to generate large-amplitude IAW's at or near the Mach-1 surface of an exploding-foil target (on the pump side of the density peak), and (2) to measure how this reduces the stimulated Raman scattering (SRS) and stimulated Brillouin scattering (SBS) backscattering levels of the pump when the probe/pump energy ratio is high enough.

Planar-foil targets of 5-μm-thick Be were used for the first time this year. According to the hydrodynamic simulations, these Be targets are hydrodynamically similar to the 10-μm-CH targets used in previous years' experiments. A major result of this year's work was the demonstration for the first time in equal-frequency crossed beam experiments in flowing plasmas of greater-than-100% transmission of a probe beam intensity due to its interaction with the pump beam and the subsequent energy transfer (see Fig. 88.51). It was also shown that SRS backscattering of the pump beam is suppressed by a factor of 6 or more in the presence of a large IAW driven by the crossing pump and probe beams at or near the Mach-1 surface even in this weak IAW damping limit.

The quality of this year's experiments was improved because it was possible to carry out probe beam intensity scaling experiments using "frequency-conversion-crystal detuning" to adjust the probe beam amplitude. This technique, attempted for the first time during these OMC SSI experiments, allows nearly square, 1-ns laser pulses to be generated over the UV energy range of 30 J to 500 J on target without adjusting the input laser pulse shape of the OMEGA laser.

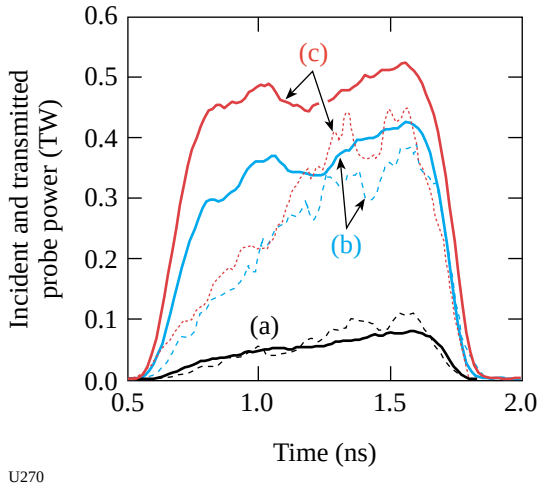

	Incident probe energy (J)	Energy transfer (%)
a	61	109
b	378	68
c	510	58

Figure 88.51
Optical-mixing-controlled stimulated scattering instability experiments on OMEGA (III) and (IV). Incident (solid curves) and transmitted (dashed or dotted curves) probe beam intensity as a function of time for different probe beam energy levels. At the probe beam energy level of 61 J, the transmitted beam intensity reaches 109% of that incident through the transfer of energy from the pump beam.

FY01 National Laboratory, NWET, and CEA Programs

OMEGA continued a high rate of shot production for external users from the national laboratories (LLNL, LANL, and SNL) as well as from the Nuclear Weapons Effects Testing (NWET) Program, the United Kingdom Atomic Weapons Establishment (AWE), and the Commissariat à l'Énergie Atomique (CEA) of France. A total of 475 target shots were taken for these programs in FY01. The following is a brief summary:

1. LLNL and NWET Campaigns

In FY01 LLNL had 320 shot opportunities at the OMEGA facility, divided as follows: 110 shots for target ignition physics (TIP), 190 shots for high-energy density science (HEDS), and 20 shots for NWET. These opportunities resulted in 312 actual target shots, involving 19 principal investigators (including several shots with collaborators from SNL and LANL). The mini-campaigns are listed in Table 88.XI.

Highlights of LLNL and NWET experiments in FY01 include the following:

Laser–Plasma Interactions: Energy transfer between beams was observed in the forward-scatter geometry and for a range of beam and plasma conditions that are similar to those expected in the NIF. In some cases, the beam energy was enhanced by as much as a factor of 2. This has the potential for creating a symmetry problem for NIF indirect-drive capsules. Substantial energy transfer was observed even at 1/5 the nominal NIF intensity. This indicates that large beams alone may not solve the symmetry problem for indirect-drive capsules. The OMEGA data will motivate an investigation of the energy transfer issue for a variety of possible NIF target/beam configurations in order to select the optimum configuration.

Cocktail Hohlraums: Experiments to investigate the potential of "cocktail" hohlraum materials to increase soft x-ray emission (and therefore increase the energy coupling to the capsule) in NIF hohlraums were continued. In FY01, Scale 3 hohlraums with a splitback plate (see Fig. 88.52) indicated that the soft x-ray emission of the cocktail material at a photon energy of 260 eV is only 15% enhanced over the case of a conventional hohlraum made only of Au (see Fig. 88.52). In addition, Scale 3/4 and Scale 1 cocktail hohlraums gave the same spectrally integrated drive as gold hohlraums, whereas a 5% increase in T_r was expected. This unexpected observation may be due to lower laser to x-ray conversion efficiency for cocktail hohlraums compared to the standard Au hohlraums. A potential fix to be tested in FY02 is to use Au-lined cocktail hohlraums such that the laser conversion to x rays still occurs in the top Au layer, while the reradiation energetics is dominated by the deeper cocktail layer.

High-Convergence Implosions: The multicone capability of OMEGA continued to be of use in conducting cylindrical-hohlraum capsule implosions with convergence ratios as high as 20. In FY01 HEP5 experiments, the improvement in performance over Nova experiments with similar targets was ascribed to better time-dependent symmetry control and the use of Ar dopant-free fuel (see Fig. 88.53). Experiments with intentionally roughened surfaces demonstrated that the degradation was caused by hydro-instability growth and followed simulation results (see Fig. 88.54).

Table 88.XI: FY01 LLNL and NWET Campaigns.

Campaign	Sub-Element	Experiment	Target Shot Allocation
Target Ignition Physics (TIP)	WBS-1: Energetics	Absolute albedo	5
		Laser–plasma interactions	10
		Cocktail holhraum	10
	WBS 2: Symmetry	NIF foot symmetry	10
		High-convergence implosions	20
	WBS 3: Ablator Physics	Shock timing	20
		Ablator burnthrough	5
		Convergent ablator burnthrough	10
		Planar RT	10
		X-ray Thomson scattering	5
	WBS 4: Diagnostics	Ignition diagnostics	5
High-Energy-Density Sciences		Solid-State Hydro	20
	Implosion Mix	Pushered shells	10
	Hydro I	Richtmyer–Meshkov	20
	Hydro II	Features	15
	Hydro III	Jets	15
	Implosions	NBI	5
	Radiation Transport	RadG	20
	Equation of State (EOS)	Low- and High-Z	35
		X-ray Thomson scattering	5
	Opacity	Hot holhraum	10
		NLTE	5
	Capability Development	X-ray Thomson scattering	10
		Backlighter development	5
		Slit closure	5
		Dual color	10
NWET	Source Development	Gas-filled sources	10
		Hot-electron sources	5
		Spheres	5
		TOTAL	320

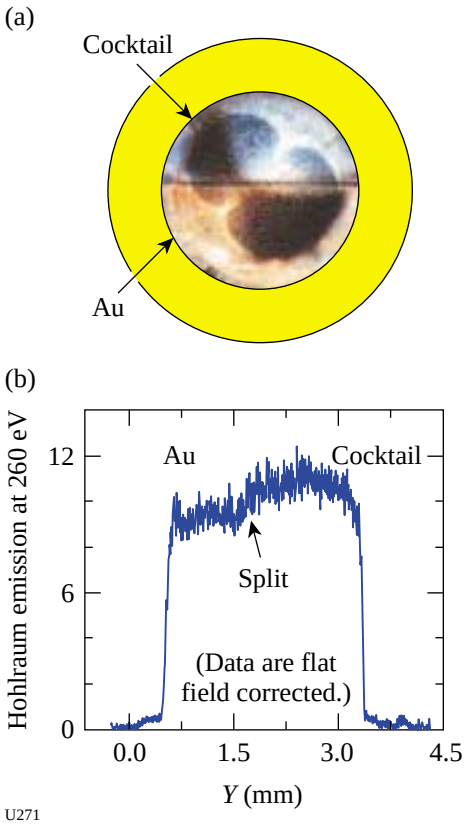

Figure 88.52
(a) Schematic of the hohlraum configuration used to conduct cocktail material experiments. A split backplate (half cocktail/half Au) is used in a Scale 3 hohlraum. (b) Soft x-ray emission at 260 eV is spatially resolved and shows an ~15% increase in cocktail soft x-ray emission compared to the Au side. This increase is lower than that predicted by *LASNEX* simulations.

NIF-Relevant Hohlraum Symmetry: Investigation of the symmetry of NIF-relevant (WBS 2) hohlraums continued. A configuration for these experiments is shown in Fig. 88.55(a). Thin-shell implosions were imaged with 4.7-keV x rays and yielded symmetry data showing that the asymmetries are small and in agreement with 2-D simulations [see Fig. 88.55(b)].

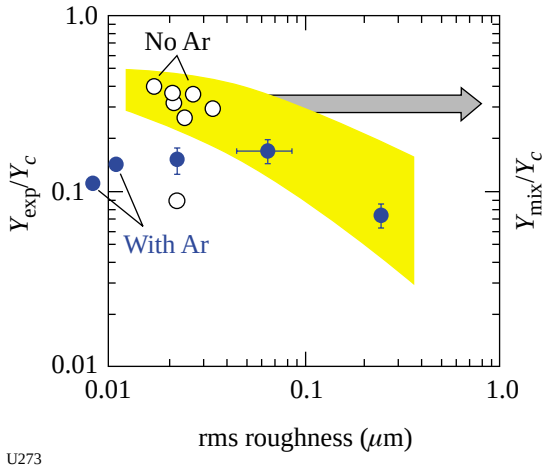

Figure 88.54
Plot of the ratio of measured neutron yield over that calculated for 1-D clean implosions as a function of measured target roughness. The cases shown are for convergence ratio ~ 20, indirect-drive implosions carried out on OMEGA. The capsules were intentionally roughened to carry out this experiment. The results are compared to simulations (yellow band) showing the ratio of the neutron yield for an implosion with mix to that of clean 1-D implosions.

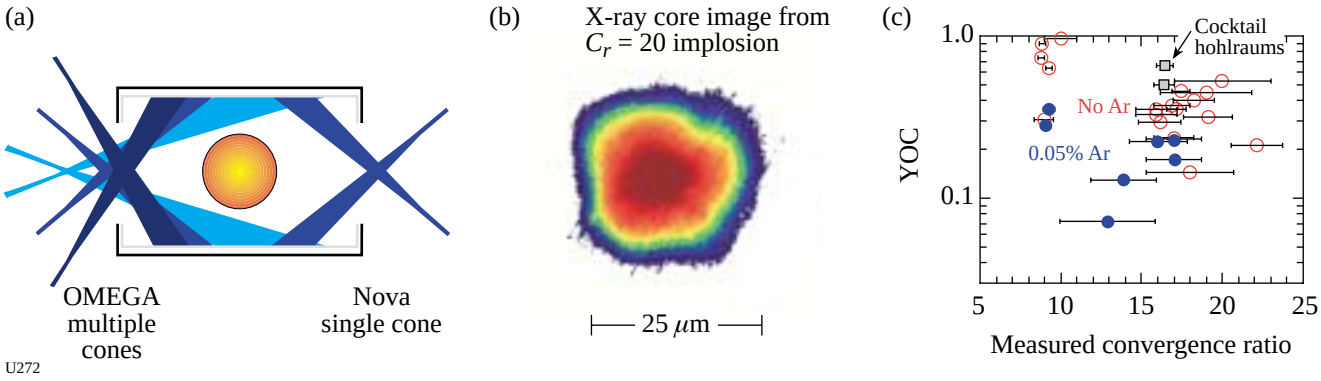

Figure 88.53
(a) Schematic showing the difference between the Nova single-cone hohlraum geometry and that of OMEGA with multiple cones. (b) Typical x-ray image of OMEGA implosion shows symmetric implosion for capsules with convergence ratio ~ 20. (c) Plot of the ratio of actual neutron yield divided by the calculated 1-D clean yield (YOC) as a function of measured convergence ratio. The improvement in performance of the OMEGA experiments (open circles) over Nova implosions (solid circles) is ascribed to better time-dependent symmetry control and the use of dopant-free fuel.

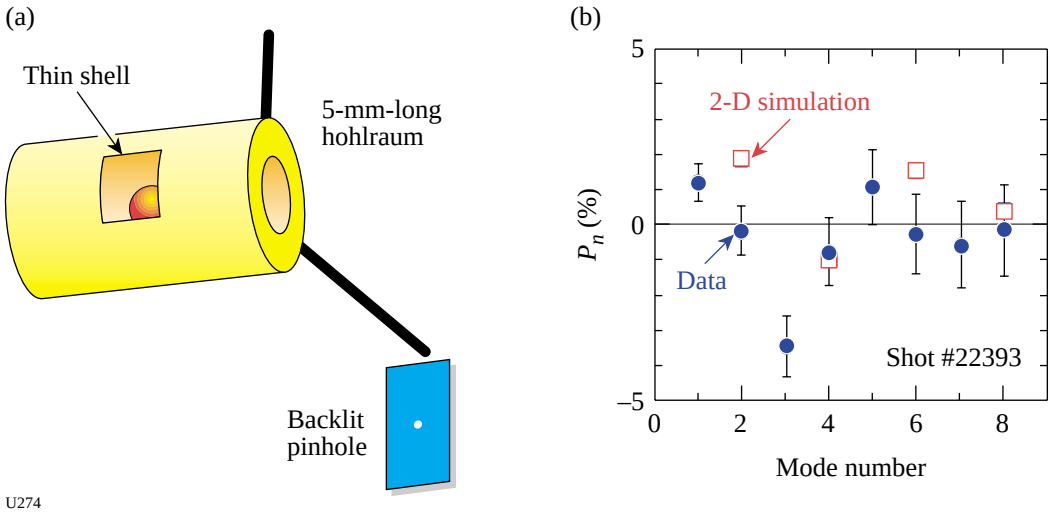

Figure 88.55
Schematic of experimental geometry for OMEGA symmetry experiments. A thin spherical target is imploded inside a 5-mm-long cylindrical hohlraum (a). A point source backlighter provides high-resolution x-ray radiographic images. The resulting data are plotted in (b) showing the inferred asymmetries decomposed in Legendre moments P_n. The open square data points are the results of a 2-D simulation of the asymmetry while the solid circles are the experimental results.

X-Ray Thomson Scattering: The first demonstration of x-ray Thomson scattering as a high-density temperature and density diagnostic was carried out on OMEGA during FY01. The experimental configuration is shown in Fig. 88.56(a). Initial results from these experiments are shown in Fig. 88.56(b).

Planar Rayleigh–Taylor Experiments: Polyimide ablator Rayleigh–Taylor (PIRT) experiments continued on radiation-driven targets in FY01. Experiments conducted with 30-, 50-, and 70-μm-wavelength perturbations showed that the RT growth rate with small initial amplitudes was somewhat greater than originally predicted and occurred somewhat earlier (see Fig. 88.57). In addition, as expected, growth in cocktail hohlraums was larger than in Au hohlraums due to the presence of less-than-2-keV preheat.

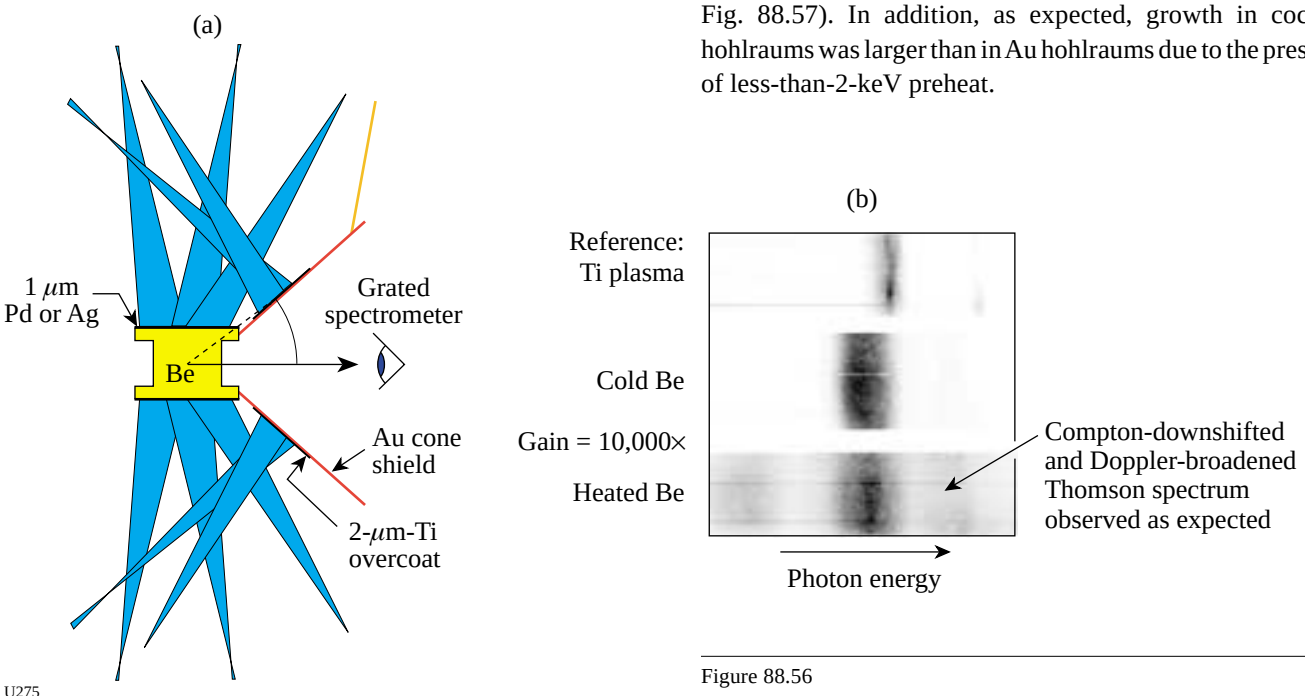

Figure 88.56
(a) Schematic of x-ray Thomson scattering experiment. (b) Experimental results from x-ray Thomson scattering experiment.

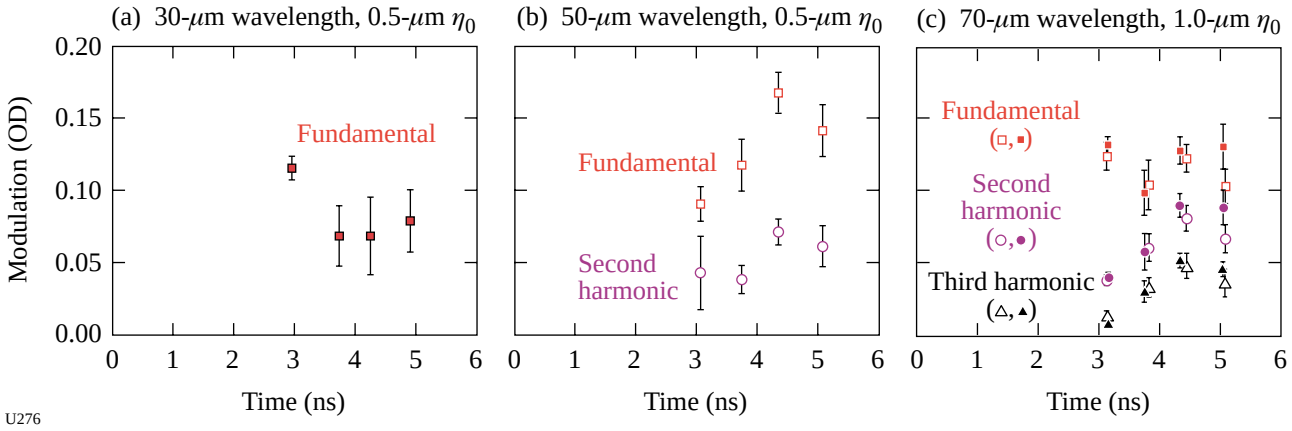

Figure 88.57
Summary of RT growth data from PIRT experiments with Au (open data points) and cocktail (solid points) hohlraums. More growth is evident in cocktail hohlraums than in Au hohlraums. Future shots will attempt to reproduce these results and expand the database.

Shock Timing: A collaboration including scientists from SNL, LANL, and LLNL conducted experiments to investigate shock timing in radiation-driven ablators. A half-hohlraum (halfraum) target was used for these experiments. One configuration featured stepped or wedged ablators attached to a halfraum and interrogated with a LANL streaked optical pyrometer (SOP) as shown in Fig. 88.58. Experiments were also conducted using flat ablator samples and an imaging configuration x-ray streak camera. Initial data with a 160-eV halfraum with Be + 0.9% Cu and polyimide ablators showed that the shock timing could be predicted to within ~ 200 ps (see Fig. 88.59).

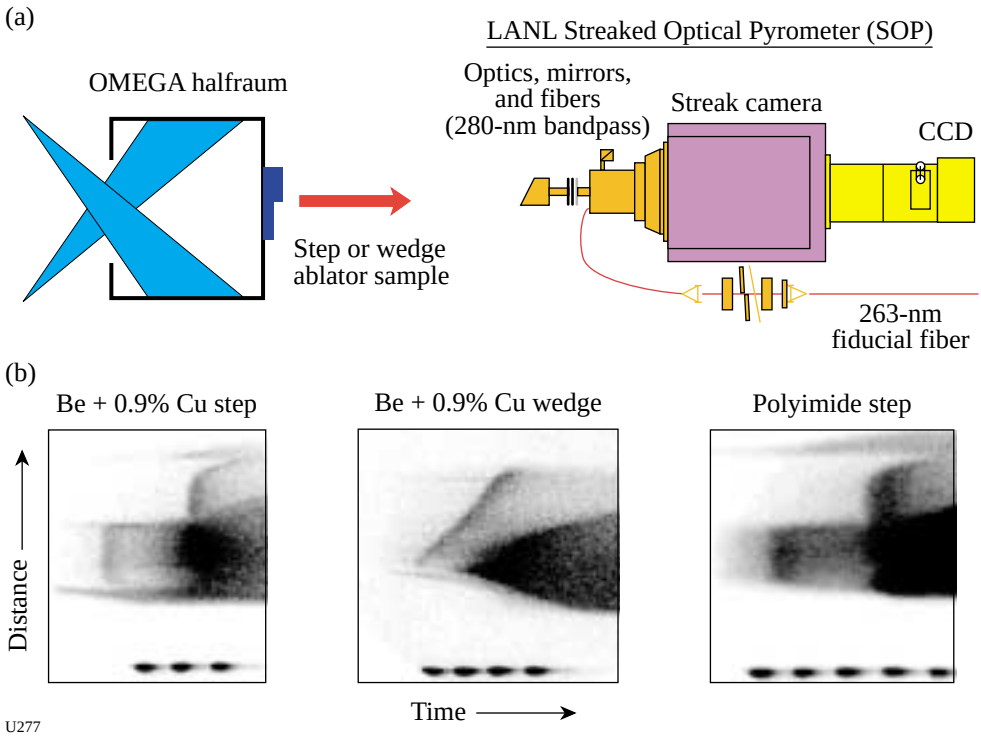

Figure 88.58
(a) Schematic of shock-timing experiments and (b) streak camera data from three configurations: Be + 0.9% Cu step; Be + 0.9% Cu wedge; and a polyimide step. The streak photographs have the time axis on the bottom (note temporal fiducial) and the space coordinate on the vertical axis.

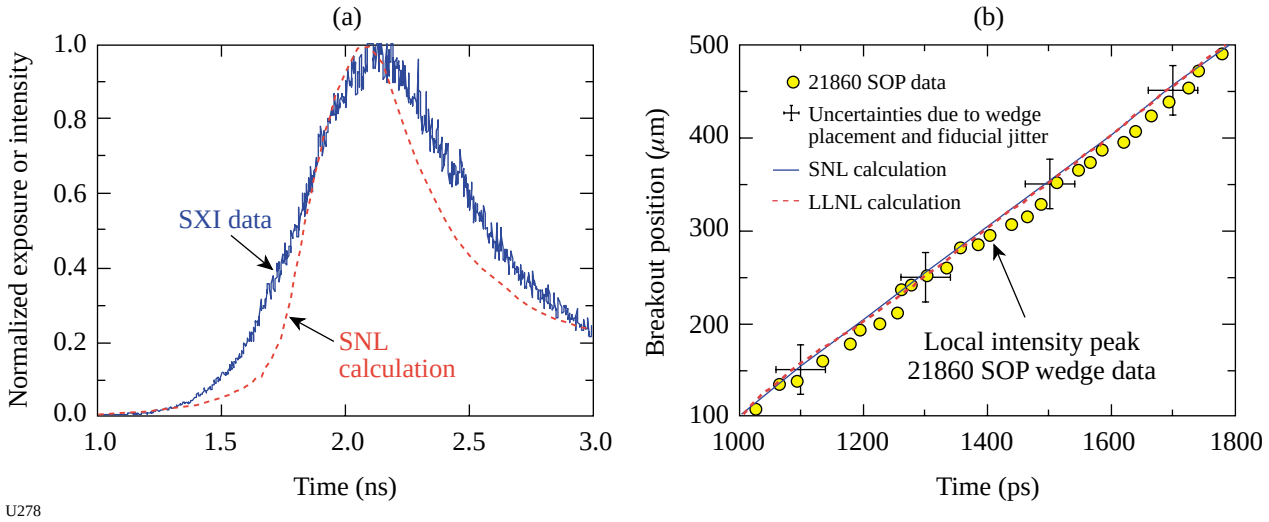

Figure 88.59
Comparison of experimental shock breakout data with SNL and LLNL calculations. (a) Ablation-front burnthrough data and comparison to SNL simulations for planar polyimide sample. (b) Shock-breakout measurements and comparison to SNL (solid line) and LLNL (dashed line) simulations for Be + 0.9% Cu wedge.

Ignition Diagnostics: A new diagnostic for measurement of the ablator areal density (ABRHOR) was tested on OMEGA. ABRHOR is designed to measure spatial variations in shell ρR and/or temperature as an indication of shell breakup and burnthrough. The technique relies on a mid-Z dopant in the ablator. Multiple monochromatic images across an x-ray energy band containing spectral features from the dopant can provide the required data. In FY01, experiments were conducted on OMEGA to test a conceptual design of this instrument based on multiple pinhole imaging off a crystal. [This is similar to an LLE-developed technique (see Fig. 88.60)]. The OMEGA test was conducted on Ti-doped CH pushers in indirect-drive implosions that were back-illuminated by the core x-ray continuum. Good data were obtained (see Fig. 88.61) from several shots with different drive and capsule parameters. The relatively poor quality of the graphite crystals used in this initial test complicated quantitative analysis. Future experiments will use a multilayer mirror to improve the quality of the data.

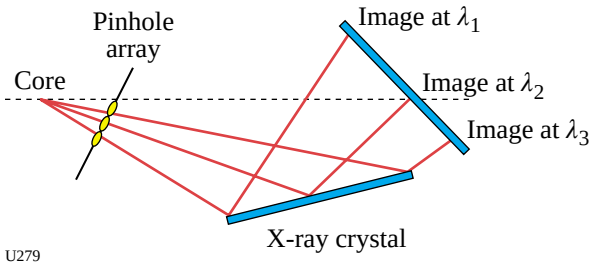

Figure 88.60
Schematic of ABRHOR diagnostic. Multiple monochromatic images are obtained across an x-ray energy band containing spectral features from the dopant.

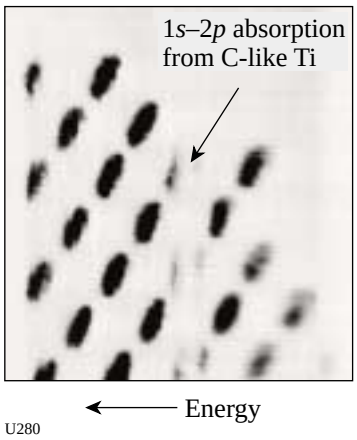

Figure 88.61
Proof-of-principle data from ABRHOR diagnostic. Multiple images of Ti-doped CH pushers are back-illuminated by the self-emission from the core continuum radiation.

IDrive: During FY01, LLNL initiated a series of experiments on OMEGA to test a new laser-driven, high-pressure source (IDrive). The new design (shown in conceptual form in Fig. 88.62) creates a plasma piston that can generate a shockless, continuously loaded high-pressure wave in a flat target. Initial efforts in July 2001 demonstrated that the concept functions as designed. Very low laser energies (less than 30 J/beam) have produced flyer velocities in excess of 12 km/s and shockless pressure waves up to 0.5 Mbar. Figure 88.63 shows the results from some of the early experiments.

High-Z and Low-Z Equation-of-State (EOS) Experiments: During FY01, significant progress was made on EOS experiments for both high-*Z* and low-*Z* matter. Hugoniot data were obtained on diamond and water; the shock metalization thresholds were identified for water, diamond, LiF, and sap-

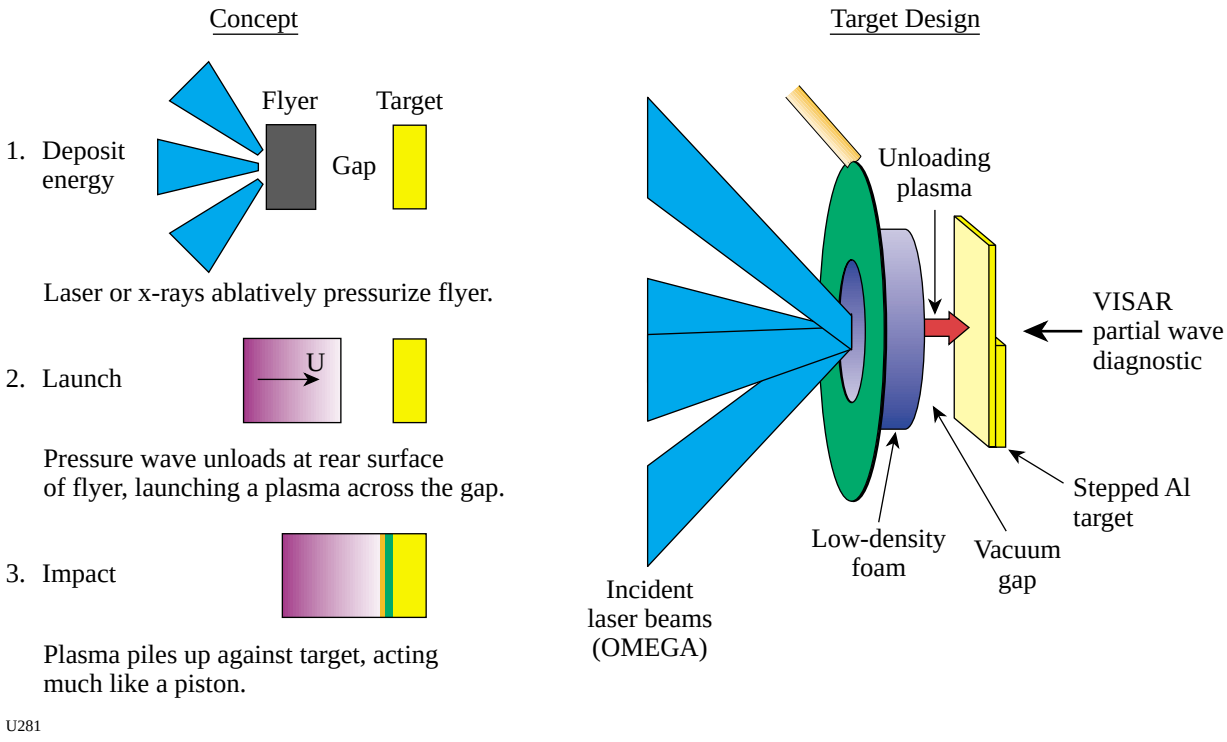

Figure 88.62
Schematic illustrating the IDrive shockless drive technique and a sketch of the target design for the IDrive experiments.

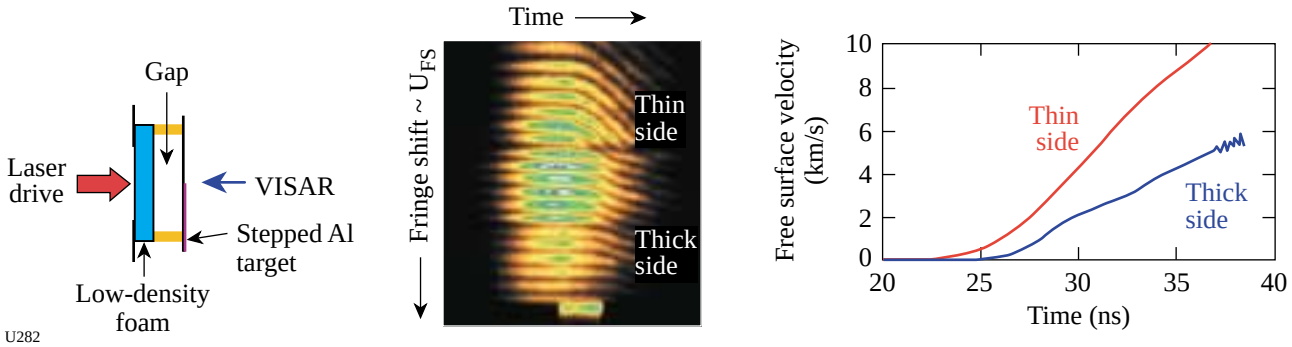

Figure 88.63
Initial results from the IDrive experiments show the presence of a shockless pressure wave in aluminum.

phire; the shock-melting transition in diamond was accurately identified; accurate double-shock experiments were carried out on water using the transparent anvil technique; and initial experiments were carried out to determine shock-induced melting in metals. In addition, the ASBO diagnostic system (the workhorse of EOS experiments) was upgraded to dual-VISAR capability.

Direct-Drive Richtmeyer–Meshkov (RM) Instability Experiments: In FY01 a series of direct-drive RM experiments were carried out on planar targets with initial perturbation amplitudes of 22 μm and 7 μm and a perturbation wavelength of 150 μm. The experimental data were compared (see Fig. 88.64) with simulations using linear (Meyer–Blewitt) and nonlinear (Sadot) models that do not include shock proximity. In both cases, the models over-predicted the amplitude growth.

Supersonic Jet Experiments: Collaborative experiments among AWE (United Kingdom), LANL, and LLNL continued to investigate the interaction of a supersonic jet with a counter-propagating shock. During FY01, these experiments provided high-quality benchmark data for comparison to the CAL (LLNL), RAGE (LANL), and NYM-PETRA (AWE) hydrocodes (see Fig. 88.65).

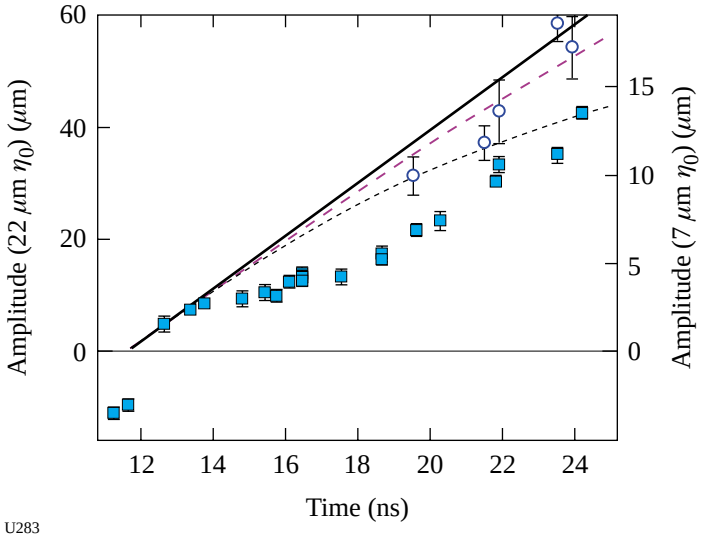

U283

Figure 88.64
Results of RM/Hydro experiments and comparison to theoretical calculations for linear (Meyer–Blewitt) and nonlinear (Sadot) theories.

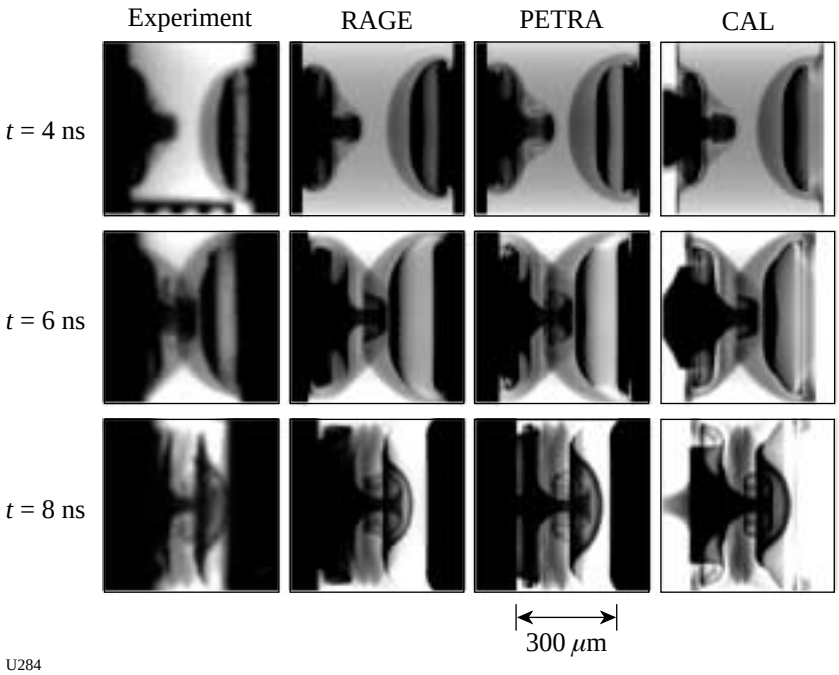

U284

Figure 88.65
Comparison of supersonic jet experiments with various multidimensional computer simulations. The jet and shock are generated in two opposed halfraums. The images are created by x-ray backlighting of the interaction region.

Nonideal Backlit Implosions (NIBI): During FY01, experiments were initiated to investigate the effects of nonuniform illumination on direct-drive capsule implosions. A subset of OMEGA beams was used to implode a capsule while the remaining beams were used to produce x rays from a Fe target to backlight the imploding target. Figure 88.66 shows the results from a near-uniform illumination experiment (shot 23543) and from an implosion with imposed asymmetry in the capsule irradiation (shot 23544).

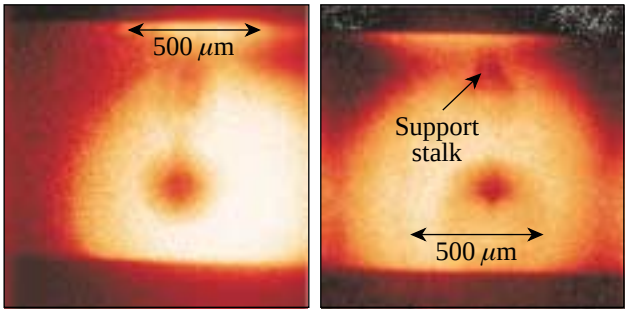

Figure 88.66
X-ray backlit images (Fe backlighter) from near-symmetric (shot 23543) and nonuniform illumination (shot 23544) of low-convergence implosions.

Slit Closure: One of the capability development programs carried out in FY01 involved the investigation of slit and pinhole closure by soft x rays. Figure 88.67 shows the experimental configuration and data obtained on two of these experiments. In this case, a Ti backlighter foil was irradiated by some of the OMEGA beams, and the transmission of the resulting x rays through a slit was measured with a streak camera. The graph compares the x-ray transmission through the slit as a function of time when a Be foil is placed between the Ti foil and the pinhole and when no foil is used. The Be foil is designed to block soft x rays from the Ti from irradiating the pinhole. No difference in transmission between these two cases is observed, implying that soft x rays are not the predominant mechanism for inducing slit or pinhole closure in such configurations. Future shots will investigate the effect of slit tamping on the closure.

Gas-Filled Sources: Experiments continued under the NWET program to develop the efficient x-ray sources to be used as

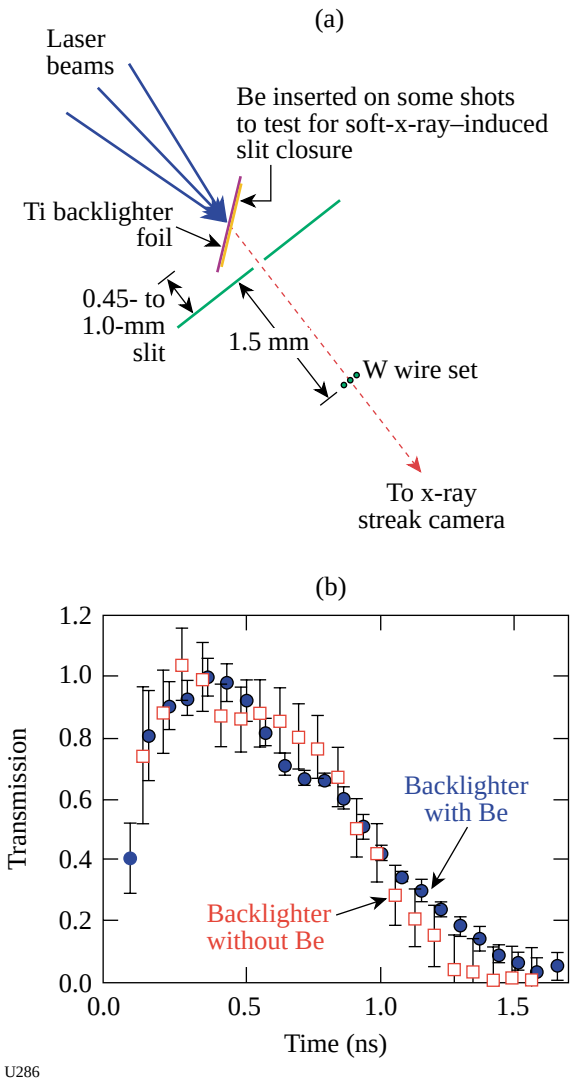

Figure 88.67
(a) Schematic of slit closure experiment and (b) results of transmission measurements.

backlighters for high-ρR and high-Z applications. During FY01, Kr K-shell emission was added to the list of efficient underdense multi-keV emitters. The experimental configuration (a Kr-filled CH cylinder) and a summary of the x-ray conversion results for emitters with energy in the range of 2 to 13 keV are shown in Fig. 88.68. The latest Kr gas experiments produced ~0.3% conversion in the ~13-keV Kr K-shell emission.

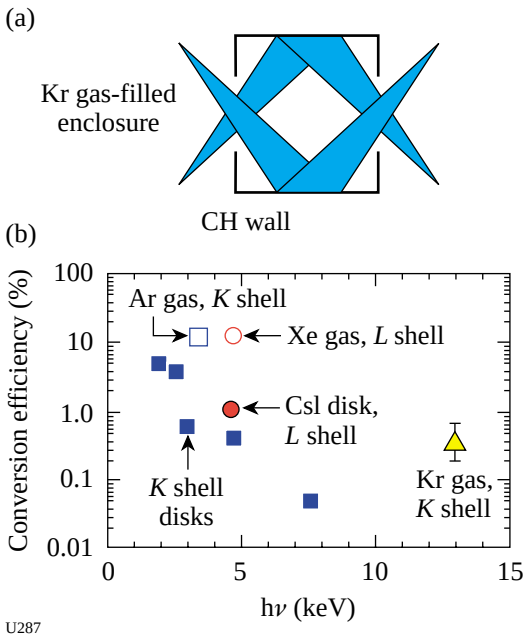

Figure 88.68
(a) Schematic of gas-filled can radiation source experiments. (b) Results of conversion efficiency measurements for a series of gases and disks.

2. Los Alamos National Laboratory Campaigns

In FY01 LANL performed five campaigns on OMEGA. This work has been documented in the form of pre- and postshot reports:

a. LANL ID01-1: Double shells in cylindrical hohlraums and ACE-A and ACE-B
   – Preshot report LA-UR-00-5574
   – Double-shell postshot report LA-UR-01-0432
   – ACE-A postshot report LA-UR-01-1426
   – ACE-B postshot report LA-UR-01-5433

b. DDCYL 01-1: Direct-drive cylinders
   – Preshot report LA-UR-01-0953
   – DDCYL postshot report LA-UR-01-5511

c. LANL ID01-2: X-ray backlighter development and ACE
   – Preshot report LA-UR-01-1659
   – ACE-A postshot report LA-UR-01-5559

d. LANL ID01-3: High-yield nuclear diagnostic development and ACE
   – Preshot report LA-UR-01-4381
   – ACE-A postshot report LA-UR-01-5560
   – High-yield postshot report
   – Direct-drive double shells (DDCYL 01-2 cancelled because of the 9/11 events)
   – Preshot report LA-UR-01-5202

Double-Shell Capsules: Work continued on double-shell capsules as an alternative for ignition on the NIF. Previously, good results (high measured neutron yield relative to 1-D clean calculations) had been obtained in spherical hohlraums (a.k.a. "tetrahedral hohlraums," referring to the locations of the laser entrance holes) with excellent irradiation symmetry. Representative capsules were shot on OMEGA to confirm that similar good results could be obtained with NIF-relevant symmetry in cylindrical hohlraums. Good results were obtained with deuterium-filled capsules, showing that drive symmetry was not the principal issue of performance for these capsules (see Fig. 88.69). Subsequently, larger capsules were shot using direct-drive illumination that would remove any

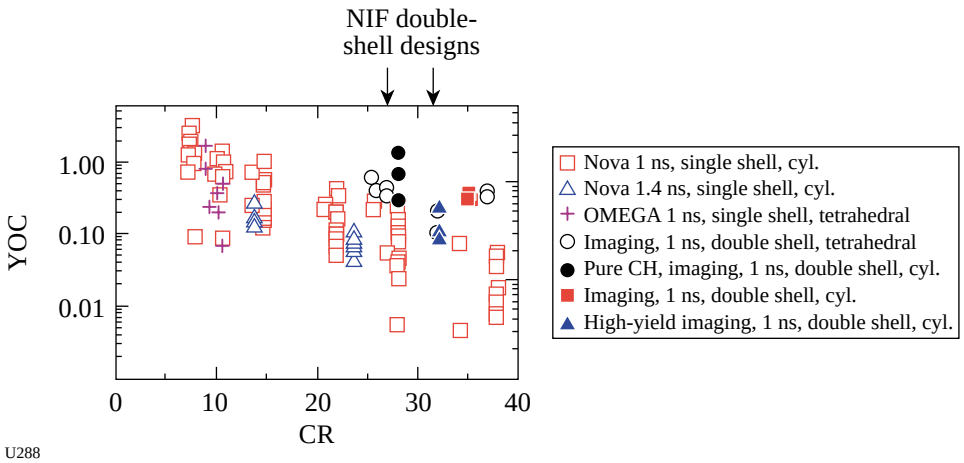

Figure 88.69
Measured neutron yield divided by 1-D, clean calculated yield (YOC) versus convergence ratio (CR) for all OMEGA imaging and pure-CH imaging shots to date, in tetrahedral and NIF-style cylindrical hohlraums. The data for the NIF-style hohlraums is shown as solid points, while the tetrahedral results are shown as circles or open crosses. In the legend, "cyl" is a cylindrical hohlraum.

M-band asymmetries due to laser spots in the hohlraums. Poor results were obtained in this series. The issues of target fabrication, mix, and direct-drive physics are being investigated to understand the later results.

X-Ray Backlighting Sources: The development of x-ray backlighting sources and the optimization of x-ray conversion efficiency for these sources are important for the design of future NIF experiments. Various mid-*Z* elements and a variety of spot sizes and intensities of 3ω light have been investigated on OMEGA experiments. Data showing the dependence of conversion efficiency on spot size at similar irradiance have been obtained (Fig. 88.70). The peak x-ray conversion as a function of intensity has been identified for different configurations.

ACE Experiments: The ACE experiments successfully obtained data for the high-energy-density support of the Stockpile Systems Program. Some experiments featured an innovative backlighter system that provides very bright emission and is flat in intensity across the field of view (illustrated in Fig. 88.71).

Direct-Drive Cylindrical Implosions: Direct-drive cylinder work continued in two campaigns. The ablative RT work evaluated target fabrication and image quality to achieve quantitative data for comparison to hydrocode predictions. Figure 88.72 shows imaging x-ray streak camera data from such a cylindrical implosion with a ramp drive pulse. Just before the end of the 2.5-ns linear ramp, the chlorine in the

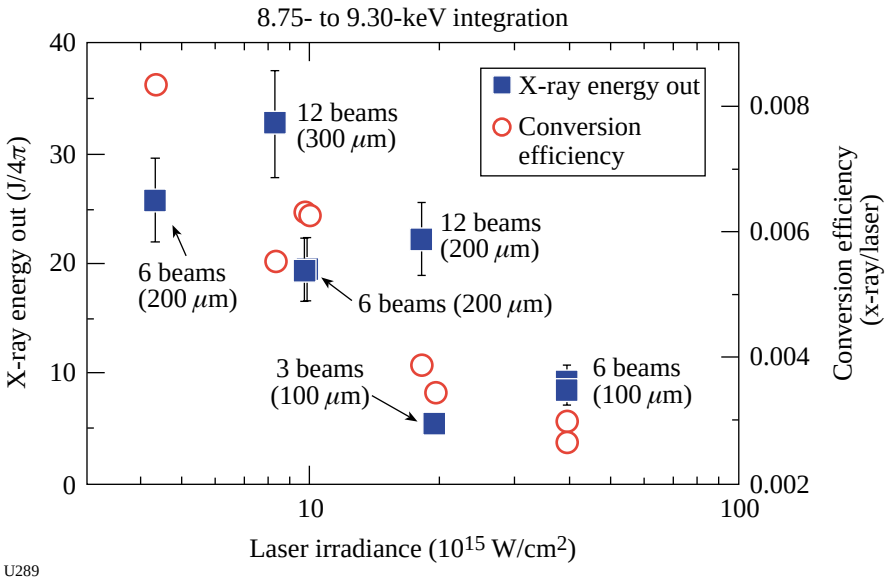

Figure 88.70
Plot of measured x-ray energy in He-α lines of Zn taken using a time-integrated Henway spectrometer versus laser irradiance from overlapped beams with indicated spot size.

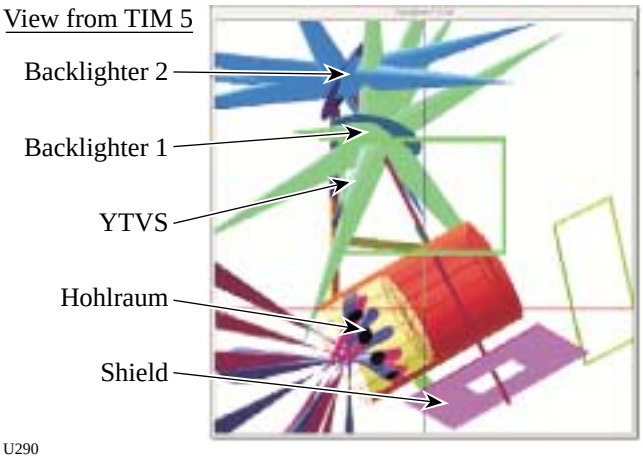

Figure 88.71
The ACE-B geometry with two backlighters irradiated by 17 beams to carry out radiography of a halfraum with 12 drive beams.

marker layer burns through due to the formation of spikes by the action of the RT instability. Unfortunately, it has been decided that, at present, targets with sufficiently small and controlled surface roughness cannot be fabricated to quantitatively address the relevant physics of this experiment so this campaign has been stopped. The direct-drive cylinder mix program has made significant success in demonstrating measurable mix in a convergent, compressible plasma experiment. Thick (60- to 73-μm) ablators separate the direct-drive laser absorption region from the "pure" hydrodynamic marker. Detailed calculations are being made to model this data using a number of codes, including the *RAGE* adaptive mesh refinement code at Los Alamos illustrated in Fig. 88.73. This year mix-width data (Fig. 88.74) were taken at different times during the implosion and compared to the *RAGE* simulations.

NIF Diagnostics: Los Alamos continues to develop Phase 2 fusion product diagnostics for the NIF, including both the Gas Cerenkov gamma-ray burn history diagnostic and pinhole-aperture neutron imaging. The Gas Cerenkov System obtained definite evidence for the DT fusion gamma on OMEGA. The neutron imaging system, in collaboration with CEA and LLE, obtained images for the first time.

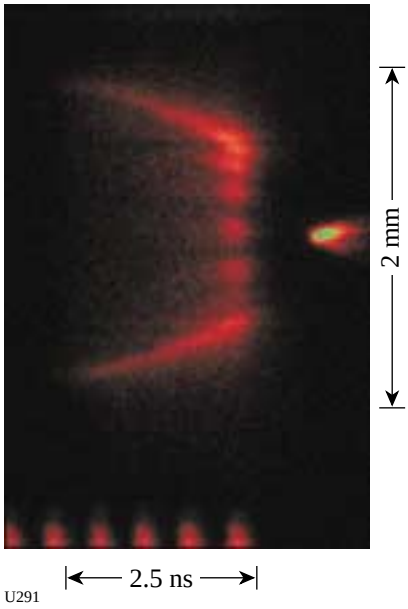

Figure 88.72
Imaging x-ray streak camera (IXRSC) image from shot 22622 showing intensity transversely across the cylinder (up–down) versus time (left–right). The ablation surface implodes, with the spikes of the original m = 14 perturbation burning through just before the end of the 2.5-ns linear ramp laser drive. Subsequently, the core of the cylinder implodes and lights up in self-emission.

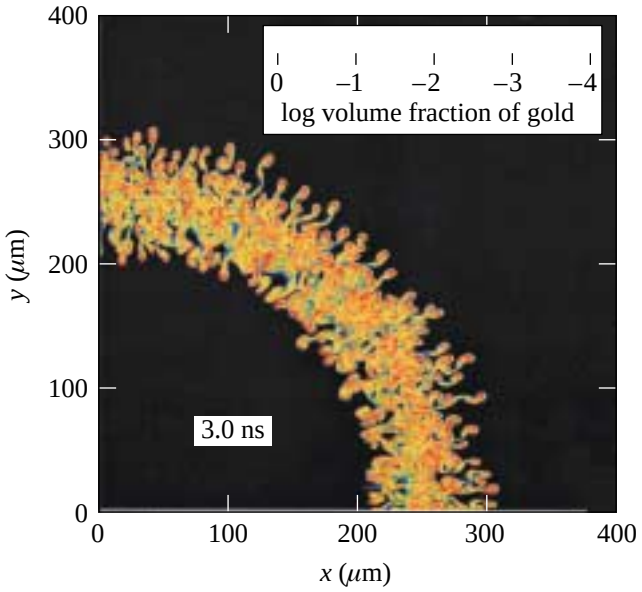

Figure 88.73
RAGE simulation of the volume fraction of a gold marker in an r-θ calculation at 3.0 ns into a direct-drive cylindrical mix implosion.

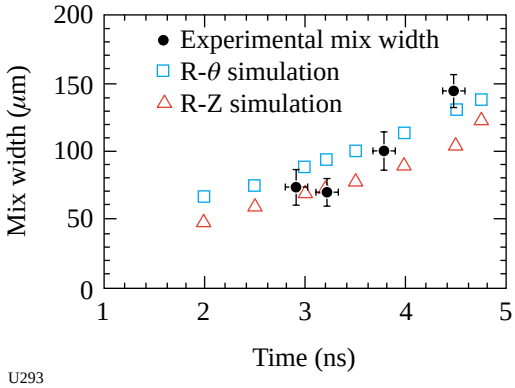

Figure 88.74
Comparison of experimental measurements of rough gold marker mix width in time with *RAGE* simulations.

3. CEA Experiments

CEA scientists participated in several OMEGA experiments during FY01 including neutron imaging development and evaluation and measurement of gamma yields on OMEGA.

Imaging of the neutrons produced by implosions on the NIF and the LMJ will require spatial resolution as great as 5 μm to distinguish failure mechanisms such as poor implosion symmetry or improper laser pulse shaping. Coded imaging, either by penumbral or annular aperture, will be used to achieve high resolution and good sensitivity.[2] In FY00, CEA implemented a neutron imaging system (NIS) on OMEGA based on penumbral imaging using a biconical aperture. Using NIS, the neutron burn regions of imploded DT-filled glass microballons with 2.5- and 4.2-μm-thick walls were imaged and produced images with FWHM's of 78 and 62 μm, recorded with a resolution of 60 and 45 μm, respectively.[3]

This year (FY01), a spatial resolution of 20 μm was attained on implosions of CH and glass targets. The smallest features observed on the implosion of 15-atm-DT-filled CH capsule implosions were ~30 μm.

To improve the NIS resolution, LLE drilled a hole in the concrete floor of the Target Bay, allowing a 13-m line of sight and a 1.6-m concrete shield for the NIS CCD detector (Fig. 88.75).

In parallel, a new neutron detector with 250-μm pixels was installed. This detector is made by filling an array of 160,000 capillaries[4] with a high-optical-index liquid scintillator. The optical-index step between the glass (1.49) and the liquid (1.58) traps the scintillation light produced by the slowing down of the recoil protons scattered by the 14-MeV neutrons. Both the pixel size and the transverse range of the recoil protons limit the neutron detector's spatial resolution to 1.1 mm. With a biconical aperture with a 200-μm field of view placed at 160 mm from target center, the ultimate resolution of NIS is now 17-μm FWHM.

Direct-drive implosions of DT-filled glass targets and CH targets were conducted during the experimental campaign. A typical unfolded neutron image from a CH target implosion (shot 23445) is shown in Fig. 88.76. The target in this case was a 932-μm-diam, 18.9-μm-thick CH shell filled with 15 atm of DT and produced a yield of 2×10^{13}.

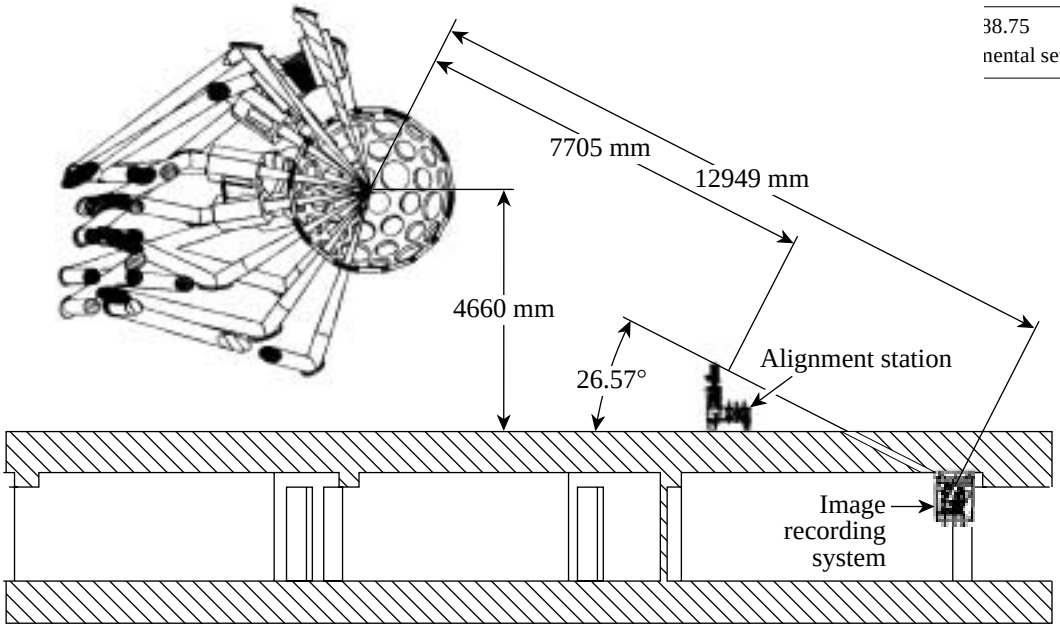

U294

38.75
nental setup of the neutron imaging system.

A new neutron detector is now being constructed. The scintillator will be loaded with deuterium to reduce the range of the recoil protons. The expected resolution of the new **detector** will be less than 0.5 mm. In parallel with the construction of the new detector, a thin annular aperture is under development. The first attempt will be made with a 5-cm-thick, 0.66-mm-diam cylinder of tungsten. This effort should lead to high-resolution neutron imaging at a low (~10^{12}) level of neutron production.

REFERENCES

1. C. A. Iglesias and S. J. Rose, Astrophys. J. Lett. **466**, L115 (1996); F. J. Rogers, B. G. Wilson, and C. A. Iglesias, Phys. Rev. A, Gen. Phys. **38**, 5007 (1988).
2. R. A. Lerche *et al.*, Laser Part. Beams **9**, 99 (1991).
3. L. Disdier, A. Rouyer, A. Fedotoff, V. Yu. Glebov, C. Stoeckl, and F. J. Marshall, "Neutron Prenumbral Imaging at OMEGA," submitted to Nuclear Instruments & Methods in Physics Research, Section A; Laboratory for Laser Energetics LLE Review **86**, 74, NTIS document No. DOE/SF/19460-393 (2001). Copies may be obtained from the National Technical Information Service, Springfield, VA 22161.
4. P. Annis *et al.*, Nucl. Instrum. Methods Phys. Res. A **367**, 377 (1995).

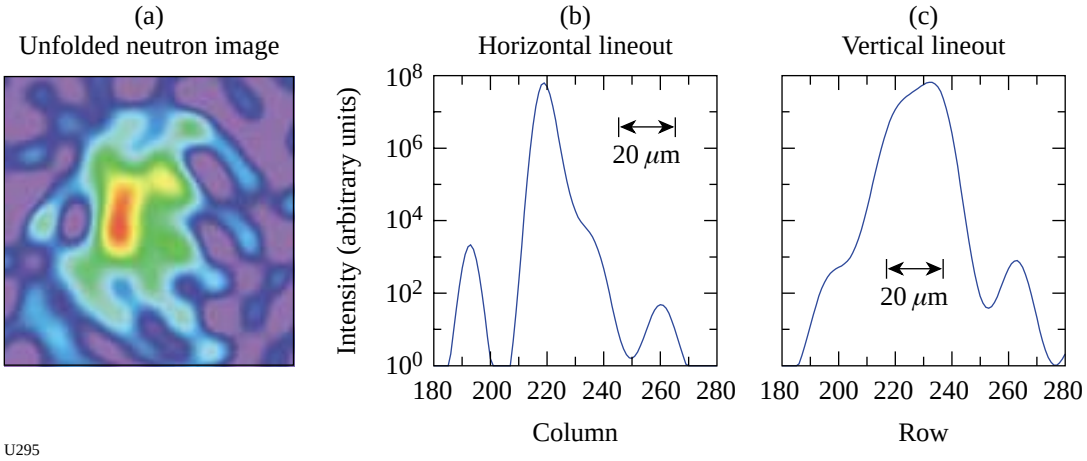

Figure 88.76
(a) Neutron image (200 × 200 μm^2) on shot 23445; (b) horizontal and (c) vertical profiles (43-μm and 75-μm FWHM, respectively). The arrows represent 20 μm in the target plane.

Publications and Conference Presentations

Publications

T. R. Boehly, J. A. Delettrez, J. P. Knauer, D. D. Meyerhofer, B. Yaakobi, R. P. J. Town, and D. Hoarty, "Effect of Shock Heating on the Stability of Laser-Driven Targets," Phys. Rev. Lett. **87**, 145003 (2001).

A. E. Marino, S. R. Arrasmith, L. L. Gregg, S. D. Jacobs, G. Chen, and Y. Duc, "Durable Phosphate Glasses with Lower Transition Temperatures," J. Non-Cryst. Solids **289**, 37 (2001).

A. V. Okishev, R. Boni, M. Millecchia, P. A. Jaanimagi, W. R. Donaldson, R. L. Keck, W. Seka, K. V. Dukelsky, M. A. Eronyan, V. S. Shevandin, G. M. Ermolaeva, G. E. Nikolaev, and V. B. Shilov, "Unique High-Bandwidth UV Fiber Delivery System for the OMEGA Diagnostics Applications," IEEE J. Sel. Top. Quantum Electron. **7**, 471 (2001).

V. A. Smalyuk, V. N. Goncharov, B. Yaakobi, J. A. Delettrez, F. J. Marshall, D. D. Meyerhofer, and S. P. Regan, "Evolution of Shell Nonuniformities Near Peak Compression of a Spherical Implosion," Phys. Rev. Lett. **87**, 155002 (2001).

Forthcoming Publications

A. Babushkin, M. J. Harvey, and M. D. Skeldon, "The Output Signal-to-Noise Ratio of a Nd:YLF Regenerative Amplifier," to be published in Applied Optics.

R. Betti and J. P. Freidberg, "Low-β, Magnetohydrodynamic Tokamak Equilibria with Poloidal Transonic Flow," to be published in Physical Review Letters.

B. Buerke and D. D. Meyerhofer, "Accurate Measurement of Hydrogenic Tunneling Rates in a High-Intensity Laser Focus," to be published in Physical Review Letters.

T. J. B. Collins and S. Skupsky, "Imprint Reduction Using an Intensity Spike in OMEGA Cryogenic Targets," to be published in Physics of Plasmas.

W. R. Donaldson, J. H. Kelly, R. L. Keck, and R. Boni, "Predicting and Measuring Optical Pulse Shapes on the OMEGA Laser System," to be published in the OSA Technical Digest.

F. Y. Fan, S. W. Culligan, J. C. Mastrangelo, D. Katsis, and S. H. Chen, "Novel Glass-Forming Liquid Crystals. VI. High–Temperature Glassy Nematics," to be published in Chemical Materials.

J. A. Frenje, D. G. Hicks, C. K. Li, F. H. Séguin, R. D. Petrasso, K. Fletcher, H. Olliver, S. Padalino, S. Thompson, J. M. Soures, S. Roberts, C. Sorce, T. C. Sangster, and T. W. Phillips, "CR-39 Tract Detector Response to Charged Particles and Neutrons," to be published in the Review of Scientific Instruments.

M. J. Guardalben, L. Ning, N. Jain, D. J. Battaglia, and K. L. Marshall, "Experimental Comparison of a Liquid Crystal Point Diffraction Interferometer (LCPDI) and a Commercial Phase-Shifting Interferometer and Methods to Improve LCPDI Accuracy," to be published in Applied Optics.

O. A. Konoplev, Y. Fisher, and D. D. Meyerhofer, "Generation of a Picosecond Laser Pulse with an Intensity Contrast of Eleven Orders of Magnitude," to be published in Optics Letters.

V. Lobatchev and R. Betti, "Ablative Stabilization of the Deceleration-Phase Rayleigh–Taylor Instability," to be published in Physical Review Letters.

J. A. Marozas, "Self- and Cross-Phase Modulation of High-Intensity Laser Beams Emerging from a Diamond-Turned KDP Wedge," to be published in the Journal of the Optical Society of America B.

J. A. Marozas, S. P. Regan, J. H. Kelly, D. D. Meyerhofer, W. Seka, and S. Skupsky, "Laser Beam Smoothing Caused by the Small-Spatial-Scale β-Integral," to be published in the Journal of the Optical Society of America B.

J. A. Marozas, J. D. Zuegel, D. Jacobs-Perkins, and J. H. Kelly, "Angular Spectrum Representation of Pulsed Laser Beams with Two-Dimensional Smoothing by Spectral Dispersion," to be published in the Journal of the Optical Society of America B.

R. L. McCrory, R. E. Bahr, R. Betti, T. R. Boehly, T. J. B. Collins, R. S. Craxton, J. A. Delettrez, W. R. Donaldson, R. Epstein, J. Frenje, V. Yu. Glebov, V. N. Goncharov, O. V. Gotchev, R. Q. Gram, D. R. Harding, D. G. Hicks, P. A. Jaanimagi, R. L. Keck, J. H. Kelly, J. P. Knauer, C. K. Li, S. J. Loucks, L. D. Lund, F. J. Marshall, P. W. McKenty, D. D. Meyerhofer, S. F. B. Morse, R. D. Petrasso, P. B. Radha, S. P. Regan, S. Roberts, F. Séguin, W. Seka, S. Skupsky, V. A. Smalyuk, C. Sorce, J. M. Soures, C. Stoeckl, R. P. J. Town, M. D. Wittman, B. Yaakobi, and J. D. Zuegel, "OMEGA ICF Experiments and Preparation for Direct-Drive Ignition on NIF," to be published in the proceedings of the 18th IAEA Fusion Energy Conference.

F. H. Séguin, C. K. Li, D. G. Hicks, J. A. Frenje, R. D. Petrasso, J. M. Soures, V. Yu. Glebov, C. Stoeckl, P. B. Radha, D. D. Meyerhofer, S. Roberts, C. Sorce, T. C. Sangster, and M. D. Cable, "Diagnostic Use of Secondary D^3He Proton Spectra for D-D OMEGA Targets," to be published in Physics of Plasmas.

A. B. Shorey, S. D. Jacobs, W. I. Kordonski, and R. F. Gans, "Understanding the Mechanism of Glass Removal in Magnetorheological Finishing (MRF)," to be published in Applied Optics.

R. W. Short, "Stability of Self-Focused Filaments in Laser-Produced Plasmas," to be published in Physical Review Letters.

M. D. Skeldon, "An Optical-Pulse-Shaping System Based on an Electro-Optic Modulator Driven by an Aperture-Coupled-Stripline Electrical-Waveform Generator," to be published in Journal of the Optical Society of America B.

D. J. Smith, J. A. Warner, N. E. LeBarron, T. J. Kessler, and S. LaDelia, "The Development of Ion-Etched Phase Plates," to be published in Applied Optics.

E. A. Startsev and C. J. McKinstrie, "Relativistic Ponderomotive Dynamics of a Test Particle in a Plasma," to be published in Physical Review E.

F. Y. Tsai, E. L. Alfonso, S. H. Chen, and D. R. Harding, "Processing Vapor-Deposited Polymide," to be published in the Journal of Applied Physics.

B. Yaakobi, C. Stoeckl, T. Boehly, D. D. Meyerhofer, and W. Seka, "Measurement of Preheat due to Fast Electrons in Laser Implosions," to be published in SPIE's Proceedings of the XXVI European Conference on Laser Interaction with Matter.

J. D. Zuegel and D. W. Jacobs-Perkins, "An Efficient, High-Frequency Bulk Phase Modulator," to be published in Applied Optics.

J. D. Zuegel and S. A. Letzring, "Bulk Microwave Phase Modulators for Smoothing by Spectral Dispersion," to be published in Applied Optics.

Conference Presentations

G. Chen, Y. Du, A. Marino, L. L. Gregg, S. R. Arrasmith, and S. D. Jacobs, "Effect of SnO on Chemical Durability of Phosphate Glasses," The International Congress on Glass ICG 2001, Edinburgh, Scotland, 2–6 July 2001.

The following presentations were made at the 14th Target Fabrication Meeting, West Point, NY, 15–19 July 2001:

E. L. Alfonso, R. Q. Gram, and D. R. Harding, "CFD Modeling of Temperature/Pressure Gradients While Cooling Thin-Walled Direct-Drive Capsules."

R. Q. Gram and D. R. Harding, "Filling and Cooling Thin-Walled Cryogenic Targets."

L. D. Lund, D. R. Harding, D. J. Lonobile, D. Jacobs-Perkins, and T. Hinterman, "Alignment, Vibration, and Shroud Retraction: Initial Performance of the OMEGA Cryogenic Target Handling System."

P. W. McKenty, C. Stoeckl, V. N. Goncharov, M. J. Bonino, V. Yu. Glebov, D. R. Harding, D. D. Meyerhofer, and R. L. McCrory, "The Role of Improved Target Surface Roughness in Recent OMEGA Gas-Filled Implosion Experiments."

D. D. Meyerhofer, C. Chiritescu, T. J. B. Collins, J. A. Delettrez, R. Epstein, V. Yu. Glebov, D. R. Harding, R. L. Keck, S. J. Loucks, L. D. Lund, R. L. McCrory, P. W. McKenty, F. J. Marshall, S. F. B. Morse, S. P. Regan, P. B. Radha, S. Roberts, W. Seka, S. Skupsky, V. A. Smalyuk, C. Sorce, C. Stoeckl, J. M. Soures, R. P. J. Town, J. A. Frenje, C. K. Li, R. D. Petrasso, F. H. Séguin, K. Fletcher, C. Padalino, C. Freeman, N. Izumi, R. Lerche, T. W. Phillips, and T. C. Sangster, "Cryogenic-Target Experiments on OMEGA."

S. G. Noyes, M. J. Bonino, D. Turner, J. Tidu, and D. R. Harding, "Target Fabrication Techniques at LLE."

S. Skupsky, R. Betti, V. N. Goncharov, R. L. McCrory, P. W. McKenty, R. P. J. Town, D. D. Meyerhofer, and D. R. Harding, "Wetted-Foam Target Designs for the NIF and OMEGA."

F.-Y. Tsai, E. L. Alfonso, S. H. Chen, D. R. Harding, and T. N. Blanton, "Effects of Processing Conditions on the Quality and Properties of Vapor-Deposited Polymide Shells."

M. D. Wittman, D. R. Harding, P. W. McKenty, H. Huang, L. S. Iwan, T. J. Kessler, L. Elasky, and J. Sailer, "Layering and Characterization of Solid Deuterium Fuel Layers in Permeation-Filled Cryogenic Targets for OMEGA."

A. V. Tikhonravov, M. K. Trubetskov, I. V. Kockikov, J. B. Oliver, and D. J. Smith, "Real-Time Characterization and Optimization of *E*-Beam Evaporated Optical Coatings," Optical Interference Coatings, Topical Meeting and Tabletop Exhibit, Banff, Alberta, Canada, 15–20 July 2001.

S. D. Jacobs, S. R. Arrasmith, I. A. Kozhinova, S. R. Gorodkin, L. L. Gregg, H. J. Romanofsky, and T. D. Bishop II, "Effects of Changes in Fluid Composition on Magnetorheological Finishing of Glasses and Crystals," 10th International Conference on Precision Engineering (ICPE), Yokohama, Japan, 18–20 July 2001.

The following presentations were made at SPIE's 46th Annual Meeting, The International Symposium on Optical Science and Technology, San Diego, CA, 29 July–3 August 2001:

S. R. Arrasmith, S. D. Jacobs, J. Lambropoulos, A. Maltsev, W. Kordonski, D. Golini, and E. Cleaveland, "The Use of Magnetorheological Finishing (MRF) to Relieve Residual Stress and Subsurface Damage on Lapped Semiconductor Silicon Wafers."

J. E. DeGroote, S. D. Jacobs, L. L. Gregg, and A. E. Marino, "Quantitative Characterization of Optical Polishing Pitch."

I. A. Kozhinova, S. R. Arrasmith, J. C. Lambropoulos, S. D. Jacobs, and H. J. Romanofsky, "Anisotropy in MRF Removal Rate for a Sapphire Single Crystal."

The following presentations were made at the EuroConference on Advanced Diagnostics for Magnetic and Inertial Fusion, Varenna, Italy, 3–7 September 2001:

R. L. Keck, W. R. Donaldson, V. Yu. Glebov, P. A. Jaanimagi, F. J. Marshall, P. W. McKenty, D. D. Meyerhofer, S. P. Regan, W. Seka, C. Stoeckl, and R. Boni, "Laser and X-Ray Irradiation Diagnostics That Have Paved the Path Toward Significantly Improved ICF Target Performance."

W. Seka, R. S. Craxton, R. L. Keck, J. P. Knauer, D. D. Meyerhofer, S. P. Regan, C. Stoeckl, B. Yaakboi, R. E. Bahr, D. Montgomery, B. Baldis, and R. Kirkwood, "Laser–Plasma Interaction Diagnostics for ICF Fusion Research."

C. Stoeckl, J. A. Delettrez, R. Epstein, V. Yu. Glebov, R. L. Keck, R. L. McCrory, P. W. McKenty, F. J. Marshall, D. D. Meyerhofer, P. B. Radha, S. P. Regan, S. Roberts, W. Seka, S. Skupsky, V. A. Smalyuk, C. Sorce, J. M. Soures, R. P. J. Town, B. Yaakobi, J. A. Frenje, C. K. Li, R. D. Petrasso, F. H. Séguin, K. Fletcher, S. Padalino, C. Freeman, N. Izumi, R. Lerche, T. W. Phillips, and T. C. Sangster, "Measuring Core Performance and Mix in Direct-Drive Spherical Implosions on OMEGA."

The following presentations were made at the Second International Conference on Inertial Fusion Sciences and Applications, Kyoto, Japan, 9–14 September 2001:

C. K. Li, F. H. Séguin, J. A. Frenje, S. Kurebayashi, R. D. Petrasso, J. M. Soures, D. D. Meyerhofer, V. Yu. Glebov, P. B. Radha, S. Roberts, W. Seka, C. Stoeckl, and T. C. Sangster, "Charged-Particle Spectroscopy on OMEGA and Recent Results of Capsule Implosion Studies."

D. D. Meyerhofer, J. H. Kelly, R. P. J. Town, L. J. Waxer, S. J. Loucks, R. L. McCrory, W. Seka, and S. Skupsky, "An Integrated Fast Ignitor Experiment for OMEGA."

P. B. Radha, J. A. Delettrez, R. Epstein, V. Yu. Glebov, V. N. Goncharov, R. L. Keck, R. L. McCrory, P. W. McKenty, F. J. Marshall, D. D. Meyerhofer, S. P. Regan, S. Roberts, W. Seka, S. Skupsky, V. A. Smalyuk, C. Sorce, C. Stoeckl, J. M. Soures, R. P. J. Town, B. Yaakobi, J. D. Zuegel, J. A. Frenje, C. K. Li, C. K. Petrasso, F. H. Séguin, K. Fletcher, S. Padalino, C. Freeman, N. Izumi, R. Lerche, T. W. Phillips, and T. C. Sangster, "Compressed Core Conditions in Direct-Drive Spherical Implosions on OMEGA."

S. P. Regan, B. Yaakobi, J. A. Delettrez, V. A. Smalyuk, F. J. Marshall, R. Epstein, V. Yu. Glebov, P. A. Jaanimagi, D. D. Meyerhofer, P. B. Radha, W. Seka, S. Skupsky, J. M. Soures, C. Stoeckl, R. P. J. Town, D. A. Haynes, Jr., C. F. Hooper, C. K. Li, R. D. Petrasso, and F. H. Séguin, "High-Density, Direct-Drive Implosions on OMEGA."

S. Skupsky, R. Betti, T. J. B. Collins, V. N. Goncharov, D. R. Harding, R. L. McCrory, P. W. McKenty, D. D. Meyerhofer, and R. P. J. Town, "High-Gain, Direct-Drive Target Designs for the National Ignition Facility."

R. P. J. Town, V. N. Goncharov, P. W. McKenty, J. A. Delettrez, R. Epstein, R. L. McCrory, P. B. Radha, S. Skupsky, V. Yu. Glebov, D. R. Harding, D. D. Meyerhofer, F. J. Marshall, S. P. Regan, W. Seka, V. A. Smalyuk, C. Stoeckl, J. M. Soures, B. Yaakobi, and J. D. Zuegel, "OMEGA Direct-Drive Cryogenic Target Physics."

UNIVERSITY OF
ROCHESTER